

Spallation Neutron Source RCS Pre-Conceptual Design

(Draft, May 4, 1999)

Contents

1	Overview	6
1.1	Introduction	6
1.2	Design Philosophy	7
1.3	Layout and Parameters	8
2	Synchrotron	11
2.1	Introduction	11
2.2	Lattice	12
2.2.1	FODO/Doublet hybrid lattice	12
2.2.2	Sextupole compensation	13
2.3	Injection	16
2.3.1	Injection layout and parameters	16
2.3.2	Injection painting	18
2.3.3	Injection kickers	21
2.4	Ramping	23
2.4.1	Programmable ramping	23
2.4.2	Ramping simulation	24
2.5	Aperture and Beam Loss	25
2.5.1	Aperture clearance	25
2.5.2	Dynamic aperture	25
2.5.3	Loss budget	25
2.6	Collimation	26
2.6.1	Beam gap cleaning	26
2.6.2	Momentum collimation	26
2.6.3	Betatron collimation	26
2.6.4	Alternative collimation designs	27
2.6.5	Collimator design	28
2.7	Magnets	32
2.7.1	Magnet requirements	32
2.7.2	Expected magnetic field errors	45
2.7.3	Expected magnet misalignments	45
2.8	Power Supply	48
2.8.1	Selection criteria	48
2.8.2	Options, selection and discussions	48
2.8.3	Challenges	49
2.9	Radio-Frequency System	50
2.9.1	Requirements	50
2.9.2	General considerations	50
2.9.3	Cavity	50
2.9.4	Power amplifier	52
2.9.5	Beam loading and stability	53
2.9.6	Low level rf beam control	53

2.9.7	Second harmonic system	54
2.9.8	Summary	54
2.10	Vacuum System	55
2.10.1	Vacuum considerations	55
2.10.2	Vacuum chambers	56
2.11	Extraction	58
2.11.1	Kicker specifications	59
2.11.2	Lambertson magnetic septum	62
2.11.3	Timing and synchronization	62
2.12	Impedance	64
2.12.1	Resistive Wall Impedance	64
2.12.2	Space Charge Impedance	65
2.12.3	Broad Band Impedance	65
2.12.4	Low Frequency Impedance	68
2.12.5	Narrow band impedance	70
2.12.6	Impedance budget	71
2.13	Collective instabilities	72
2.13.1	Longitudinal microwave instability	72
2.13.2	Transverse instabilities	72
2.13.3	e-p like (PSR) instability	80
2.14	Beam Diagnostic Instrumentation	83
2.14.1	Beam Loss Monitors	83
2.14.2	Beam Current Monitors	84
2.14.3	Beam Profile Monitor	84
2.14.4	Beam Position Monitors	85
2.14.5	Damper/tune measurement	86
2.14.6	Beam-in-gap cleaner	86
3	High Energy Beam Transfer Line	87
3.1	Introduction	87
3.1.1	LINAC to Achromat matching section	91
3.1.2	LINAC beam dump	91
3.1.3	Momentum selection (Achromat)	91
3.1.4	Energy stabilizer & energy wobbler	91
3.1.5	Ring matching section	92
3.2	Magnets and Support	93
3.3	Collimation and Halo Scraping	94
3.4	Instrumentation and Diagnostics	95
3.5	Vacuum System	96
4	Ring to Target Beam Transfer Line	97
4.1	Introduction	97
4.2	Design Description and Functions of the RTBT Line	100
4.2.1	Extraction section	100

4.2.2	Extraction dump	100
4.2.3	Beam spreader	100
4.3	Magnet System	101
4.4	Halo scraping (collimation)	101
4.5	Beam Diagnostic Instrumentation	101
4.6	Vacuum System	102
5	Challenges	103
6	Appendix	104

Acknowledgments

Authors:

Lattice:	C. Gardner, Y.Y. Lee, J. Wei
Injection:	C. Gardner, Y.Y. Lee, J. Beebe-Wang, W. Meng, S. Y. Zhang
Ramping:	S.Y. Zhang, J.D. Galambos, A.U. Luccio, J. Beebe-Wang
Aperture and loss:	J. Wei, N. Malitsky, D. Raparia
Magnet system:	G. Danby, J. Jackson
Power supply:	A. Soukas,
RF system	M. Blaskiewicz, M. Brennan, A. Zaltsman
Collimation:	N. Catalan-Nasheras, H. Ludewig, P. Cameron, J. Wei
Vacuum:	H.C. Hseuh, M. Blaskiewicz
Extraction:	N. Tsoupas
Impedance:	S.Y. Zhang, J.G. Wang, M. Blaskiewicz
Instabilities:	S.Y. Zhang, J.G. Wang
Instrumentation:	R. Witkover, P. Cameron
HEBT and RTBT:	D. Raparia, R. Witkover, H.C. Hseuh
Engineering aspects:	A. Soukas, J. Tuozzolo

Other Contributors:

D. Abell, J. Alessi, S. Danilov, S. Machida, K. Reece, G. Rees, T. Roser, W.T. Weng, and the SNS team at the Brookhaven National Laboratory.

Acknowledgments:

V. Biryukov, Y. Cho, B. Blind, P. Grande, A. Jason, R. Kustom, D. Lowenstein, R. Macek, D. Moncton, J. Negrin, R. Talman, P. Thieberger

Editor:

J. Wei

1 Overview

1.1 Introduction

The Spallation Neutron Source (SNS) is designed to meet the growing need for new tools that will deepen our understanding in materials science, life science, chemistry, fundamental and nuclear physics, earth and environmental sciences, and engineering sciences. The SNS is based on an accelerator producing an average beam power of 2 MW at a repetition rate of 60 Hz.

This report documents the study of an alternative approach to the accelerator design. The nominal accelerator complex (LAR) [1] consists of the source and the front end, a 1 GeV full-energy LINAC, a single accumulator ring and its transfer lines, and the target. The alternative accelerator complex consists of similar source, front end, and target, but a shortened LINAC and a pair of rapid-cycling synchrotrons (RCS).

On April 9, 1999, the SNS management defined the boundary condition for this alternative complex to consist of a 400 MeV LINAC injecting into two synchrotrons, each accelerating beam pulses of 1.04×10^{14} protons at a repetition rate of 30 Hz from 400 MeV to 2 GeV, producing a combined beam power of 2 MW. The two synchrotrons are vertically stacked sharing the same tunnel. Figure 1.1 shows the alternating ramping cycle of two synchrotrons.

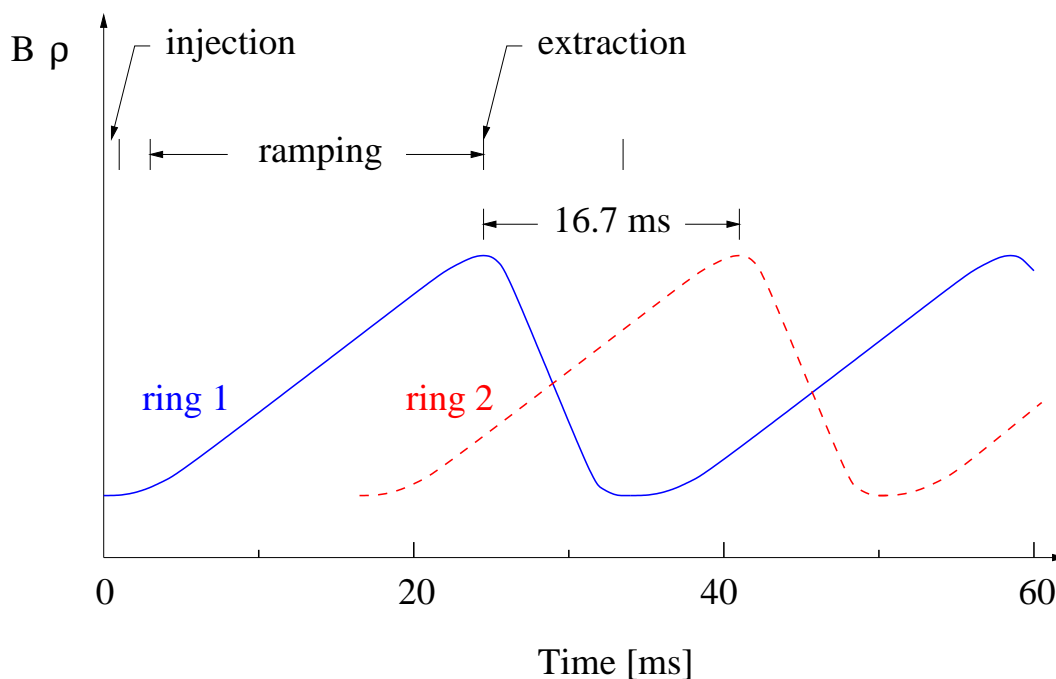


Figure 1: Ramping cycle of two rapid-cycling synchrotrons providing a total of 2 MW beam power.

1.2 Design Philosophy

Reliability and maintainability are of primary importance to the SNS facility. Based on operational experience at both LINAC [2] and the AGS Booster, [3] hands-on maintenance demands that the uncontrolled beam loss be limited to about 1 W of beam power per tunnel meter. For two synchrotrons, each with circumference near 300 meters, this corresponds to an average uncontrolled beam loss of 4×10^{-4} at 400 MeV beam energy.

Among the existing RCS machines, typical beam loss ranges from several to tens of percent. Major beam loss usually occurs at injection and the initial ramping stage (first 5 ms). These beam losses are typically attributed to a high space charge tune shift (0.5 or larger), limited physical and momentum acceptance, and large magnetic field errors.

The SNS synchrotrons are designed with practically achievable large acceptance so that beam space charge tune shift remains about 0.2. The use of programmable ramping moderates the required RF voltage and ramp rate, resulting in a reasonable machine circumference and a tolerable eddy-current induced magnet errors. Lengths of the magnets are chosen to avoid excessive error due to saturation fringe field.

Effective collection of the beam halo is essential for maintaining a low uncontrolled beam loss. To facilitate the momentum cleaning and multi-stage collimation systems, a wide momentum acceptance (full beam plus $\pm 2\%$ in $\Delta p/p$) is chosen. This allows cleaning of the momentum halo using a multi-turn beam gap kicker system. With the collimation system designed to be more than 90% efficient, the total allowed beam loss is at 1% level.

Flexibility is another important aspect considered in the design. A matched FODO/doublet hybrid lattice is chosen so that chromatic and resonance correction can be done mainly in the FODO arcs, while long uninterrupted doublet straight sections allow flexible modular operation (injection painting independent of lattice tuning, long uninterrupted straight section, balanced RF cavity arrangement, possible collimation “dog leg”, etc.). Since the FODO arc and doublet straight section are optically matched, a low amplitude (β_{max}) is achieved for the given cell length, thus confining the beam size.

To address the issue of engineering reliability, the collimator and shielding hardware are designed to withstand an average of 10^{-2} beam power. In addition, the machine is designed to withstand a couple of full beam pulses during commissioning and in case of emergency.

1.3 Layout and Parameters

The synchrotron version of the Spallation Neutron Source consists of the front end, a 400 MeV LINAC, two vertically stacked synchrotrons and their transfer lines, the target, and the instrumentation lines. The beam power at the target is 2 MW at a repetition rate of 60 Hz.

Table 1.3 lists the LINAC parameters. The LINAC repetition rate is 60 Hz. In the

Table 1: LINAC requirements and LINAC/HEBT interface parameters.

Quantity	Value	unit
Energy, E_k	400	MeV
Average current	1.1	mA
Repetition rate	60	Hz
Peak current	~ 50	mA
Chopping rate	60	%
Pulse length	0.60	msec
Duty cycle	3.6	%
Energy fluctuation	0.5	MeV
Energy spread, ΔE_k (rms)	0.2	MeV
Emittance (unnormalized, rms)	0.5	π mm mr
Off-normal emittance limit	1	π mm mr
Transverse halo (5σ)	5×10^{-4}	
Beam gap residual	5×10^{-4}	

High Energy Beam Transfer (HEBT) line, a switching dipole magnet operating at 30 Hz alternates the proton beam between the two synchrotrons. Each synchrotron accelerates pulses of 1.04×10^{14} protons from 400 MeV to 2 GeV at a repetition rate of 30 Hz. The beams are then extracted from the synchrotrons and combined in the Ring-to-Target Beam Transfer (RTBT) line by another switching dipole magnet, producing a total beam power of 2 MW at the target .

Figure 1.3 shows one of the two vertically stacked synchrotrons and their transfer lines. Table 1.3 shows the major design parameters of the synchrotrons. Table 1.3 shows the evolution of beam parameters.

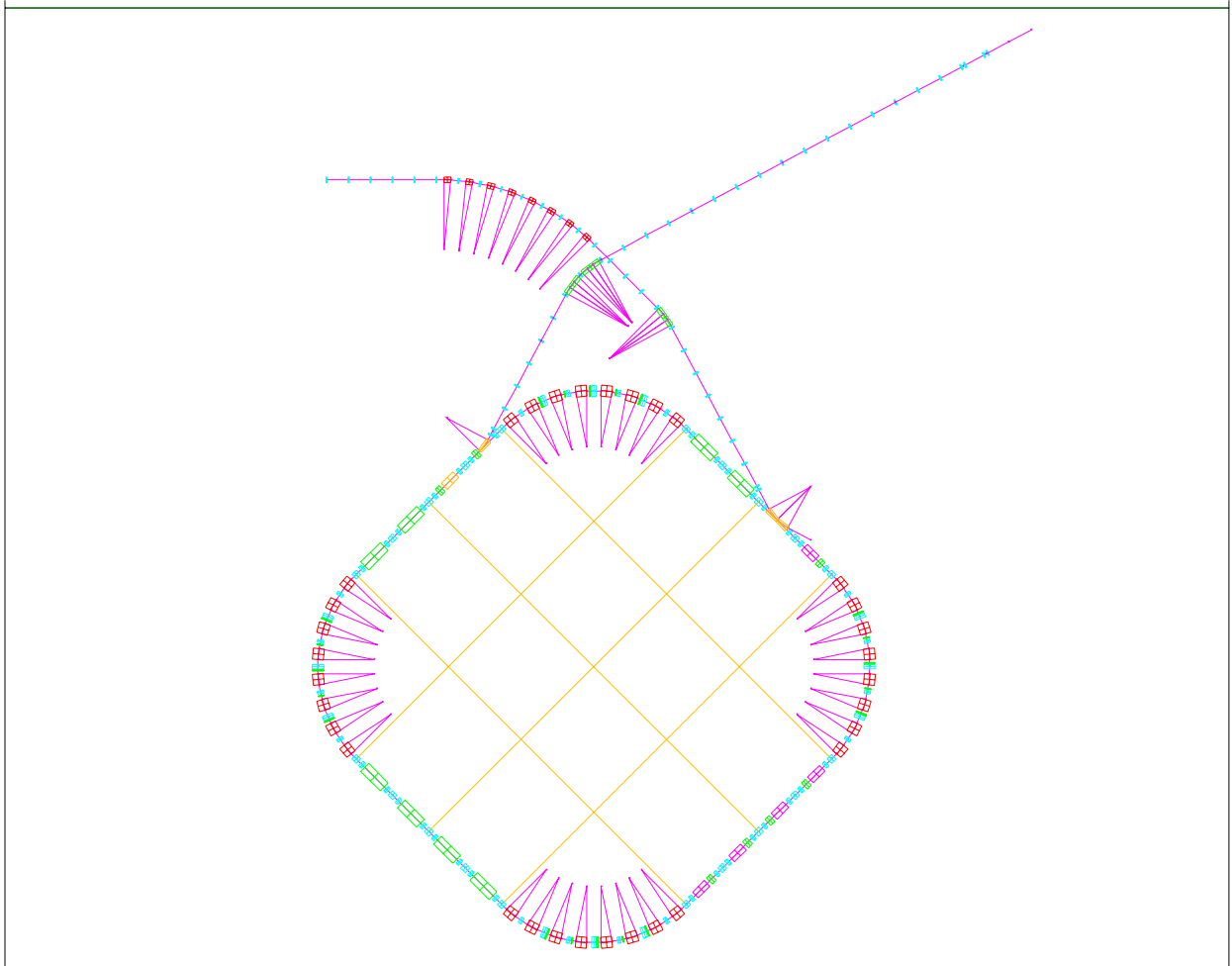


Figure 2: Layout of rapid-cycling synchrotrons and their transfer lines.

Table 2: Spallation Neutron Source synchrotron major machine parameters.

Quantity	Value	unit
Number of synchrotron rings	2	
Vertical center-to-center separation	2	m
Circumference	299.2	m
Average radius	47.619	m
Injection energy	400	MeV
Extraction energy	2	GeV
Beam power per ring	1	MW
Repetition rate per ring	30	Hz
Extraction energy range	– 2	GeV
Repetition rate range	30 –	Hz
Number of proton	1.04	10^{14}
Peak dipole field	0.91	T
Peak ramp rate	29.4	T/s
Up-ramp period	24	msec
RF harmonic	2, 4	
Peak rf voltage, $h = 2$	300	kV
Peak rf voltage, $h = 4$	100	kV
Normalized emittance	264	π mm mr
Betatron acceptance	520 + clearance	π mm mr
Additional beam clearance	5	mm
Momentum acceptance (full beam)	± 2	%
Momentum acceptance (zero amplitude)	± 3.8	%
Magnetic rigidity, $B\rho$	3.18 – 9.29	Tm
Bending radius, ρ	10.186	m
Horizontal tune	7.82	
Vertical tune	7.30	
Transition energy, γ_T	5.91	
Horizontal natural chromaticity	–9.93	
Vertical natural chromaticity	–7.48	
Number of superperiod	4	
Arc lattice	4 FODO cells	
Straight section lattice	4 doublet cells	
Lattice cell length	9.35	m

2 Synchrotron

2.1 Introduction

Figure 2.1 shows a schematic layout of one of the two rapid-cycling synchrotrons. The ring is four-fold symmetric consisting of FODO arcs and doublet straight sections. The FODO structure in the arcs allows easy chromatic and resonance correction, while long uninterrupted doublet straight sections allows flexible modular operation (injection painting independent of lattice tuning, long uninterrupted straight section, balanced RF cavity arrangement, possible collimation “dog leg”, etc.) Since the FODO arc and doublet straight section are optically matched, low (β_{max}) amplitude is achieved for the given cell length to confine the beam size.

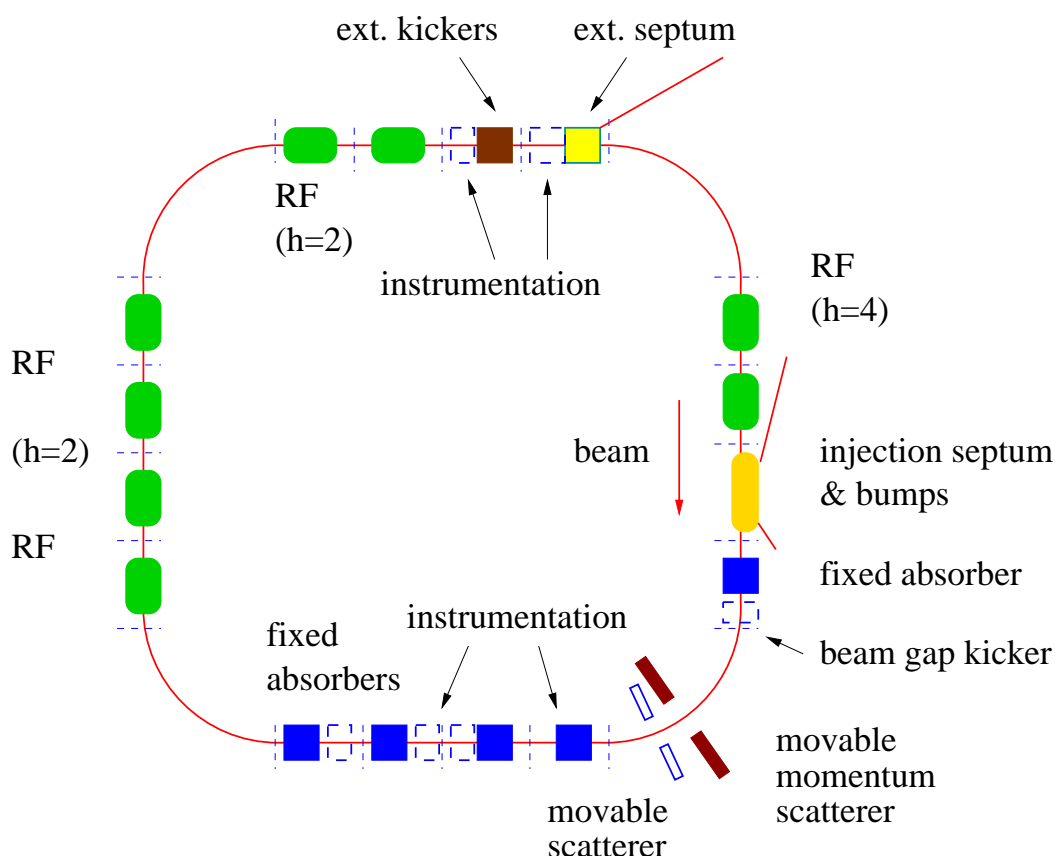


Figure 3: Schematic layout of the rapid cycling synchrotron.

Beam injection is entirely confined in one of the straight sections. Immediately downstream of the injection section, beam halo absorbers are placed to protect against injection malfunction and beam halo. The beam cleaning and collimation section starts with a beam gap kicker located 90 degrees in betatron phase advance upstream of the primary collimator. Following the first beam are movable beam halo scatters and collimators covering a 2π betatron phase. Radio frequency (RF) systems of both ($h = 2$) and ($h = 4$) occupy 50% of the available straight sections. The beam is extracted by fast vertical kickers, located immediately before a set of triplet quadrupole magnets, and a horizontal Lambertson septum magnet.

2.2 Lattice

2.2.1 FODO/Doublet hybrid lattice

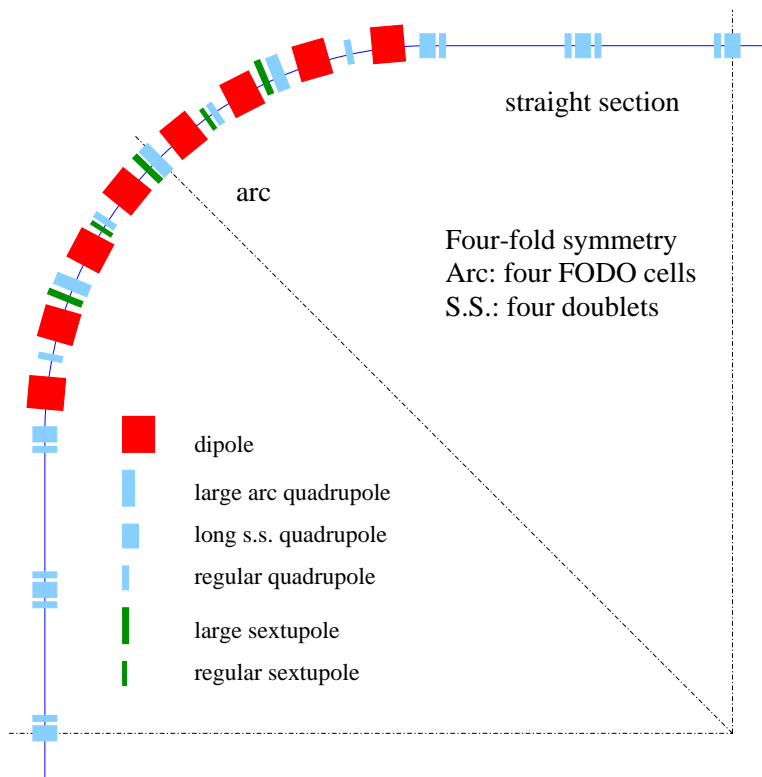


Figure 4: Ring magnet layout.

For the RCS Ring we have chosen a FODO-Doublet Hybrid lattice similar to that proposed for the Accumulator Ring [8]. The lattice consists of four superperiods, each containing a 90° arc and a long straight section. In order to make the dispersion zero in the long straights, the arcs are made of four identical FODO cells, each cell having a betatron phase advance of $\pi/2$ in the horizontal plane. Using AC to denote the Arc Cell, we write, in the notation of the MAD program,

$$\text{AC: Line} = (\text{QF}, \text{O}, \text{BND}, \text{O}, \text{QD}, \text{QD}, \text{O}, \text{BND}, \text{O}, \text{QF}).$$

Here QF and QD are horizontal Focusing and Defocusing half-quadrupoles of length $0.75/2$ m and $0.60/2$ m respectively, O is a drift of length 1.0 m, and BND is a 11.25° bend of length 2.0 m. Each Arc Cell is therefore 9.35 meters long and bends the beam 22.5° . The 1.0 m drift spaces on either side of the bends can accommodate the necessary vacuum pumps, bellows, position monitors, sextupoles and correction elements. They also allow for momentum collimation in the dispersive regions of the arc. The total 90° arc, consisting of 4 cells, is given by

$$\text{ARC: Line} = (\text{AC}, \text{AC}, \text{AC}, \text{AC}).$$

Four identical Doublet Cells form each long straight section. We use DC to denote these cells and write

$$\text{DC: Line} = (\text{QFS}, \text{L}, \text{QDS}, \text{QDS}, \text{LL}, \text{QDS}, \text{QDS}, \text{L}, \text{QFS}).$$

Here QFS and QDS are horizontal Focusing and Defocusing half-quadrupoles of length 1.15/2 m and 0.60/2 m respectively, L is a short drift of length 0.3 m separating the quadrupoles in each doublet, and LL is a long drift of length 6.5 m. Each Doublet Cell is therefore 9.45 m long and provides 6.5 m of free drift space. Each superperiod, starting from the center of one long straight section and going to the center of the next, is then 75.2 m long and is given by

$$\text{SP: Line} = (\text{DC}, \text{DC}, \text{ARC}, \text{DC}, \text{DC}).$$

The four long straights of the Ring provide a total of $4 \times 4 \times 6.5 = 104$ m of free drift space to house injection, collimation, rf cavities, and extraction systems. (The circumference of the ring is $4 \times 75.2 = 300.8$ m.)

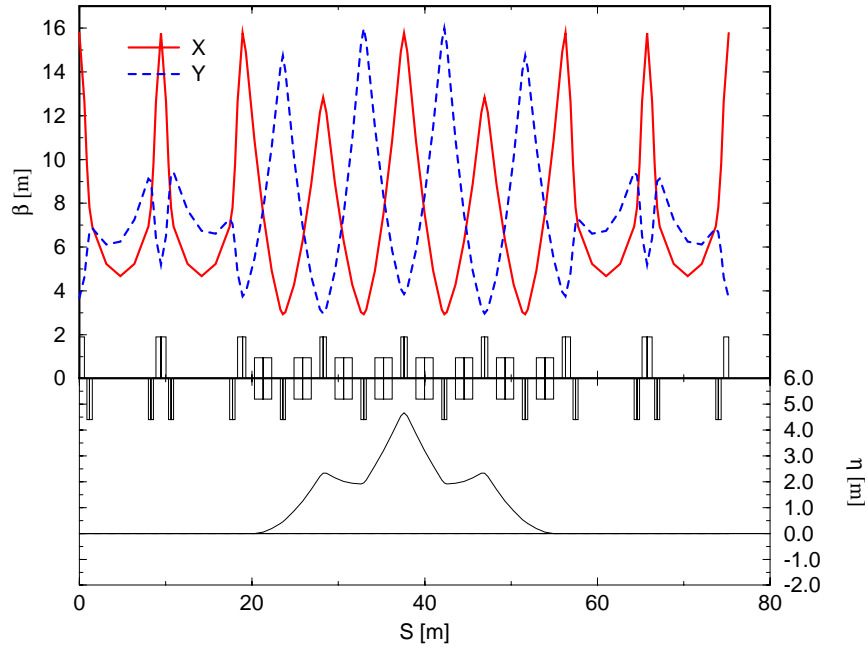
The horizontal and vertical tunes of the lattice are taken to be $Q_H = 7.82$ and $Q_V = 7.30$. These give betatron phase advances of approximately $\pi/2$ for the Doublet Cells and provide sufficient tune separation to minimize transverse coupling. The possibly harmful structure resonances at tunes of $6 + 2/3$ and 8 are also avoided. The lattice functions are shown in Fig. 2.2.1 where the plot runs from the center of one straight section to the center of the next.

The maximum beta in both planes is 16 m and the ratio of maximum to minimum beta is 5.4. The dispersion reaches a maximum of 4.7 m at the center of each arc. The quadrupole gradients required at the injection energy of 400 MeV and the extraction energy of 2 GeV are given in Table 4. (Here KF, KD, KFS, KDS are respectively the gradients in the Arc quadrupoles QF and QD, and the Straight Section quadrupoles QFS and QDS.)

2.2.2 Sextupole compensation

Table 3: Evolution of beam parameters from LINAC to the synchrotrons (per ring).

Quantity	LINAC	HEBT	RCS injection	RCS extraction
Energy, E_k [GeV]	0.4	0.4	0.4	2.0
Profile	Gaussian	Gaussian	quasi-uniform	quasi-uniform
Emittance, ϵ_{UN} (rms) [π mm·mr]	0.5	0.5	0.5 – 78	27
Emittance, ϵ_{UN} (99%) [π mm·mr]	0.5	0.5	0.5 – 260	89
Energy spread, $\Delta E/E$ (rms) [10^{-3}]	0.5	0.5 – 3	4.3	3.9
Energy spread, $\Delta E/E$ (99%) [10^{-3}]	1.5	1.5 – 6.8	12	11
Average current [mA]	1.1	1.1	1	1
Peak current [A]	0.05	0.03 – 0.03	0.03 – 12	16
D.C. current [A]	19	19 – 0.6	0.6 – 26	75
Transverse S.C., $\Delta\nu$			– 0.24	– 0.24
Transverse S.C., $ \Delta\nu/\nu $ [%]			3.1	3.1



Time: Mon May 3 12:20:02 1999 Last file modify time: Sat May 1 11:44:21 1999

Figure 5: FODO-Doublet Hybrid Lattice.

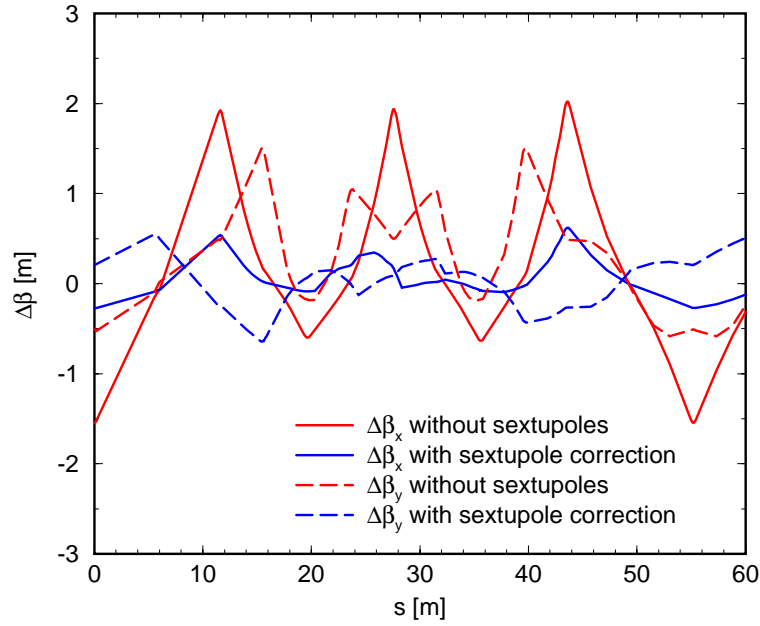


Figure 6: Reduction in the off-momentum amplitude mismatch using arc sextupoles. The study is done with MAD.

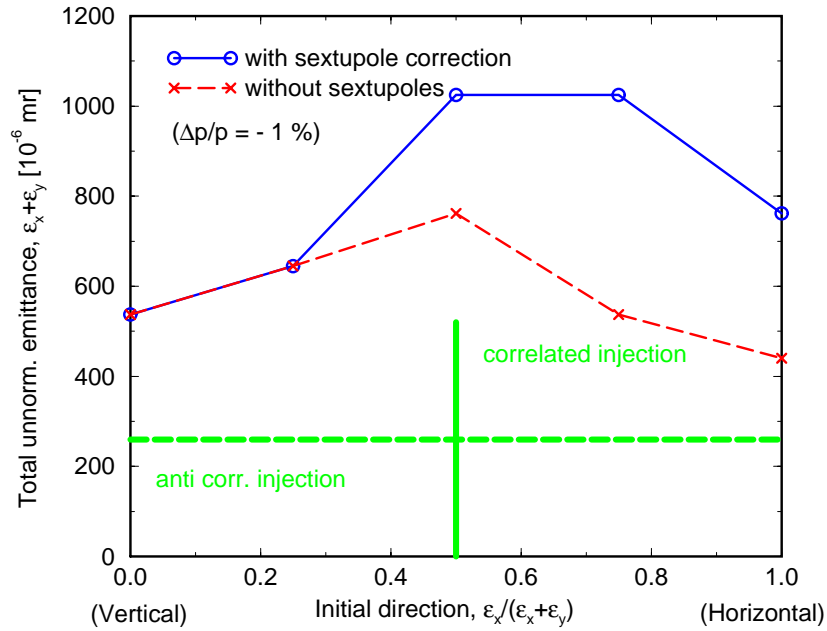


Figure 7: Improvement in the DA due to off-momentum optics optimization using arc sextupoles. The 6 dimensional tracking is done with TEAPOT.

Table 5: RCS injection parameters.

Quantity	Value	unit
Injection energy, E_k	400	MeV
β	0.7131	
γ	1.4264	
$\beta\gamma$	1.017	
Momentum, p_0	0.954	GeV/c
Revolution frequency	0.714	MHz
Revolution period	1.40	μs
Emittance	260	π mm mr
Injection turns	429	
Injection period	600	μs
RF voltage, $h = 2$	120	kV
RF synchronous phase, ϕ_s	0.0	
RF frequency, $h = 2$	1.43	MHz
RF frequency, $h = 4$	2.86	MHz
RF bucket area	6.68	eVs
Bunch area	3.8	eVs
Synchrotron frequency	2.8	kHz
Synchrotron period	252	turn
Number of bunches	2	
Bunching factor	0.46	
Bunch center distance	700	ns
Bunch length	420	ns
Beam gap width	280	ns
Magnetic rigidity, $B\rho$	3.18	Tm
Dipole field	0.31	T
Quadrupole gradient	1.6, 1.3, 2.0	T/m
Sextupole gradient, B''	28, 22	T/m ²

2.3.2 Injection painting

Since the beam is injected into the ring at a dispersion-free region, beam phase-space painting in the transverse direction is conveniently de-coupled from the longitudinal beam manipulation. Furthermore, painting in the horizontal and vertical direction can be adjusted independently. The injection system is designed to accommodate both x-y correlated and x-y anti-correlated painting schemes, illustrated in Figure 2.3.2.

With a x-y correlated bump setting, phase spaces in both dimensions are painted from small to large emittance. Figure 2.3.2 and Figure 2.3.2 give the simulation results of correlated painting at the end of injection (0.6ms) and at the end of ramping (21ms) respectively. Ideally, the resulting rectangular transverse profile obtained from correlated painting have better chance to meet the target requirements. However, such a beam profile is susceptible to transverse coupling due to magnet misalignment and space charge forces, which in turn results in an effective doubling of the maximum emittance in both directions. On the other hand, with the x-y anti-correlated scheme the total transverse emittance is approximately constant during the injection. The resulting beam profile achieved by x-y anti-correlated painting, is immune to the transverse coupling. Figure 2.3.2 and Figure 2.3.2 give the simulation results of correlated painting at the end of injection (0.6ms) and at the end of ramping (21ms) respectively. Computer simulations with ramping and space charge was performed with ACCSIM tracking code. The results with the two painting schemes are summarized in Table 2.3.2.

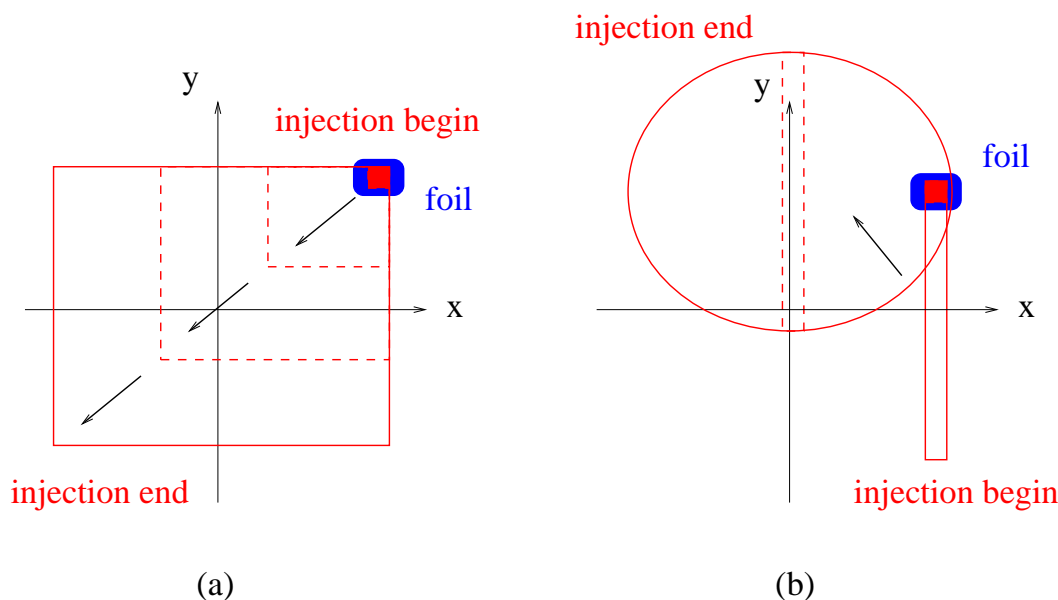


Figure 9: Basic painting scenarios. (a) x-y correlated painting, (b) x-y anti-correlated painting.

Table 6: Tracking results with correlated and anti-correlated painting.

Quantity	Correlated	Anti-correlated	Unit
$\varepsilon_{UN,x}$ (RMS) at the beginning of injection	0.5	0.5	π mm-mr
$\varepsilon_{UN,x}$ (99%) at the beginning of injection	0.5	0.5	π mm-mr
$\varepsilon_{UN,x}$ (RMS) at the end of injection	57	54	π mm-mr
$\varepsilon_{UN,x}$ (99%) at the beginning of injection	249	264	π mm-mr
$\varepsilon_{UN,y}$ (RMS) at the beginning of injection	0.5	0.5	π mm-mr
$\varepsilon_{UN,y}$ (99%) at the beginning of injection	0.5	0.5	π mm-mr
$\varepsilon_{UN,y}$ (RMS) at the end of injection	56	50	π mm-mr
$\varepsilon_{UN,y}$ (99%) at the beginning of injection	245	251	π mm-mr
ε_l (RMS) at the end of injection	0.95	0.93	eV-s
ε_l (99%) at the beginning of injection	5.29	5.31	eV-s
Max ν_x at the end of injection	0.244	0.222	
Max ν_x at the end of ramping	0.056	0.055	
Max ν_y at the end of injection	0.248	0.242	
Max ν_y at the end of ramping	0.069	0.062	
Foil size (H \times V)	5×5	5×5	mm ²
Average Foil hits during injection	3.12	3.90	

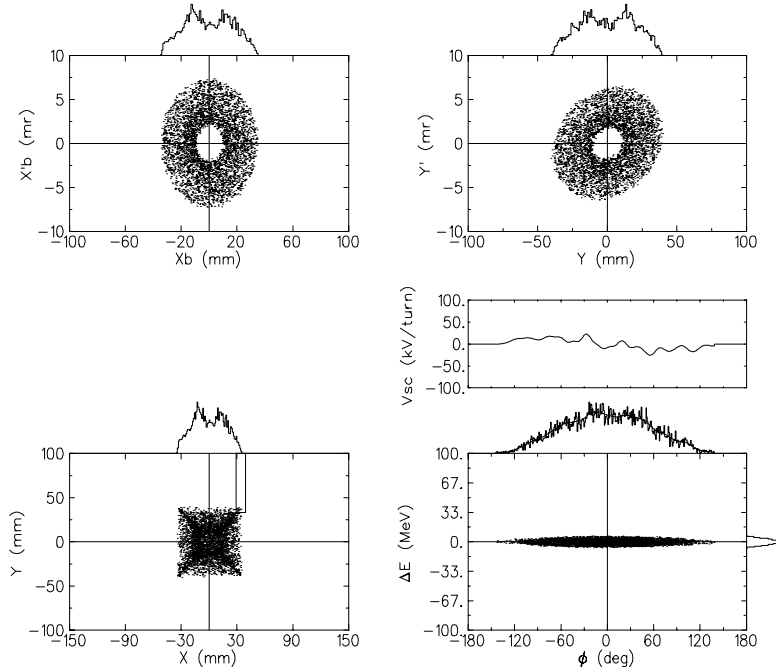


Figure 10: Correlated painting at the end of 0.6 msec injection.

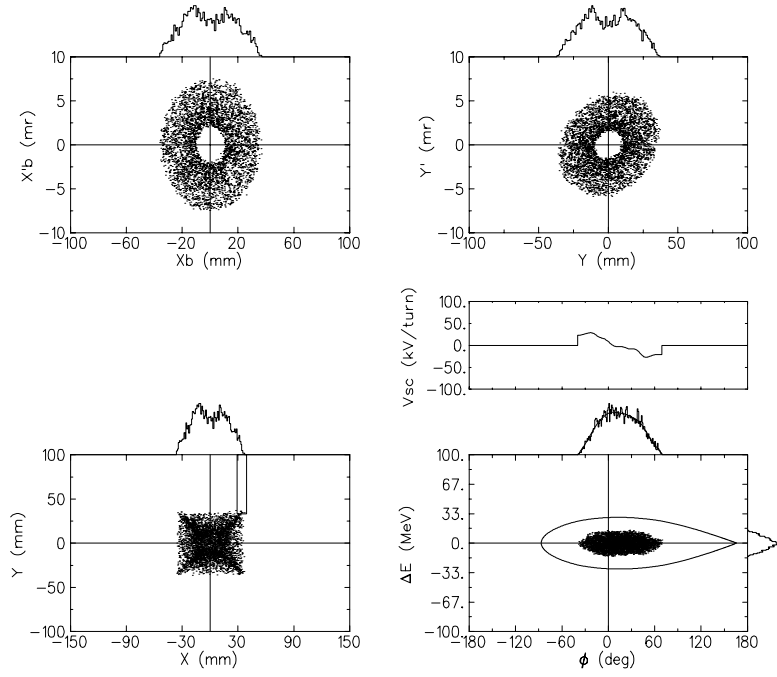


Figure 11: Correlated painting at the end of ramping (21 ms).

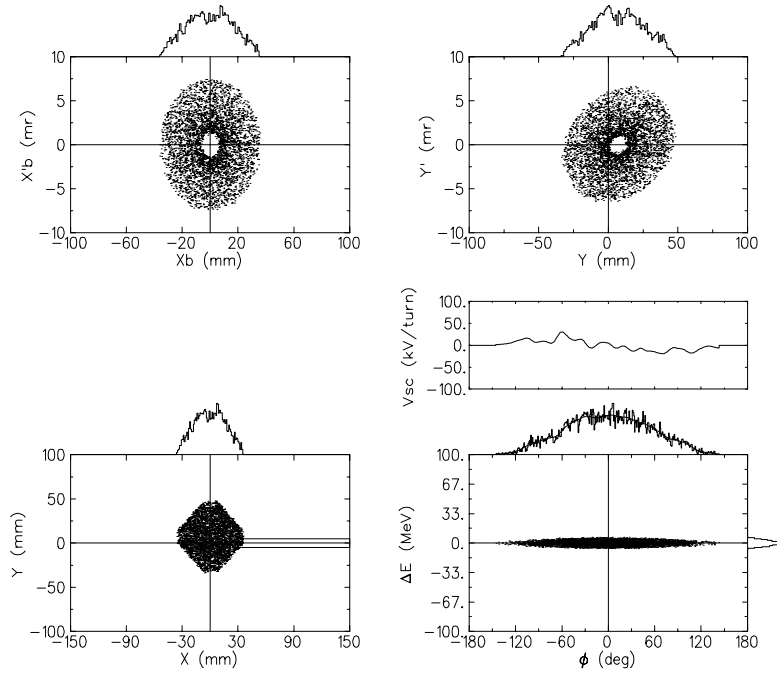


Figure 12: Anti-correlated painting at the end of 0.6 msec injection.

2.3.3 Injection kickers

Two options of injection dynamic-bump kickers are investigated.

The first option is to make 20 cm long kickers for individual H/V kick, with the field strength on the order of 4 kG ramped in 300 μ s. Opera 2d static state calculation shows that this option can be achieved by using laminated steel and high conductivity Cu plate to construct a window-frame magnet. The clear aperture is 24.6 cm (square). The uniformity of the field is 2.5×10^{-4} on the 5 cm radius. The maximum field in the steel is about 12 kG. Total stored energy is 775 Joule (assuming the length is 20 cm). The self-inductance is estimated as 1.0 μ H.

The second option is to combine H/V kicking functions in one magnet, with the field strength of 2 kG which can be controlled by individual power supply. The eddy current effect was studied by using Opera 2d transient program. Figure 2.3.3 shows the case that the eddy current generated in the horizontal Cu plate (due to ramping current in the vertical Cu plate), which tends to reduce the central field. The color zones show the eddy current density in the unit of ampere per square centimeter. By breaking down the Cu plate into 8 smaller Cu conductors, Figure 2.3.3 shows the significant reduction of the total eddy current influence on the central field at the same time ($t = 0.0002$ sec). In the latter case (Figure 2.3.3), with firing as a horizontal kicker only, the stored energy is about 400 joule (assuming the length is 40cm); the corresponding self-inductance is 124 μ H. Figure 2.3.3 shows the comparison of the field rises with the same exponential ramp function: the solid curve stands for the ideal central field ramp along the time; the cross symbol stands for the poor field ramp suffered by eddy current effect in the Cu plate; the diamond symbol stands for the improved field ramp by using 8 smaller conductors. This case must be further studied for firing both kickers with slightly different ramp functions, in order to further investigate possible saturation and other problems

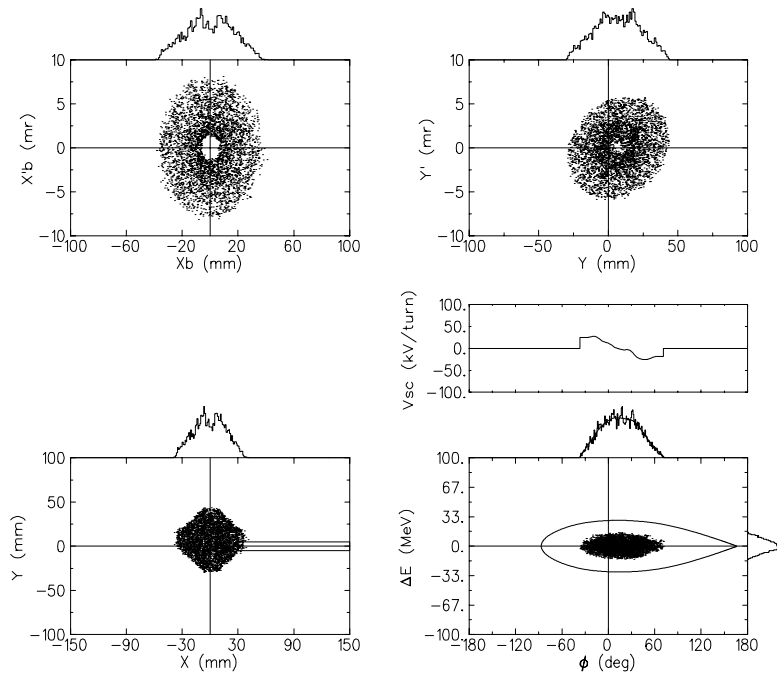


Figure 13: Anti-correlated painting at the end of ramping (21 ms).

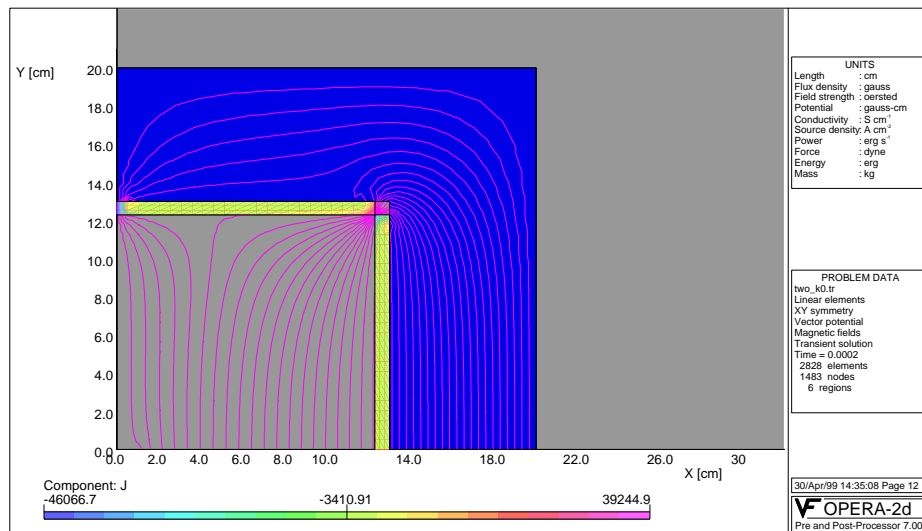


Figure 14: Eddy current effect generated in combined H/V kickers.

2.4 Ramping

2.4.1 Programmable ramping

Table 7: RCS ramp parameters.

Quantity	Value	unit
Ramp profile	programmable	
Injection flat period	1	msec
Up-ramp period	24	msec
Down-ramp period	8	msec
Maximum dipole ramp rate, \dot{B}	29.4	T/s

2.4.2 Ramping simulation

Simulation of the longitudinal phase space for the SNS Rapid Cycle Synchrotron was performed using the C++ code ORBIT. ORBIT is a full six-dimensional code including space charge, however for longitudinal mode only it has a special mode of operation that needs as input only the length of the machine and other basic parameters such as the value of gamma transition, bending radius, harmonic number and energy and number of real particles in the beam.

The macro-particles are created at random on a given distribution. In the longitudinal mode, the shape and the width of the distribution, both in energy and phase are prescribed. In the simulation, we used a truncated Gaussian distribution in energy within plus-minus 2.5 MeV, and a flat distribution in phase.

The bending field and the RF voltages are given as functions of time through an input stream (file) read by the code. Space charge effects are calculated, applied to the beam, and also affect the shape of the bucket separatrix shown in the output. At prescribed turn numbers, ORBIT generates PostScript graphic files showing the phase space distribution and the bucket and beam profiles in energy and phase.

In our simulation, for the acceleration of 1.04×10^{14} particles from 0.4 to 2 GeV (1 MW beam power in one ring) we considered three cases: (a) linear B field ramp with a flat front porch, and RF operating at the fundamental frequency, (b) linear ramp and dual frequency (first and seconds, pseudo-barrier bucket), and (c) sinusoidal ramp with fundamental RF.

Harmonic number was 2 and the number of macro particles used in the simulation 40,000, that allowed a reasonable accuracy in a short computer time (a few minutes). In the simulation, we tried to optimize the ramp and RF voltage shape in order to minimize losses (in all three cases we found no losses in the longitudinal space), while maintaining the synchronous phase to a small value and achieving a good bunch/bucket area ratio. We also tried to inject as long a bunch as we could to minimize the load on the injection LINAC. We found a comfortable value at plus-minus 125 degrees.

The bunch area was simply calculated as the area of an ellipse with semi-axes equal to the maximum displacement of the macros in energy and phase respectively (then, this area included 100% of the beam). The number of bins for space charge calculation and for beam distribution display was 16. Phase space diagrams are shown at 0.7 m sec (500 turns), 4.2 (3100), 7.3 (5600), 10.2 m sec (8100), 15.8 (13,100), and 22 (19,000).

The simulation showed that a very important role is played by the shape of the ramp in the region just after the injection at the beginning of acceleration in the case of a linear ramp with a flat front porch. It proved in fact very important that, in order to capture and retain the totality of the beam, the bucket separatrix would move adiabatically. We ended up in making this region (a cosine-like function) up to 5 msec long.

2.5 Aperture and Beam Loss

Four levels of beam loss control are implemented in the design of the synchrotrons: to guarantee hands-on maintenance, the total uncontrolled beam loss in the ring needs to be limited well below 10^{-3} ; the collimators are designed to collect beam halo at a level of 10^{-2} ; hardware and shielding are designed to withstand 10^{-2} for engineering reliability; and the machine can withstand a couple of full beam pulses for emergency handling and commissioning.

2.5.1 Aperture clearance

Table 8: Momentum aperture and sextupole improvement.

Item	Value
beam momentum spread (99%)	± 0.010
rf acceptance at 40 kV	± 0.012
ring acceptance at nominal emittance	± 0.020
ring acceptance at zero emittance	± 0.036

2.5.2 Dynamic aperture

2.5.3 Loss budget

Table 9: Loss budget for each synchrotron ring assuming $400\mu\text{g}/\text{cm}^2$ foil density.

Mechanism	Controlled loss	Uncontrol. loss
LINAC incoming halo		5×10^{-4}
LINAC gap residual		5×10^{-4}
<u>Injection loss:</u>		
missing foil	0.12	—
foil elastic scattering	—	5.2×10^{-5}
foil inelastic scattering	—	3.7×10^{-5}
H^0 production	0.02~0.11	$2 \sim 11 \times 10^{-8}$
ionization energy loss	—	5×10^{-6}
beam hitting septum	$< 10^{-3}$	
Capture loss	2×10^{-3}	2×10^{-4}
<u>Fault condition:</u>		
1 kicker missing	< 0.1	—
<u>LINAC off-normal:</u>		
doubled emittance	0.03~0.11	2.1×10^{-4}

2.6 Collimation

2.6.1 Beam gap cleaning

Ramp miscapture, chopper inefficiency, foil ionization, etc. can produce residual beam between subsequent micro bunches resulting in uncontrolled loss at early stage of ramping. A gap cleaning kicker is designed to be located at a straight section with a vertical betatron phase 90° (modulus integer) from that of the primary collimator, where beam loss is measured with a fast gated loss monitor. The hardware is similar to that of the RHIC Damper/Tune Monitor System, which uses commercially available MOSFET banks to supply 5 kV, 120 A, 10 ns rise and fall time pulses to a transmission line kicker. Burst mode frequency is greater than 1 MHz, permitting turn-by-turn kicking. With 5 meters of kicker length, the gap can be cleaned in about 10 turns near 400 MeV.

2.6.2 Momentum collimation

The need for momentum collimation is introduced by the ramping nature of the synchrotron. As acceleration takes place, protons uncaptured by the RF system, drift outwards due to dispersion and eventually hit the vacuum pipe at positions of high dispersion like the center of the arcs.

Large momentum aperture has been reserved so that momentum collimation can be achieved by employing the beam gap cleaning kickers as discussed in the next section.

2.6.3 Betatron collimation

The actual layout of the collimation system is shown in Figure 24. Two primary movable collimators are located in the first cell of the straight section. They will be equipped with horizontal and vertical jaws respectively and act as primary collimators. In the next three cells, fix aperture secondary collimators are installed. They are circular collimators cutting the secondary halo in the horizontal and vertical planes simultaneously. The design and operation of movable and fixed collimators is described in the collimator design section.

First, we will refer to mechanical collimation. This method consists of introducing a material jaw in the machine between the beam and the vacuum chamber intercepting the halo at a certain amplitude n_1 . As the drift velocity of the halo is generally small, the covers all phases of its betatronic oscillation before its amplitude increase sensibly. As a result, when a particle touches the jaw its coordinates are $x \approx x_{max}$ and $x \approx x_0$. Low impact parameters and angles lead to a high probability of grazing. The first effect of grazing is the production of secondary electrons in the surface of the collimators described in the collimator design section. The second effect is the generation of a secondary halo after the collimator that even if less dense, has bigger amplitude than the initial one.

Secondary collimators have thus to be installed downstream to intercept out-scattered protons in what is called a two stage collimation system. The principle for multistage collimation is sketched in Figure 24.

It is clear that the residual halo extends to larger amplitudes than the primary collimator aperture. In the one dimensional case this extent is n_2 , while in the two dimensional case the

optimum phase advance is not defined. Ideally, the number of secondary jaws to reduce has to be infinite. The final extent is determined by the number of secondary collimators and their aperture and phase advance with respect to the primary collimator.

There are two points that have to be studied before defining the final layout of the collimation system and compute the foreseen efficiency.

- The final efficiency of the system is determined by the extension of the halo escaping the secondary collimators. If the total extension of the Jaws, covers less than 360 degrees of phase advance, particles originated in primary collimators can leave the collimator section without interacting with any of the secondary absorbers. This will originate a residual halo which maximum extent is bigger than the secondary aperture n_2 .

The present layout offers us 360 degrees of phase advance and the possibility of cover all section with absorbers. Still, the exact phase advance between fixed collimators and the primary ones can be optimized to avoid redundant collimators and save space and resources. Preliminary estimates make us confident that the residual halo can be housed inside the accelerator limiting aperture with this reduced set of collimators. The exact position and operating aperture of them will be determined from the final optics functions and aperture of the machine.

- Second, if the impact parameter of the particle in secondary collimators is small, there is a finite probability of grazing this jaw as in the case of primaries. Thus, exact simulations of the scattering processes taking place in the jaw are necessary before we can predict the final efficiency of the whole system.

2.6.4 Alternative collimation designs

Collimation dog-leg When working at a relatively low energy range (400-1000 MeV) the loss of energy by ionization that a proton suffers in the collimator jaw is an important fraction of its total energy and it may be enough to remove the beam halo by using a dog-leg.

The principle of operation is illustrated in figure 25. A thin scrapper layer ($\approx 1\text{cm}$) is shaped conveniently and introduced in the beam on such a way as to intercept only halo particles. When the halo proton traverses the material, their energy is less by a fraction of some percent while the angular kick received in the scrapper is negligible with respect to a small fraction of the natural divergence of the beam. Following the scrapper an achromatic bending system filters the particles with a given lack of energy while returning the central beam to their original orbit.

This system can be hosted in one or two doublet cells depending on the final bending angle and energy spread of the halo after scrapping.

Momentum scraper Momentum collimation can also possibly be performed by locating collimator jaws at places where non-zero dispersion. The specifications of the RCS machine are shown in Figure 26. The value for the dispersion at the collimator has to be close to that of the arc itself $D_x \approx 4.4\text{m}$.

Crystal collimation Crystal channelling is an attractive option to guide the beam halo into desired collimation angles. The key issues to be resolved are collimation efficiency (expected to be near 80%), crystal heating, and incoming halo acceptance.

2.6.5 Collimator design

Collimators are used to remove halo or off-momentum particles from the main proton beam. In addition to removing halo particles collimators will also act as shielding for the remainder of the accelerator structures. Thus, collimators reduce uncontrolled losses around the ring and reduce activation of the accelerator components.

Requirements and performance goals for the collimator are summarized below:

- Halo proton attenuation by a factor of 10^{-4} ,
- Minimize production of secondary radiation, and its subsequent leakage, and
- Remove heat (2 kW).

In order to meet these goals a self-shielding collimator configuration will be designed. An arrangement consisting of a layered structure will be considered. The initial layers (in the direction of the proton beam) are transparent to protons, and become progressively less transparent (blackier) with depth into the collimator. In addition, a high density (iron) shield will be added around this structure. The protons are stopped in the approximate center of the collimator, and thus the bulk of the secondary particles will also be generated there. Since these secondary particles are primarily produced isotropically their leakage path length will be maximized in this manner (high probability of capture or attenuation). In the case of neutrons a black layer is included at each end in order to further minimize their leakage in the direction of the beam. This design will therefore minimize the activation of surrounding accelerator components.

Conceptual design The conceptual design, based on the above requirements and ring constraints, is shown on Figures 28 and 27. The protons travel from left to right, with the beam confined primarily to the inner diameter of the collimator. Halo particles are found between the collimator inner diameter and the beam tube inner diameter, and are assumed to pass into the collimator volume. On their way into the collimator the halo particles will first encounter the tapered transition surface between the collimator tube and the vacuum chamber. This surface has a wall thickness of 1 cm and is made of steel. The next 15 cm consist of a borated light-water volume. This region is relatively transparent to high energy protons, but lower energy neutrons would be thermalized in this region and be absorbed by the boron. The use of borated light water to thermalize and absorb neutrons is a common practice in the light water reactor industry.

All the zones to this point have the same composition in the radial direction. The following two zones have a radial variation at a radius of 20 cm. Within the 20 cm radius they consist of randomly packed spheres cooled by borated light water, and outside this radius they consist of solid iron plates. This arrangement is chosen to ease the assembly of the collimator, ensure

heat removal, and minimize the cost. Randomly packed beds of particles are particularly efficient at heat transfer, since their area per unit volume is very large. Furthermore, the cost of small spheres of stainless steel is lower than machined discs of the same material. The void (coolant in this case) fraction of randomly packed spheres is approximately 35%, thus the solid fraction in these zones will be 65%. The particle bed zone will consist of 3 mm diameter stainless steel particles, with a length of 80 cm. The protons will lose the bulk of their energy in this zone, and since the production of neutrons per proton is modest for stainless steel, the secondary production of neutrons is relatively low. However, there is a probability of generating secondary protons in addition to the neutrons. Fortunately the yield of secondary protons is low compared to the neutron yield, due to the fact that the protons have to overcome the potential barrier before escaping the excited nucleus. Finally, the back 15 cm of the collimator consists of the same borated light water used in the first 15 cm of the collimator. This volume will ensure that many of the remaining spallation neutrons are slowed down and captured. The collimator is encased in 45 cm of solid iron on all sides. The collimator thus has an overall radius of 75 cm and a total length of 222 cm (including the iron shield).

Analysis and results The above collimator configuration was analyzed using the Monte Carlo codes LAHET [11], for particles above 20 MeV; and MCNP [12] for particles below 20 MeV. In addition, a suitably modified version of the ORIGEN [13] code was used to estimate the buildup of spallation products during machine operation, and their decay following shut-down. The proton beam is assumed to be traveling from left to right, parallel to the collimator tube. The source plane is situated at the graphite transition piece. Radially the proton beam is assumed to have a Gaussian shape. These results show that the backward (opposite to the direction of the proton beam) and forward (in the direction of the proton beam) proton currents in the halo zone of the beam (radius greater than 5 cm) decreases monotonically to the back end of the collimator. In addition, the leakage out of the front end of the collimator is also seen to be vanishingly small. Within the collimator it is seen that the proton current in the backward direction varies, with a maximum at the interface between the shield and the collimator containment vessel. The need for the thick iron shield is thus demonstrated. Thus, the proton leakage out of the back and front of the collimator meets the design goal set for it. Neutron currents (neutrons with energies above 20 MeV) were also determined. It is seen that in the forward direction the neutron current increases initially and then decreases monotonically to a low value at the outer surface. In the backwards direction the current peaks at the interface between the front shield and the collimator body.

The thick shield should minimize neutron leakage, which in turn will minimize the activation of the tunnel air. The only other activated material which can leave the collimator is the cooling water. Potentially ^7Be and ^3H are formed and circulate in the coolant. For the above reason the cooling water will be cooled in a closed loop via an intermediate heat exchanger. The maximum heat load from a collimator is 2 kW. If a temperature rise of 5°C is assumed ($T_{\text{in}}=30^\circ\text{C}$, and $T_{\text{out}}=35^\circ\text{C}$) a flow rate of approximately 3(-4)m³/s is required. This implies a moderate heat removal system for the design basis condition.

Estimates of the energy deposition in the collimator indicate the bulk of the power will be generated in the inner 20 cm of the front borated light water zone (9%), the front iron

shield (10%), and the stainless steel particle bed (70%). All these zones need to be cooled by the cooling water system. The stainless steel particle bed zone is inside the collimator and is cooled by the borated water system. Preliminary estimates of the temperature indicate that they are well within the operating limits.

In addition to the estimates of energy deposition in bulk components, an estimate of the axial and radial variation of energy deposition was made in the collimator tube, and front shell. The energy deposition was found to be quite modest, with the maximum (2.2×10^5 W/m³) occurring at the leading edge. The tube and containment shell are subject to the most challenging thermal environment, since they are cooled on one surface, and the coolant flow pattern in the leading edge corner can be ambiguous. Assuming a heat transfer coefficient of 350 W/m²-°C on the surface the maximum temperature rise per pulse is estimated to be approximately 15°C, and the implied maximum thermal stress is estimated to be 4.0(7)N/m². These values appear to be within the operating limits of the containment shell material. However, it should be pointed out that the above estimates do not account for the cyclic nature of the beam, and the possible effects due to thermal-mechanical shock enhancement of the stresses.

It was assumed that the machine has operated for 180 days at full power (1 MW, with 0.001 of the beam being captured in the collimator). Activation levels after 1 day, 7 days, and 30 days following shutdown were determined. It was found that the quadrupole magnets have an activation of x Curies. The primary activation products being ⁵¹Cr, ⁵⁴Mn, ⁵⁶Mn, ⁵⁵Fe, ⁵⁹Fe, ⁶⁵Ni, ⁶²Cu, and ⁶⁶Cu. In the iron zones of the magnet structure the same activation products are important, except Cu and Ni. The dipole magnets behind the collimator have a vanishingly small amount of radioactive buildup. The energy spectrum due to decay gamma rays was found to peak in the energy range between 0.85 MeV and 1.25 MeV. The activity of the solid components within the collimator is well shielded.

Furthermore, the question of scrapping interactions, on the collimator walls of primary protons and the production of secondary particles is being investigated. A simulation of primary proton scrapping on the walls of a conical shaped collimator with an inner diameter of 10 cm at its entrance, various included conical angles, and a length of 1 m, was carried out. The results indicate that for a scrapping angle of $0.05^\circ \sim 50^\circ$ of the particles re-emerge from the collimator, and of these 47 % are confined to a cone with an included angle of 30° . This fraction decreases monotonically with increasing included collimator angle ($\sim 40\%$ for 0.2°). The energy distribution of the emerging protons has a peak at the primary proton energy, but has a low energy tail which extends down to 100 MeV. The production of secondary electrons at SNS conditions has been estimated. First, based on a theory due to Sternglass [14, 15], and second scaled from experiments using the above theory [16]. The values of electron production per primary proton (e-/p+) vary from 200 to 25 for the above two estimates respectively. Currently, an experimental program is being carried out at BNL to study this phenomena. The objective of these experiments is to further quantify the processes involved, and more importantly to investigate possible methods of suppressing the production/capture of secondary electrons.

Finally, the possibility of incorporating a movable inner surface to the primary ring collimator is being investigated. A possible configuration is shown on Fig. 2. The inner wall is constructed in halves which move in and out radially both vertically and horizontally, to

vary the aperture. The pieces are made of copper with internal cooling loops. Initial estimates indicate that the energy deposition and neutron production is 10% - 15% higher than if a similar piece was made of stainless steel. However, due to its superior heat conduction, copper will be used in this application.

2.7 Magnets

2.7.1 Magnet requirements

Table 10: Dipole and quadrupole magnet requirements for the two synchrotrons.

Quantity	Value	unit
Dipole:		
bend angle	11.25	degree
number	64 + 1	used + reference
magnetic length	2	m
sagitta (unless curved)	4.89	cm
pole width	52	cm
gap height	19.8	cm
magnetic field	0.31 – 0.91	T
ramp rate	0 – 29.4	T/s
Quadrupole:		
Regular ring quadrupole:		
number	96 + 1	used + reference
magnetic length	0.6	m
magnetic strength, $B'/B\rho$	0.50	m ²
magnetic gradient	1.6 – 4.6	T/m
diameter	25.6	cm
peak field at pole tip	0.59	T
Large ring quadrupole:		
number	24 + 1	used + reference
magnetic length	0.75	m
magnetic strength, $B'/B\rho$	0.41	m ²
magnetic gradient	1.3 – 3.8	T/m
diameter	33.6	cm
peak field at pole tip	0.68	T
Long ring quadrupole:		
number	40 + 1	used + spare
magnetic length	1.15	m
magnetic strength, $B'/B\rho$	0.64	m ²
magnetic gradient	2.0 – 5.9	T/m
diameter	25.6	cm
peak field at pole tip	0.76	T

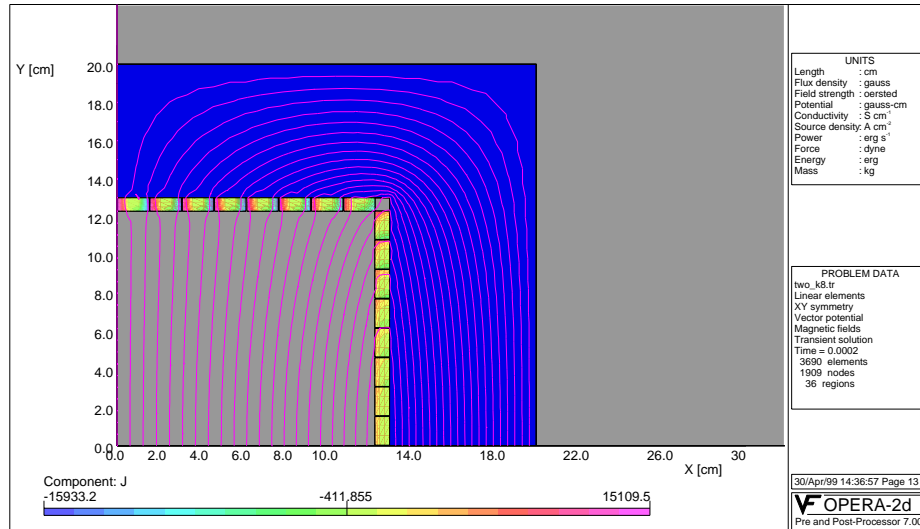


Figure 15: Eddy current effect generated in combined H/V kickers. The effect is significantly reduced by breaking down the Cu plate into 8 smaller Cu conductors.

Table 11: Sextupole and correction magnet requirements for the two synchrotrons.

Quantity	Value	unit
Sextupole:		
Regular ring sextupole:		
number	16 + 1	used + reference
magnetic length	0.2	m
magnetic strength, $B''/B\rho$	8.9	m^{-3}
diameter	25.6	cm
peak field at pole tip	0.68	T
Large ring sextupole:		
number	24 + 1	used + reference
magnetic length	0.25	m
magnetic strength, $B''/B\rho$	7.0	m^{-3}
diameter	33.6	cm
peak field at pole tip	0.73	T
Correctors:		
Quadrupole		
Skew quadrupole		
Sextupole		
Skew sextupole		
Decapole		

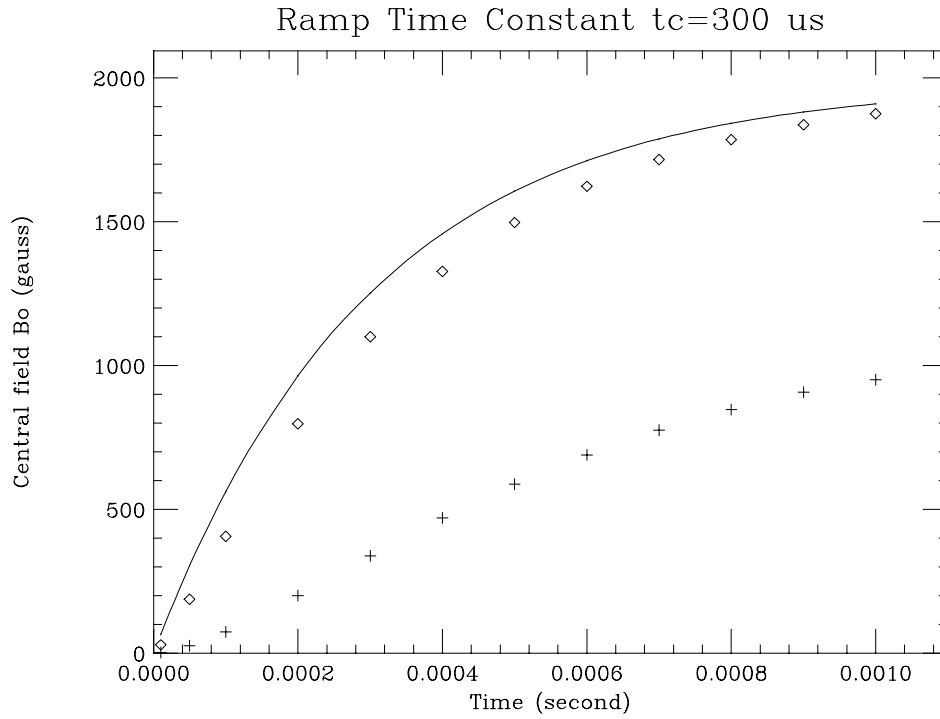


Figure 16: Comparison of the field rises with the same exponential ramp function: the solid curve stands for the ideal central field ramp along the time; the cross symbol stands for the poor field ramp suffered by eddy current effect in the Cu plate; the diamond symbol stands for the improved field ramp by using 8 smaller conductors.

Table 12: Corrector and their functions.

Chromatic sextupole	off-momentum optics matching chromaticity adjustment instability damping
Quadrupole	dipole-quad eddy current matching tune adjustment
Skew quadrupole	decoupling
Sextupole	eddy current correction resonance correction
Skew sextupole	resonance correction
Octupole	damping, resonance correction

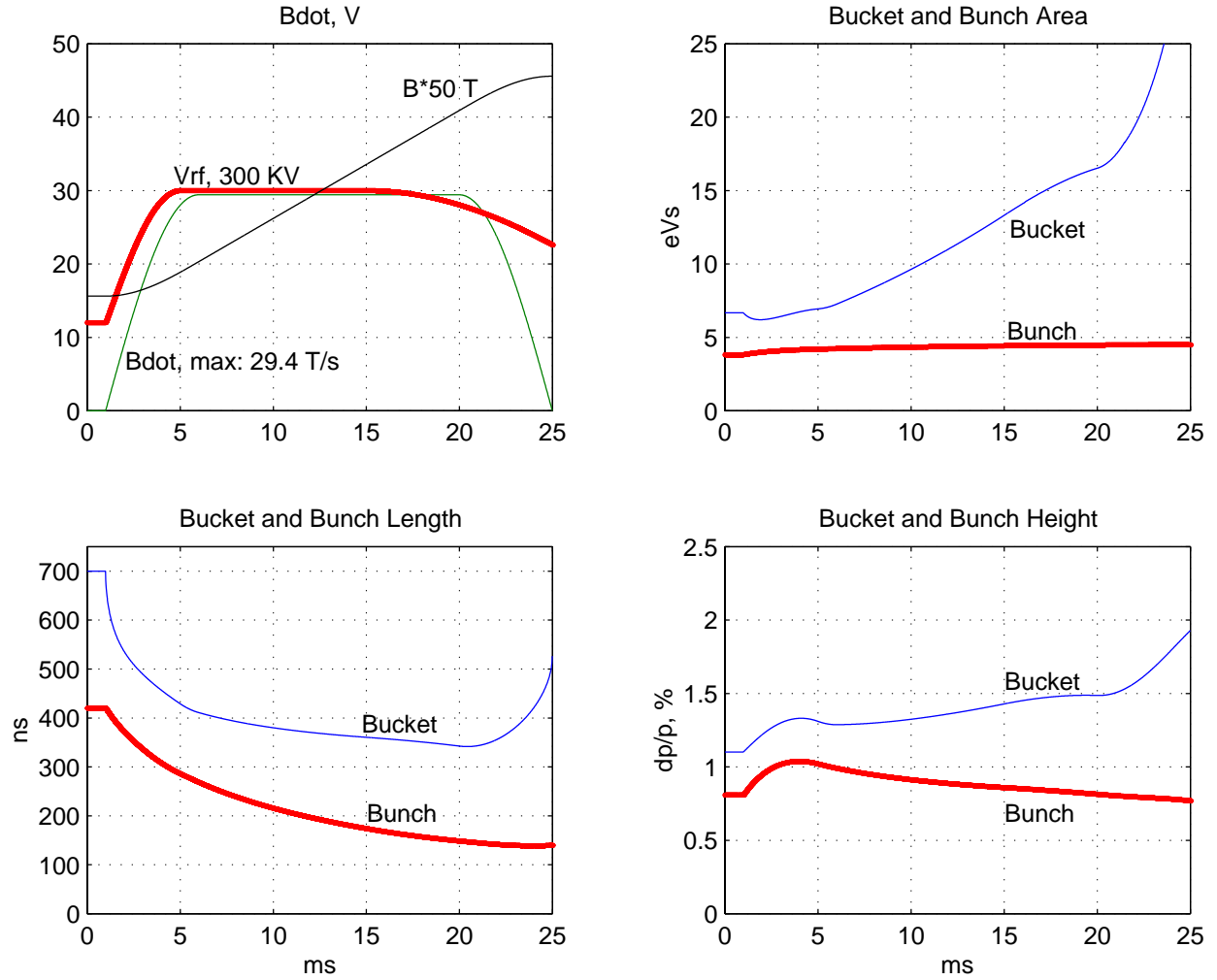


Figure 17: Programming of RF voltage and magnetic field, and the evolution of momentum spread, bunch area and bunch width in comparison with the ($h = 2$) RF bucket.

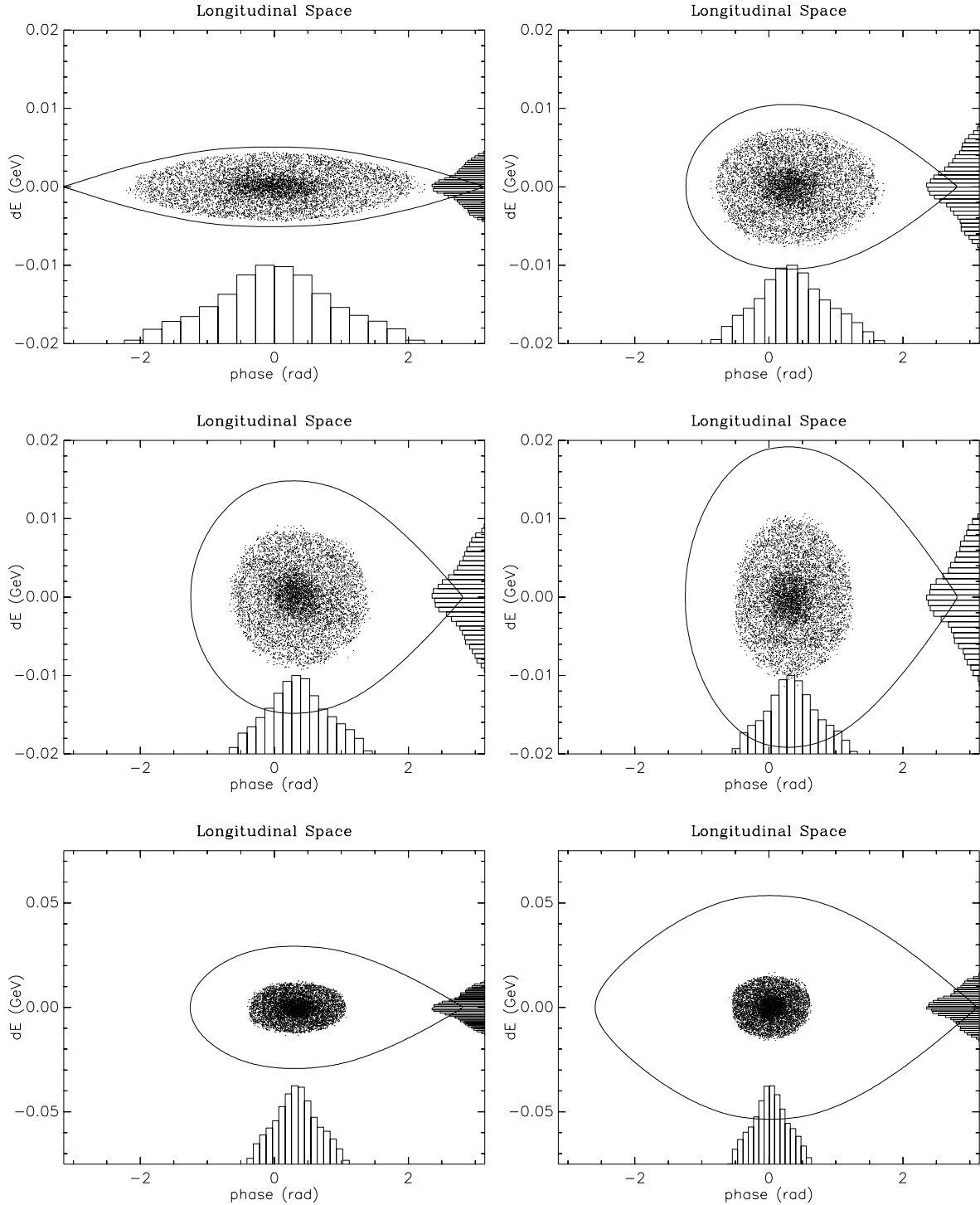


Figure 18: Simulation at 0.7, 4.2, 7.3, 10.2, 15.8, and 22 msec from the beginning of injection during the ramping. A single ($h = 2$) RF system is used with a peak voltage of 300 kV.

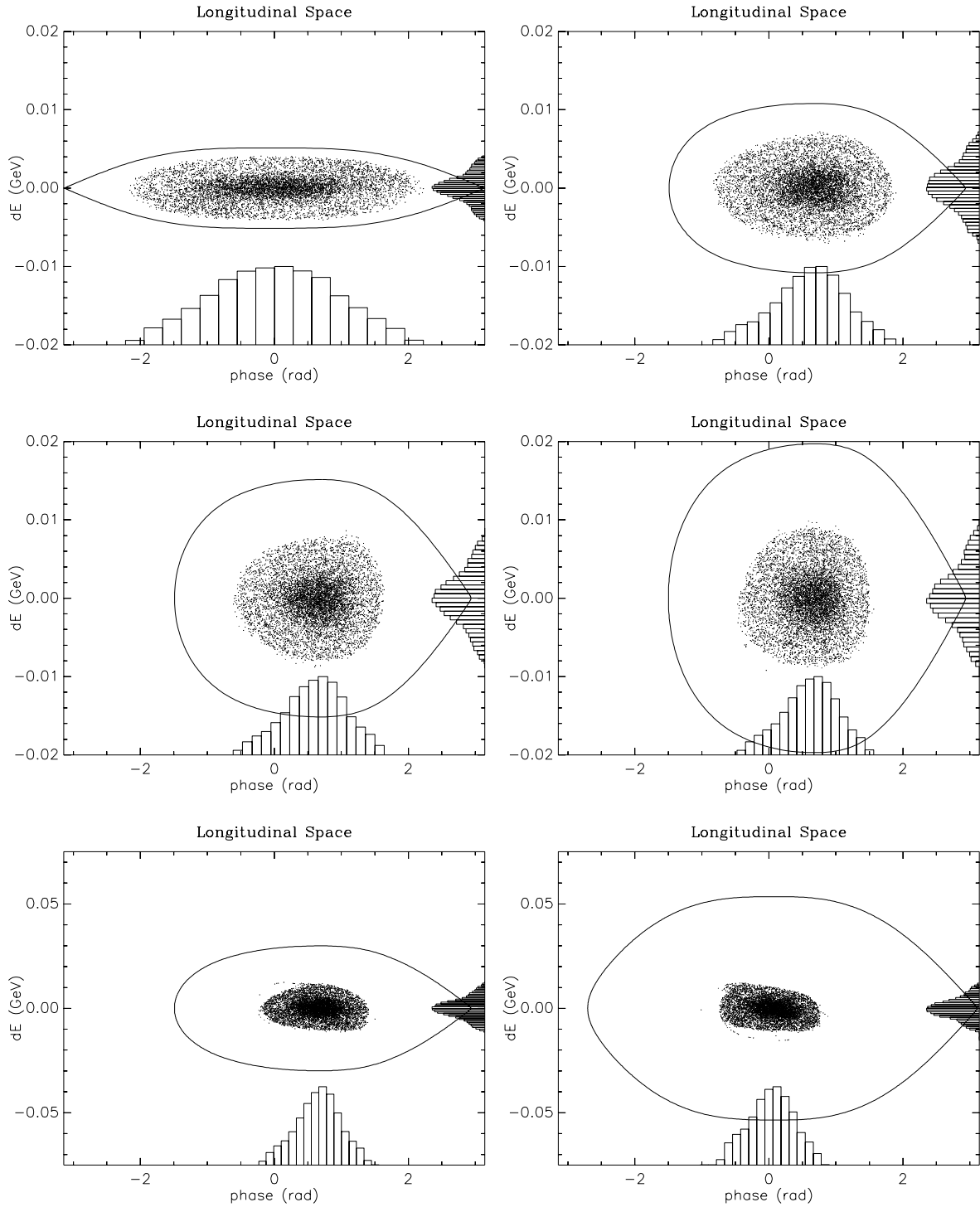


Figure 19: Simulation at 0.7, 4.2, 7.3, 10.2, 15.8, and 22 msec from the beginning of injection during the ramping. A dual ($h = 2$ and $h = 4$) RF system is used with a peak voltage of 300 kV.

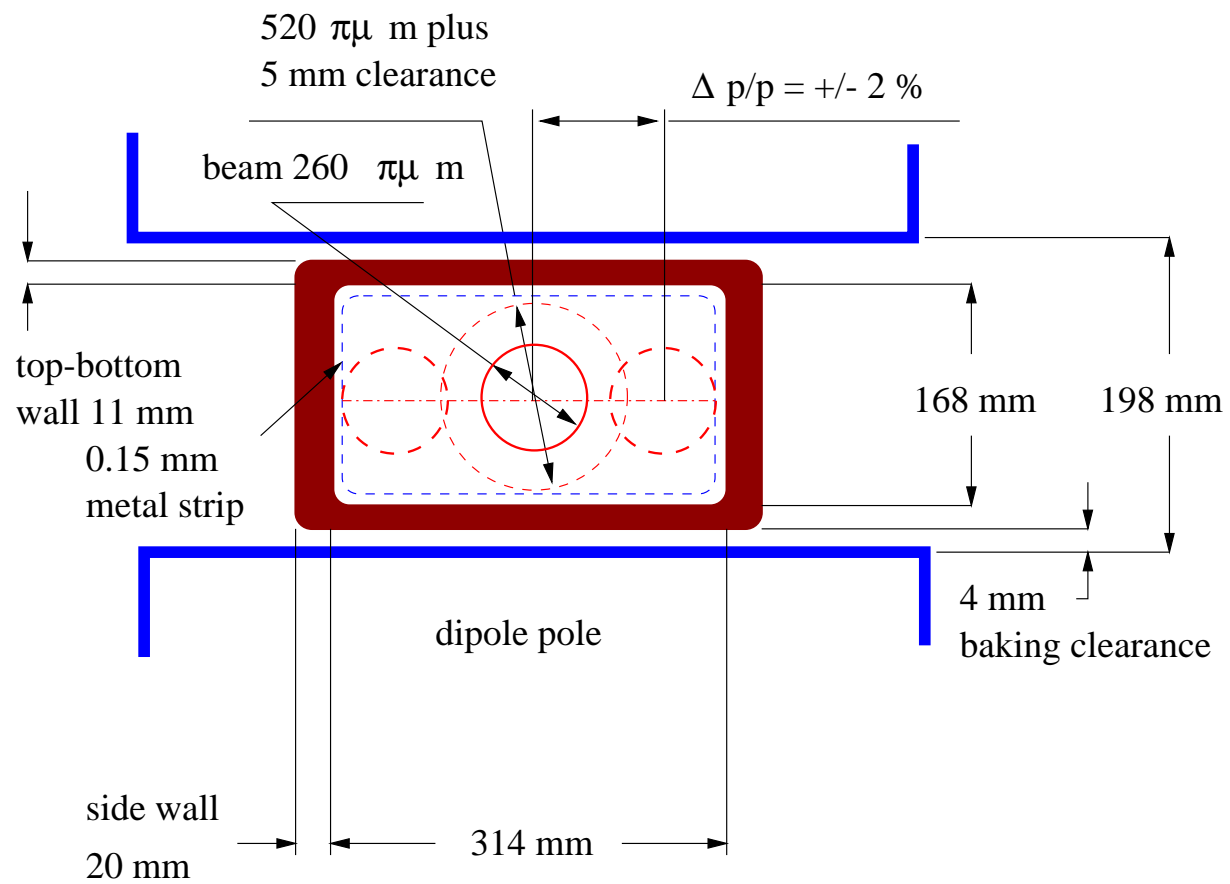


Figure 20: Dipole magnet chamber and aperture clearance.

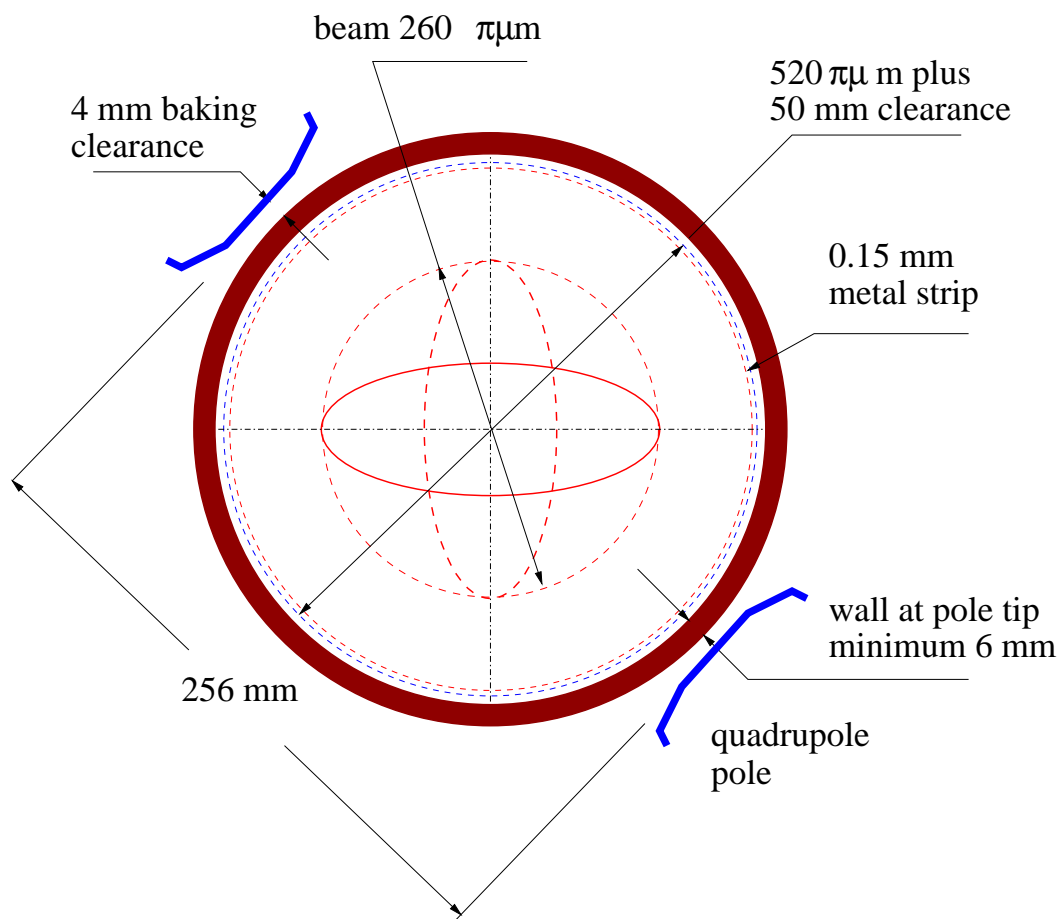


Figure 21: Regular quadrupole magnet chamber and aperture clearance.

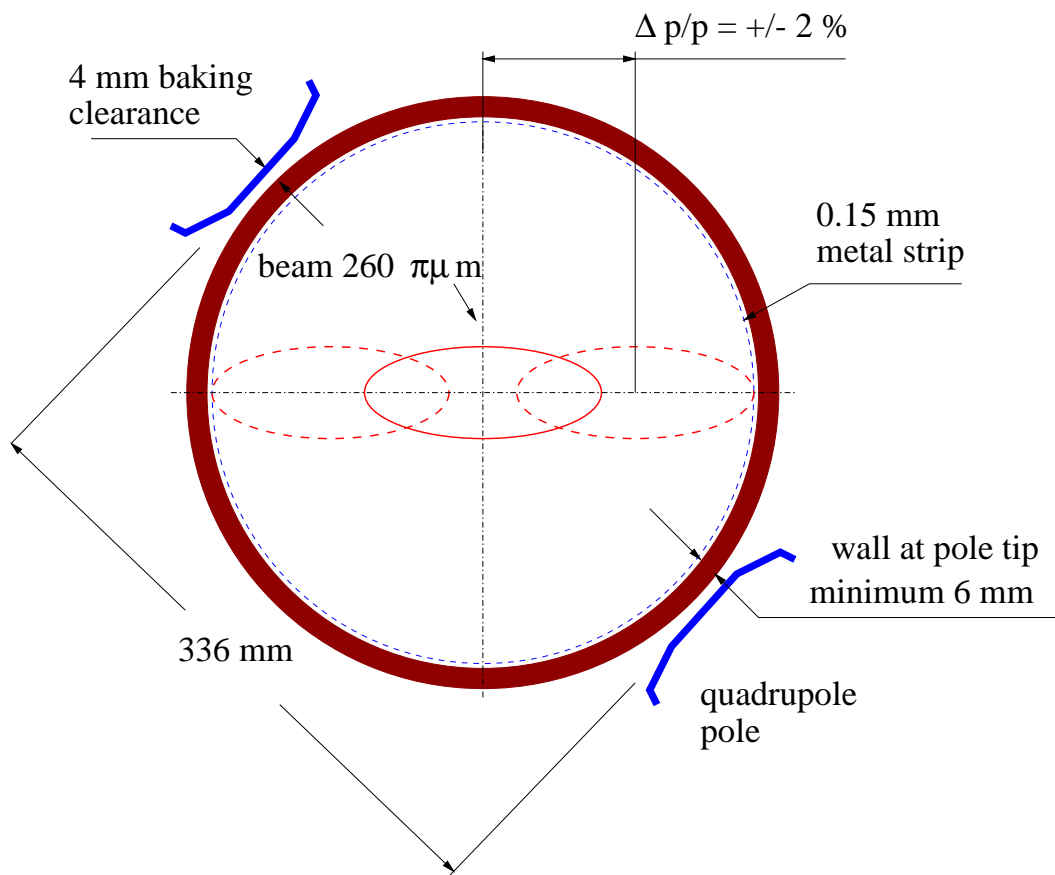


Figure 22: Large quadrupole magnet chamber and aperture clearance.

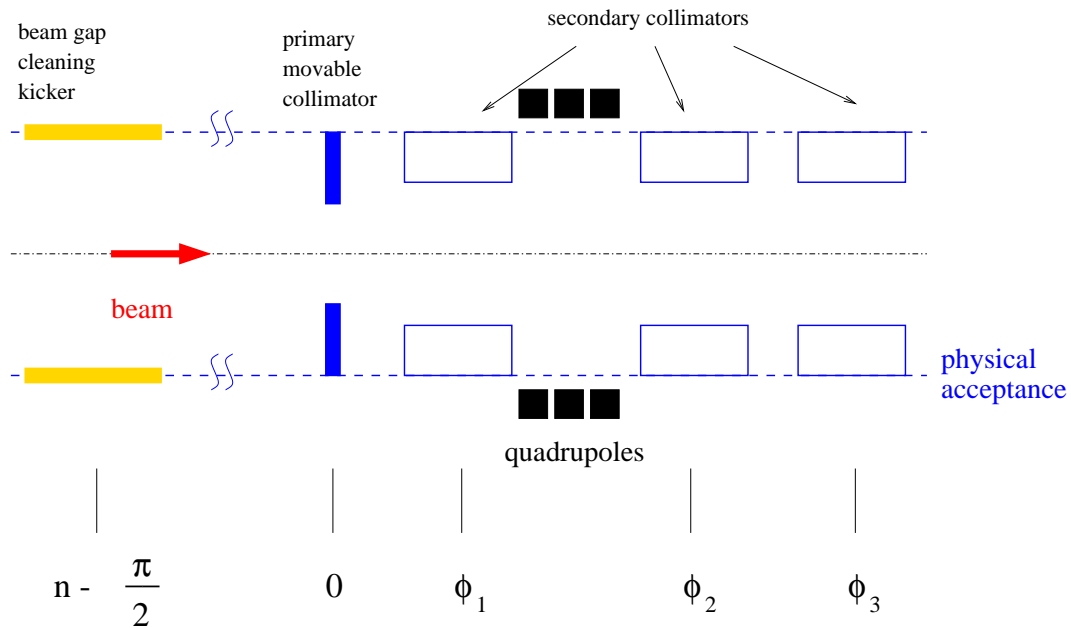


Figure 23: Schematic layout of SNS ring beam gap cleaning and collimation devices. The collimators are housed and shielded in a single straight section.

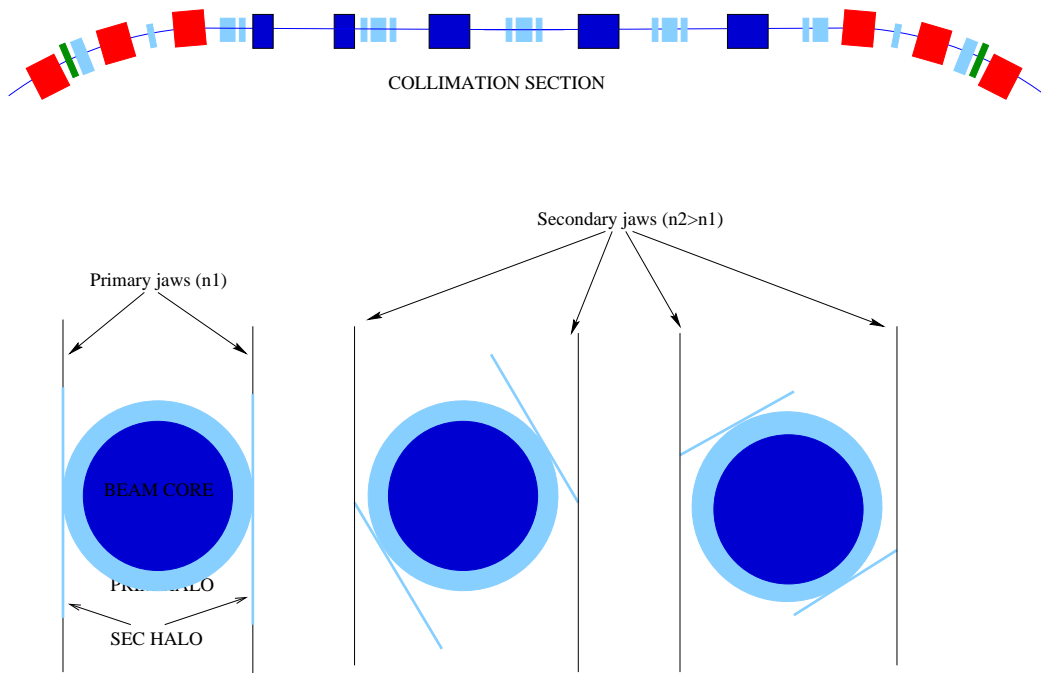


Figure 24: Schematic layout of RCS betatron collimation.

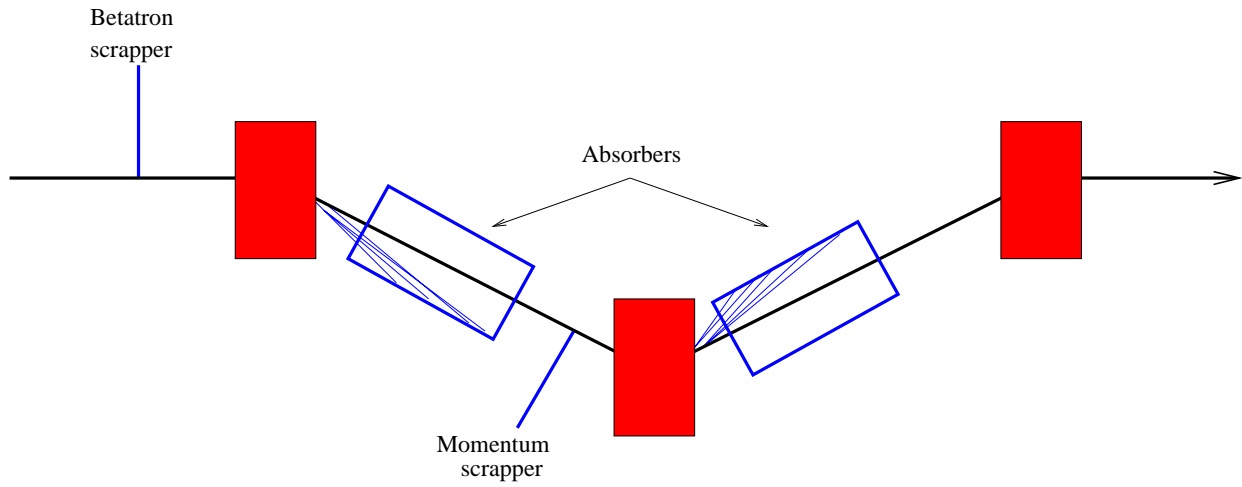


Figure 25: Schematic layout of the collimation dog-leg.

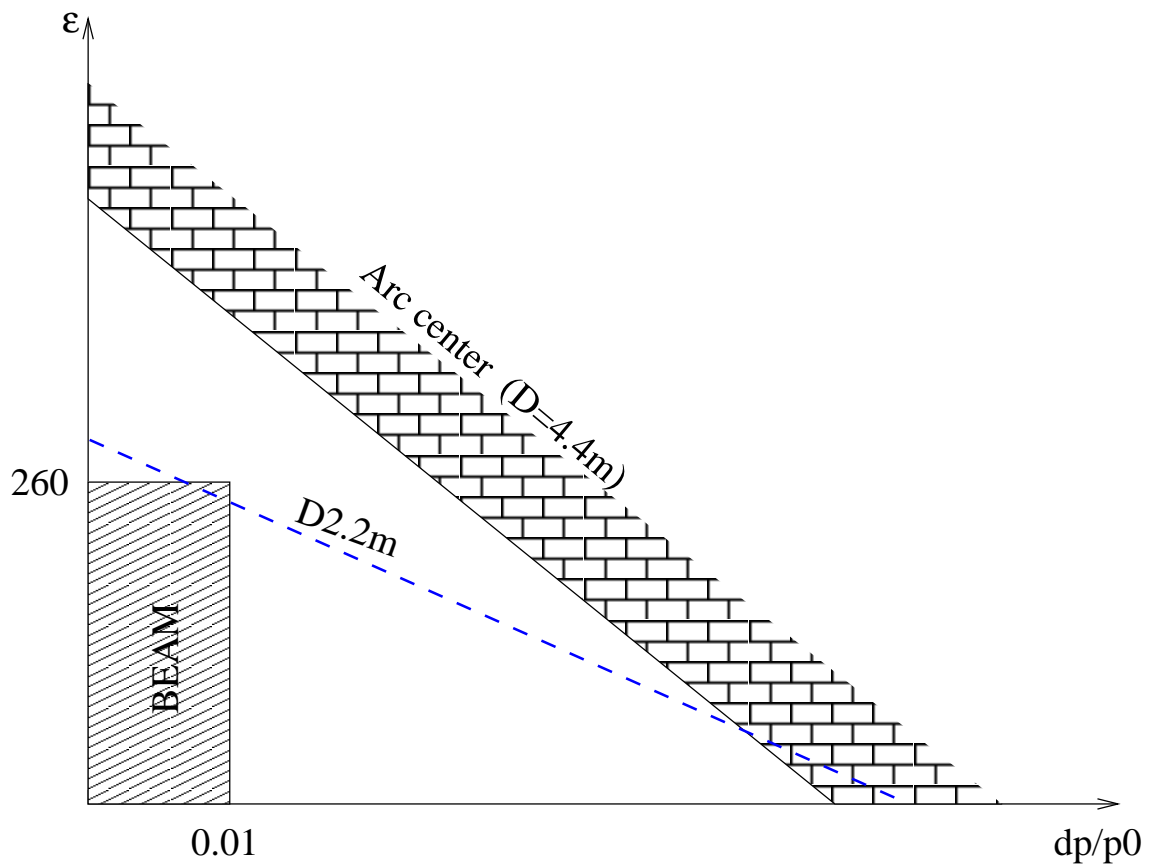


Figure 26: Schematic layout of possible momentum collimation.

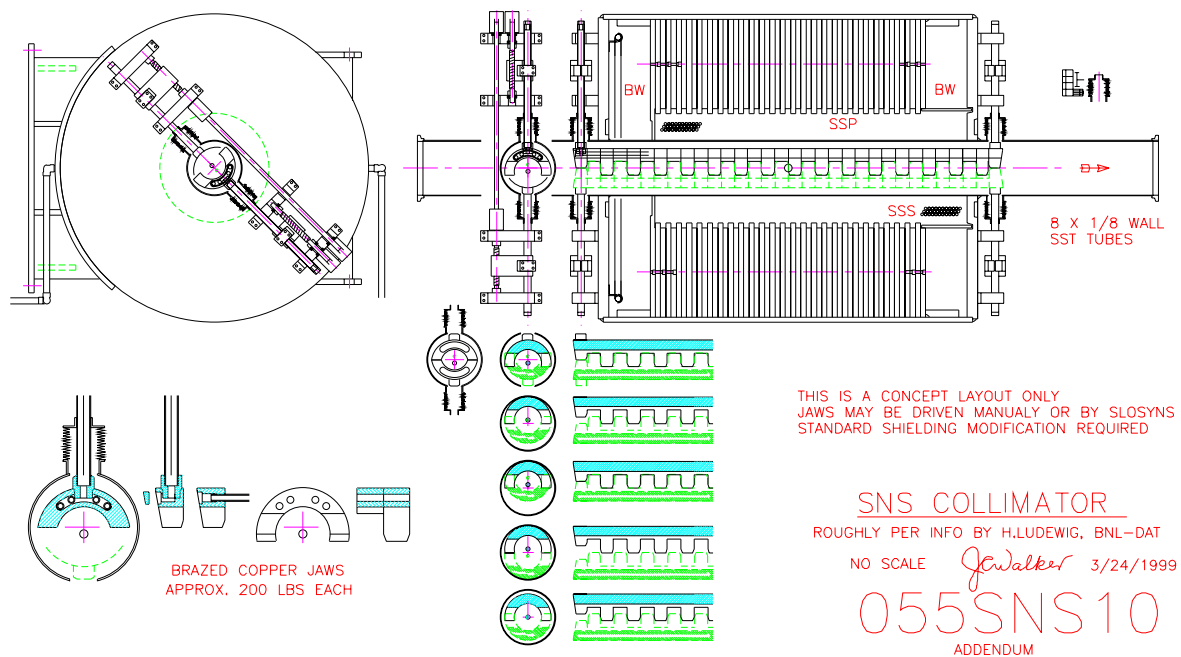


Figure 27: Adjustable collimator design.

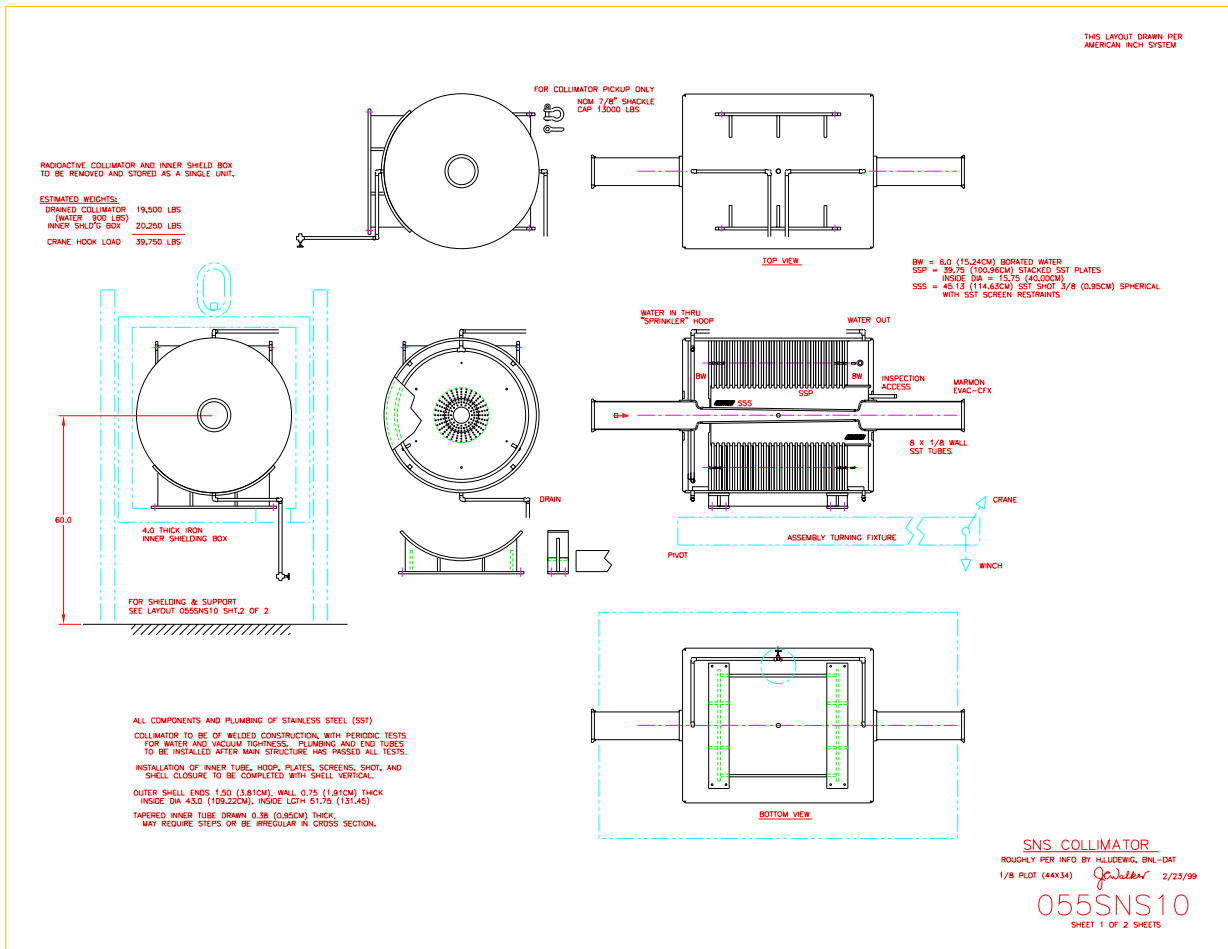


Figure 28: Fixed collimator design.

2.7.2 Expected magnetic field errors

Table 13: Magnet transfer function deviation due to magnetization, ramping eddy current, Saturation, and magnet-to-magnet cross talk. The ramp rate is assumed to be 30 T/s, and the saturation corresponds to the extraction field.

Quantity	Value	unit
Dipole:		
Eddy current	1.1	%
Magnetization	0.22	%
Saturation	1.0	%
Cross talk		
Quadrupole:		
Eddy current	0.5	%
Magnetization	0.2	%
Saturation	2.0	%
Cross talk		

- (a) Magnet ends shaped to minimize field saturation mismatch.
- (b) Hi silicon tram-steel used to minimize magnetization.

2.7.3 Expected magnet misalignments

Table 14: Expected magnetic errors of ring dipoles at the injection flat bottom.

n	Normal		Skew	
	$\langle b_n \rangle$	$\sigma(b_n)$	$\langle a_n \rangle$	$\sigma(a_n)$
Body	[unit]			
3	-0.2	0.0	0.0	0.0
5	0.8	0.0	0.0	0.0
7	-0.8	0.0	0.0	0.0
9	-3.0	0.0	0.0	0.0
11	-4.4	0.0	0.0	0.0
13	-2.4	0.0	0.0	0.0

(a) Based on 2D calculation of SNS ring dipole design

(b) Normalized to 10^{-4} of the main field at the reference radius R_{ref} of 15 cm.

Table 15: Expected magnetic errors of ring quadrupoles at the injection flat bottom.

n	Normal		Skew	
	$\langle b_n \rangle$	$\sigma(b_n)$	$\langle a_n \rangle$	$\sigma(a_n)$
Body	[unit]			
3	0.0	-2.46	0.0	-2.5
4	0.0	-0.76	0.0	-2.0
5	0.0	-0.63	0.0	1.29
6	0.2	0.0	0.0	1.45
7	0.0	0.02	0.0	0.25
8	0.0	-0.63	0.0	0.31
9	0.0	0.17	0.0	-0.11
10	0.70	0.0	0.0	1.04
11	0.0	-0.06	0.0	-0.05
12	0.0	-0.22	0.0	-0.09
13	0.0	-0.06	0.0	0.08
14	-1.41	0.0	0.0	0.26

(a) Based on AGS Booster quad integral measurement data.

(b) Normalized to 10^{-4} of the main field at the reference radius R_{ref} . For regular ring quadrupoles, $R_{ref} = 12$ cm; for regular ring quadrupoles, $R_{ref} = 15$ cm (approximately 92% of the quadrupole iron pole tip radius).

Table 16: Expected sextupole (b_3) error component of the dipole magnets due to magnetization, ramping eddy current, Saturation, and magnet-to-magnet cross talk. The ramp rate is assumed to be 30 T/s, and the saturation corresponds to the extraction field.

Quantity	Value
Eddy current	15 u
Magnetization	1 u
Saturation	5 u
Cross talk	

- (a) Sextupole (b_3) content scaled from Booster measurement data.
- (b) Normalized to 10^{-4} of the main field at the reference radius R_{ref} of 15 cm.

Table 17: Expected dodecapole (b_6) error component of the quadrupole magnets due to magnetization, ramping eddy current, Saturation, and magnet-to-magnet cross talk. The ramp rate is assumed to be 30 T/s, and the saturation corresponds to the extraction field.

Quantity	Value
Eddy current	9 u
Magnetization	1 u
Saturation	
Cross talk	

- (a) Value scaled from Booster measurement data.
- (b) Normalized to 10^{-4} of the main field at the reference radius R_{ref} . For regular ring quadrupoles, $R_{ref} = 12$ cm; for regular ring quadrupoles, $R_{ref} = 15$ cm (approximately 92% of the quadrupole iron pole tip radius).

Table 18: Expected alignment errors of ring magnets.

Item	Value
Ring dipole sagitta deviation (unless curved)	4.89 cm
Magnetic center position ^{a,b} (rms)	0.1 – 0.5 mm
Magnet longitudinal position ^b (rms)	0.5 mm
Mean field roll angle ^{a,b} (rms)	0.2 – 0.5 mr

- (a) Based on AGS Booster dipole and quad manufacturing data
- (b) Based on actual survey of AGS-to-RHIC transfer line magnets
- (c) Based on the expected improvement from end shaping

2.8 Power Supply

2.8.1 Selection criteria

The Rapid Cycling Synchrotron (RCS) option for the SNS presents several critical choices in its technical design process. These are fundamental decisions for the ultimate high performance operation of the 2 MW SNS facility. The choices are driven mostly by the high frequency (30 Hz) pulse repetition operation of each of the two accelerator rings and by the low-loss requirement of the machines. The choices are predominantly in the general accelerator areas usually classified as: Injection, RF acceleration, Magnet and Power Supply, and Vacuum.

This section will concentrate on Injection, RF, and Power Supply, since there are tradeoffs that can be made between these. Any accelerator requires close control of the main magnet excitation during the period of injection, i.e. capture during beam stacking and early acceleration (see also sections 2.3 and 2.4). Thus, one of the most desirable properties of the Power Supply scheme is that it be programmable to give the proper \dot{B} during this early but very important part of the machine cycle. This determines the dominant losses of the rings.

The other major properties of the Power Supply is that its ramp-up during acceleration exhibit as close to a linear rise as possible, using as low a slope as possible. These will enable the requirement for the amount of RF accelerating potential to be minimized (see RF section 2.4). The RF cavities, which have a limited MV/meter, otherwise will occupy a large fraction of the machine straight-section space and increase the costs of the RF and the ring appreciably.

In all of the above, as well as in the design of the ring magnets and vacuum chambers, the critical parameter is the maximum \dot{B} value in the main ring guiding and focussing magnetic fields. This quantity causes eddy currents to flow in metallic volumes and results in undesirable heating and distortions in magnetic fields. Thus, it is most important to reduce this quantity to as low a value as is reasonable. The linear rise, which uses as much of the cycle as possible (in our pre-conceptual design we plan for ~ 20 msec rise time) accomplishes this very effectively.

2.8.2 Options, selection and discussions

For the reasons given above, the RCS Power supply option we have chosen for our baseline conceptual design is a linear, programmable excitation system which utilizes modern solid-state controllable devices. Realizing a linear scheme however, while it appears to be a straightforward extension of existing technology, will require a large amount of R & D to produce units of high peak ratings. More will be described regarding this in section 2.8.3 below. The main reason for the complexity is that the Main Ring magnets require large amounts of stored energy due to the large gaps needed to accommodate the high intensity beams. Ultimately, in any design, the stored energy has to be carefully controlled so that it flows to the right places at the right times.

The following describes the various powering schemes that were considered for a linear excitation as well as a simple resonant circuit. In all of these the peak energy is of major concern. The AC line will not support the huge power swings and therefore energy storage of some form would have to be provided. This can be in the form of capacitors, mechanical rotating mass, or inductive storage.

2.8.2.1- Switchmode PS modules using IGBT (Insulated Gate Bipolar Transistor) technology. These will be powered directly off the AC line with individual storage derived from transformer and rectifier/DC capacitors.

2.8.2.2- Switchmode PS modules powered by a common, large, DC generator buffer system.

2.8.2.3- SCR (Silicon Controlled Rectifier) PS modules of ratings which have been built by industry. This option will definitely require an energy storage such as an AC generator or inductor/controlled rectifier.

2.8.2.4- SCR PS modules powered by a higher frequency (300 - 400 Hz) AC generator. This will have advantages of improved ripple and increased speed of response.

2.8.2.5- Resonant biased cosine wave excitation with the energy stored in local capacitors.

The design of the PS system is dominated by the huge amounts of energy flow at the pulse repetition time of the rings, i.e. 30 Hertz. The preliminary values per ring are approximately 200 MW swings during acceleration and 400 MW during the invert or energy recovery part of the cycle. These very large amounts dictate that energy storage of some form must be employed since an AC line cannot support large swings without causing unacceptable "voltage flicker". This storage adds cost to the PS system. We have attempted to optimize the conceptual design by considering several machine design possibilities. There are definitely more options or combinations that require further optimization. In our decisions we have considered a larger ring circumference, a reduction of the magnetic field volumes (gap size), or ultimately a higher injection energy. These will require time and further study for technical and cost refinements.

2.8.3 Challenges

As indicated above, a linear/programmable option selected for the SNS RCS will require R & D to come up with a well-designed, reliable Switchmode module of high ratings (5 - 10 MW). The energy storage question must also be solved either as capacitors, inductors, or rotating mechanical mass.

As a backup, SCR modules can be used. These offer a wider choice of solid state devices of adequate ratings and modules have been constructed by commercial firms. However, in this case the energy storage problem becomes more acute and a rotating mass (MG sets) of large rating would have to be provided. This has implications for initial, installation and operational costs.

The R & D effort is estimated as follows:

2.8.3.1- High Power IGBT Module	12-15 MOS	1M\$
2.8.3.2- Power/Stored Energy Optimiz	3 MOS	0.1M\$
2.8.3.3- High Freq Mag (D, Q) Design	12-15 MOS	0.7M\$
2.8.3.4- Ceramic Vacuum Chambers	12 MOS	0.3M\$

2.9 Radio-Frequency System

2.9.1 Requirements

The RCS cycle involves charge exchange injection for 0.6 ms followed by acceleration over 20 ms and extraction. A ring circumference of 300 m with 400 MeV protons implies an injection revolution frequency $f_0 = 713$ kHz. At 2 GeV, $f_0 = 947$ kHz. The ring contains 1.04×10^{14} protons corresponding to a DC beam current of 11.9 A at injection, rising to 15.8 A at extraction. Assuming a linear ramp in magnetic field the peak rf power supplied to the beam is 1.5 MW and corresponds to a net accelerating voltage $V \sin(\phi_s) = 90$ kV/turn. A clean gap of length $\gtrsim 300$ ns is needed for the extraction kicker rise time. A large bunching factor, $B = I_{ave}/I_{peak}$ is needed to keep transverse space charge forces small. A large momentum spread $|p - p_0|/p_0 \approx 0.01$ is required to smooth the beam profile and help damp instabilities.

2.9.2 General considerations

Take $h = 2$ for the primary harmonic. This allows for an adequate extraction gap while keeping the rf frequency high enough for manageable cavity sizes. There are 8, 6.5 m straight sections available for rf cavities. With pumping ports, bellows, diagnostics etc. it is assumed that 5 m of each straight is available for the rf cavity measured flange to flange. With 50 kV per cavity a total of 400 kV/turn is available. Six of the cavities will be used for $h = 2$ and two for $h = 4$.

2.9.3 Cavity

Design for a gap voltage of $V_g = 25$ kV. This allows for a conservative design without submerging the ferrite stack in an insulating fluid. Take 2 equal stacks of ferrite per gap and two gaps per cavity. Use gap capacitance to shift between $h = 2$ and $h = 4$ so all cavities have the same design. Shorter $h = 4$ cavities are possible at additional cost.

The amount of ferrite required depends on the peak value of the rf magnetic field in the ferrite, B_{rf} . The AGS Booster cavities operate with $B_{rf} \lesssim 40$ mT and an average value of $B_{rf} = 30$ mT with comparable frequencies. The same ferrite, Phillips 4M2, will be used in the RCS so the design assumes $B_{rf} = 30$ mT. Let a and b be the inner and outer radii of the ferrite stack and ℓ be its length. From Faraday's Law

$$V_g = \omega_{rf} \Phi_B = \omega_{rf} B_{rf} \ell a \log(b/a)$$

where $\omega_{rf} = 2\pi h f_0 \geq 9.0 \times 10^6 \text{ s}^{-1}$. Take $a = 17.5$ cm and $b = 25$ cm for the inner and outer radii of the ferrite rings. Using harmonic 2 and allowing for full voltage at minimum ω_{rf} implies $\ell = 1.5$ m of ferrite per gap. A cooling plate thickness of $1/4$ " and a ferrite thickness of 1 " implies a full stack length of 1.88 m per gap. For a two gap cavity in a 5 m straight section there is a total of $5 - 2 \times 1.88 = 1.24$ m for the two accelerating gaps, the tank, the shroud, and the 2 flanges.

With $B_{rf} = 30$ mT the measured power dissipation in the ferrite is 260 mW/cc and with bias one expects the dissipation to be fairly uniform with radius. At $V_g = 25$ kV the power dissipated in the ferrite is $P_f = 39$ kW per gap yielding a cavity shunt impedance of $R_f = V_g^2/2P_f = 8.0$ k Ω per gap, where the f subscript corresponds to properties of the ferrite

Table 19: RF requirements per synchrotron ring.

Quantity	Value	unit
Ring ($h = 2$):		
RF harmonics	2	
Peak RF voltage, $h = 2$	300	kV
RF frequency, $h = 2$	1.43 – 1.90	MHz
Available space for RF systems	6 cells	
Number of cavities	6	
Peak RF voltage per cavity	50	kV
Peak RF power per cavity	1.2	MW
Peak RF power to beam	1.5	MW
Ring ($h = 4$):		
RF harmonics	4	
Peak RF voltage, $h = 4$	100	kV
RF frequency, $h = 4$	2.86 – 3.80	MHz
Available space for RF systems	2 cell	
Number of cavities	2	
Peak RF voltage per cavity	50	kV
Peak RF power per cavity	0.6	MW
HEBT (RF stabilizer):		
Peak RF voltage		MV
RF frequency		MHz
Available space for RF systems	1 half cell	
Number of RF cavities		
HEBT (RF wobbler):		
Peak RF voltage		MV
RF frequency		MHz
Available space for RF systems	1 half cells	
Number of RF cavities		

2.9.4 Power amplifier

Design for full cancellation of beam current at injection and a tuned load during acceleration. Power 2 gaps per amplifier with coupling to one of the two ferrite stacks per gap. The amplifier sees half the gap voltage but must supply 4 times the gap current. We will consider only the $h = 2$ system since it will supply most of the accelerating power and be subject to the most beam loading

During the acceleration ramp the amplifier sees a purely resistive load. With six $h = 2$ cavities the amplifier must supply a total rf power of $P_{amp} = 2 \times 39 \text{ kW} + 1.5 \text{ MW}/6 = 328 \text{ kW}$, which is the sum of the power dissipated in the ferrite and the power accelerating the beam. The harmonic amplitude of the gap voltage is $V_g = 25 \text{ kV}$ and $P_{amp} = VI_g/2$ where I_g is the harmonic amplitude of the gap current; $I_g = 26.5 \text{ A}$.

Taking a voltage swing of $\pm 12.5 \text{ kV}$ at the anode and assuming a minimum anode voltage of 2.5 kV gives an anode voltage $V_A = 15 + 12.5 \cos(\phi) \text{ kV}$ where ϕ is rf phase. For 328 kW of rf power the $h = 2$ component of the anode current has an amplitude of 53 A . A realistic situation is shown in the figure. The plotted anode current and voltage have the correct Fourier amplitudes and correspond to 212 kW of anode power.

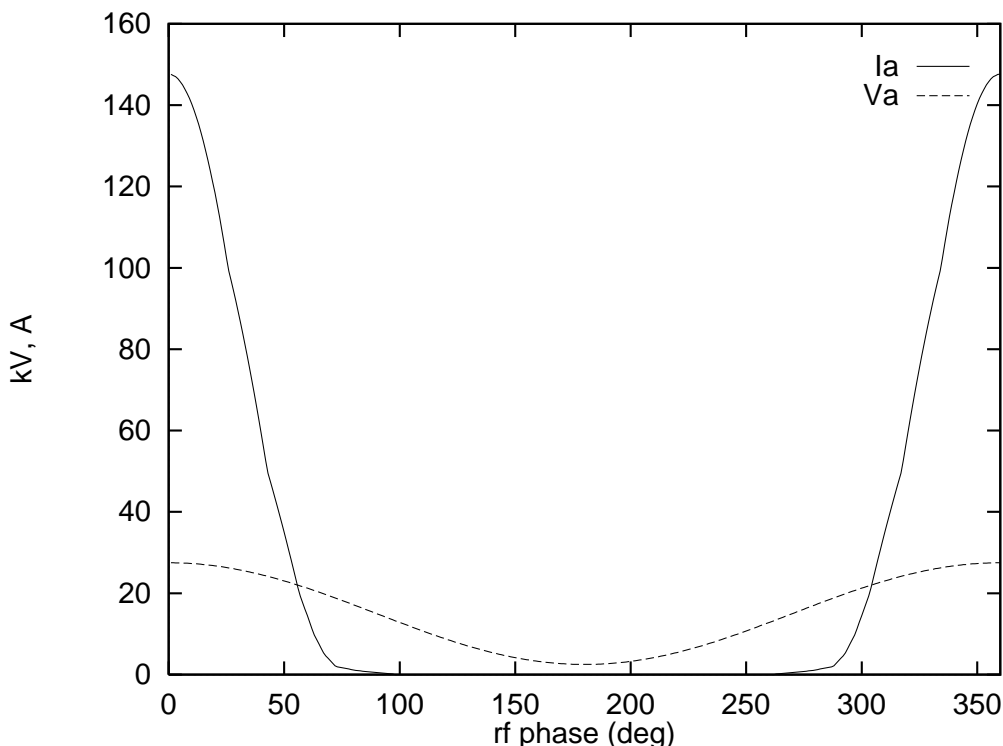


Figure 29: RF.

During injection the cavity will be tuned so that the power amplifier sees a resistive load at the end of injection. Taking $I_{beam,rf}/I_{beam} = 1.5$ implies that the power amplifier rf current is $4I_{beam,rf} = 72 \text{ A}$ at the start of injection. Taking the same 15 kV quiescent voltage and assuming a reactive load the minimum anode dissipation is 540 kW . For short bunches,

$I_{beam,rf}/I_{beam} = 2$ and the anode dissipation rises to 720 kW. Since this current is required for only 0.5 ms a 600 kW tube rating should be sufficient.

Depending on reliability and price the amplifier may use one large tube or two smaller tubes in a push-pull configuration. In any case each anode supply will need to provide about 600 kW with a 70% duty factor.

2.9.5 Beam loading and stability

The worst beam loading occurs during injection with ~ 100 kV per turn. For a beam loading parameter equal to two[9] the effective resistance of the cavity and amplifier as measured at the gap is $R_e = 2V_g/I_{beam,rf} \lesssim V_g/I_{beam} = 700\Omega$. This is quite small compared to the 8 k Ω ferrite resistance so the effective resistance of the amplifier as seen at the gap must be less than R_e . There is a factor of 8 amplification due to the number of gaps and the 2:1 transformer ratio implying a peak anode resistance of $R_a \lesssim R_e/8 = 88\Omega$. A Thompson TH558 tetrode with a 600 kW rating operating near 600 kW has $R_a \approx 400\Omega$. Taking 400 Ω as the fiducial amplifier resistance implies a factor of 4.6 impedance reduction for marginal stability.

With rf feedback the value of R_e can be reduced. A conservative limit is given by [10]

$$\min(R_e) = \left(\frac{R_f}{Q_f} \right) 4f_{rf}\tau_{delay},$$

where Q_f is the quality factor of the cavity without the amplifier and τ_{delay} is the net delay of the feedback loop. This is the resistance across at gap. Assuming a parallel LRC resonator for the cavity, $R_f/Q_f = \sqrt{L/C}$ where L and C are the inductance and capacitance of the cavity, respectively. Taking $\mu_r = 81$ for the biased permeability of the ferrite gives $L = 8.7 \mu\text{H}$ and $R_f/Q_f = \omega_{rf}L = 78\Omega$. The maximum gap impedance is 700 Ω so $f_{cav}\tau_{delay} \leq 2.2$. This is well within the state of the art.

2.9.6 Low level rf beam control

The rf system will be equipped with 1. a phase loop to damp coherent dipole oscillations, 2. a radial control loop for maintaining the synchronous energy, 3. automatic level control on each cavity, 4. a tuning servo that keeps the rf cavity at the optimal resonant frequency during acceleration. With two bunches the growth rates of coupled bunch modes are very small so no bunch by bunch damping is planned. The rings will have a fast longitudinal pickup and two transverse pickups in dispersive regions separated by $\approx 180^\circ$ of betatron phase.

Since there are six $h = 2$ cavities some sort of phase shifter is required to keep the voltage contributions of individual cavities in phase. This is easily achieved with modern rf technology.

The low level control system will use an on-line measurement of the magnetic field in the ring to pre-program the rf frequency and control the precise timing of beam extraction. Typically this measurement is made in a reference magnet located outside the ring but electrically connected in series with the ring magnets. A ring vacuum chamber is included in the reference magnet so that eddy currents are automatically accounted for.

2.9.7 Second harmonic system

A second harmonic ($h = 4$) system capable of generating 100 kV per turn is planned. This system will improve the bunching factor and provide synchrotron frequency spread to damp instabilities. Fast rf feedback will be present and the relative phase of the second harmonic voltage with respect to the first harmonic will be slaved to a user defined function. No separate phase or radial loops in the second harmonic system are planned, but the cavities will have tuning loops and automatic gain control.

While the $h=4$ system may require less power per station than the $h=2$ system the possibility of faults in the $h=2$ system suggests that the $h=4$ systems be easily converted into $h=2$ systems. Using less ferrite in the $h=4$ cavities or reducing their drivers limits the ability of the $h=4$ system to “fill in” while the $h=2$ system is off line. The engineering of the second harmonic system will be done with the possibility of rapid conversion in mind.

2.9.8 Summary

The RCS rf system involves proven technology and is a straightforward extension of rf systems currently operating at Brookhaven. With stacked rings, maintainability and accessibility will need careful design consideration. A large voltage per turn allows for a small synchronous phase and a long bunch. Heavy beam loading is overcome by using sufficient rf power and fast rf feedback. The system will allow for a sufficiently large bunching factor and momentum spread to ensure stable operation. A dual harmonic system is the baseline design which meets the performance requirements. The hardware configuration is compatible with a fall back to a single harmonic system. The system is robust to single point failures, by going to the single harmonic mode but a ring entry to remove capacitors on the $h = 2$ system is required.

2.10 Vacuum System

The operating pressure of the RCS vacuum system will be in 10^{-8} Torr range and is needed to minimize the beam-residual gas ionization. The dipole and quadrupole chambers will be fabricated out of high strength alumina to reduce the eddy current effect of the fast cycling magnets.

2.10.1 Vacuum considerations

The following beam-residual gas interactions are considered in assessing the required vacuum levels in RCS; nuclear scattering, multi-coulomb scattering and residual gas ionization. The nuclear scattering cross sections are usually less than 3×10^{-25} cm² for most common residual gases. The beam loss due to nuclear scattering will be less than 1×10^{-6} over 25 msec at a vacuum of 1×10^{-8} Torr. The multi-coulomb scattering causes growth of the rms beam size. The fractional growth will be less than 1×10^{-5} over 25 msec at the design vacuum of 10^{-8} Torr.

The residual gas ionization sets the most stringent requirement on the vacuum levels. The ionization cross sections of protons on the residual gas molecules are usually less than 2×10^{-18} cm² at RCS energy range. With a gas density of 3×10^8 molecules/cm³ at the design vacuum, there will be $\sim 1 \times 10^{-1}$ ionization per proton over the 25 msec cycle. The newly created ions repelled by the beam-wall potential will bombard the chamber wall and desorb molecules. The ionized electrons could be trapped in the potential well of the beam causing partial neutralization of the beam, or they could bombard the chamber wall and liberate more secondary electrons.

The ion desorption coefficient h , the number of molecules desorbed per incident ion, depends on the material and surface treatment of the chamber wall and ranges from less than 1 for a baked and glow discharge cleaned surface to over 10 for an unbaked surface. If the rate of desorption (proportional to $I^* \eta$) is higher than the rate of removal, the pressure will rise exponentially and leads to pressure instability. This could happen if h is large, the linear conductance of the chamber and the pumping speed are small or the pumps are spaced too far apart. For the RCS with large chamber conductance and one large ion pump every 4.7m (length of a halfcell), the critical $(I^* \eta)_{crit}$ will be over 50 A [17]. With average current of ~ 10 A and desorption coefficient of 5 or less for a thoroughly cleaned and insitu baked surface, no pressure bump instability is expected in RCS.

The initial energy of ionized electrons will be < 10 eV. With a bunch spacing of $0.4 \mu s$ in RCS, electrons will be pushed toward the wall by the magnet field. No accumulation of electrons is expected here. In the long straight sections, some electrons might be trapped and oscillating in the beam potential. Clearing electrodes, if necessary, will be positioned at a few strategic locations to remove any trapped electrons. Secondary electrons will be ejected from the chamber surface when bombarded by the ionized electrons. These electrons can be attracted by the next beam bunches and hit the wall again liberating more electrons (the multi-pactoring effect). With the exception of alumina, the secondary electron yields of standard vacuum chamber materials are < 2 if the energy of the electrons are less than 100 eV. By coating the wall of the alumina chambers with silver the secondary electron yield can

be reduced, thus avoiding multi-pactoring.

2.10.2 Vacuum chambers

The RCS ring will be divided into 8 vacuum sectors, four arc sectors and four straight sectors, which can be isolated with all metal gate valves. Each sector consists of eight half cells and is to be insitu baked to 120°C. One ion pump of 200 l/s, supplemented with a titanium sublimation pump, will be positioned at each halfcell (every 4.7 m). Coupled with the large chamber conductance, they will provide enough pumping to meet the beam stability requirement up to an $I^*\eta < 50$ A.

Each arc halfcell consists of four chambers, the dipole chamber, the quadrupole/sextupole chamber, and two bellowed chambers. The dipole chambers and the quadrupole/sextupole chambers will be made of high strength alumina ceramic, thus avoiding the eddy current effect (both thermal and magnetic) from the fast changing magnetic field. A thin wall chamber made of inconel will have eddy currents of hundreds amperes and thermal loads of several kilowatts per meter. The dipole chamber will be ~ 2.5 m long with a rectangular cross section of 18.8 cm (V) by 35.4 cm (H) and a bending curvature of 11.25°. The quadrupole, sextupole and corrector magnets will share a 1.3 m long, round ceramic chamber of either 25 cm or 33 cm in diameter for regular and large quads, respectively. Stainless steel chambers, each with welded bellows, are located between the ceramic chambers. The short (~ 0.2 m) one locates between the dipole and the corrector. The long (~ 0.65 m) chamber located between the dipole and the quadrupole houses the BPM and the ion pump port.

Two approaches have been developed to fabricate long ceramic chambers. The ISIS chambers were fabricated by jointing short straight sections of ceramic pipes together using glass glazing [18]. A different approach was developed at Triumf in the fabrication of the prototype chambers for Koan Factroy [19]. The alumina powder is isostatically pressed in a mold to form a pipe of appropriate cross section. The curvature of the dipole chamber is obtained by firing the pipe horizontally (with its sides on the top and bottom) and allowing the whole chamber to slump with gravity. The inner wall of the chambers was then coated with metal strips. These strips will be terminated at the end of chamber with resistor-capacitor networks, which present high impedance to the low frequency eddy current and low impedance to the high frequency image current. The strips are formed by coating the inner wall with silver based paste. The chambers are then fired to remove the organics in the paste and to provide adequate bonding of the strips to the alumina.

The Triumf approach will be adopted for RCS's ceramic chambers. It requires smaller magnet gaps, has better thermal contact of strips to the chamber and has few glass joints, which are potential sources of leaks. The walls of the ceramic chambers will be ~ 1 cm to prevent their slumping during firing. If necessary, the walls at the magnet poles may be machined down. The cost of machining is appreciable and has to be weighted against the added cost of a larger magnet gap. A space of 4 mm between chamber and magnet pole is allocated for heating jackets needed for insitu bake. The heating jackets will also damp any vibration, which is detrimental to ceramic chambers.

Round ceramic flanges with vitreous glass coating will be glazed to both ends of the ceramic chamber by a fused glass seal. A soft metal seal and quick disconnect V-type clamp will be

used to join this flange to the flange of the adjacent stainless steel chamber. Alternatively, metal flanges may be brazed to the ends of the ceramic chamber through a thin wall Kovar transition. The adjacent stainless chamber will have welded bellows to allow the ease of sealing and to avoid stressing the glazing joint.

Silver strips of 0.15 mm in thickness, corresponding to approximately 3 times of the skin depth, will be coated onto the inner wall of the chambers. One end of the strips will be connected to the stainless chamber using spring contacts held between the adjacent flanges. The other end of the strips will go around the end face of the ceramic chamber and be terminated with capacitors.

Extensive work is required to develop the fabrication technology of the ceramic chambers and the silver coating. The reliability of the sealing mechanism, the rf contacts and the capacitor terminations has to be thoroughly investigated. To ensure the stability of the beam, the ion desorption coefficients and the secondary electron yields of alumina and the silver strips also have to be studied.

Table 20: Synchrotron vacuum chamber requirements for two rings.

Quantity	Value	unit
Material	ceramic	
Pipe-to-magnet-pole clearance	4	mm
Dipole:		
Number of main dipole ceramic chambers	64	
Outer height	190	mm
Inner height	168	mm
Top-bottom wall thickness	1.1	mm
Outer width	354	mm
Inner width	314	mm
Side-wall thickness	20	mm
Quadrupole:		
Number of regular quadrupole ceramic chambers	72	
Regular & long ring quadrupole:		
Outer diameter	248	mm
Inner diameter	236	mm
Wall thickness at pole location	6	mm
Large ring quadrupole:		
Number of large quadrupole ceramic chambers	24	
Outer diameter at pole tip location	328	mm
Inner diameter	316	mm
Wall thickness at pole location	6	mm

2.11 Extraction

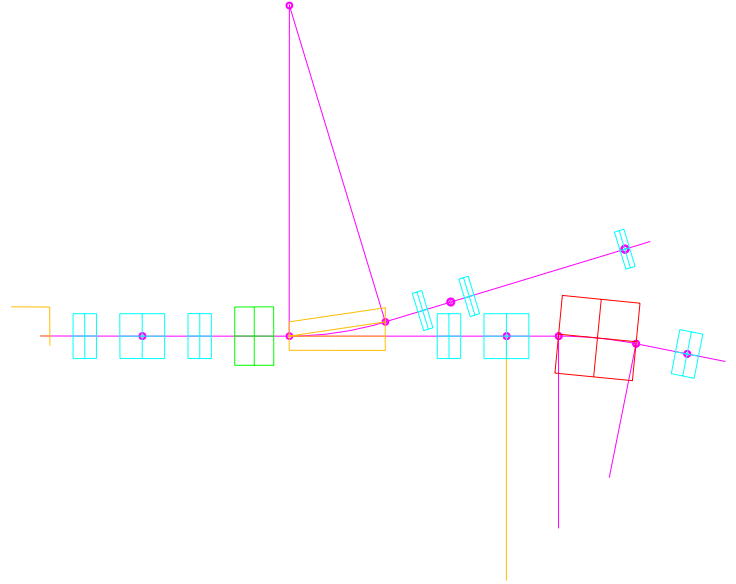


Figure 30: Extraction layout.

At the end of the acceleration cycle the two beam bunches will be ~ 150 nsec long and will be separated by 550 nsec. Both bunches have to be extracted in a single turn by fast kicker magnets which will kick the beam into a lambertson septum magnet. The frequency of the extraction process is set to 30 Hz. In this section we describe the layout and the optics of the extraction as well as the specifications of the required magnets for the extraction.

Extraction will take place in one of the straight sections of the RCS ring, using the following devices.

- Eight fast kickers magnet which will be placed at the end of the third long drift space (see Fig. 2.11) of the straight section.
- A lambertson septum magnet which will be placed at the last long drift section (see Fig. 2.11).

There are two constraints that should be satisfied in the extraction process:

- The Y_{cod} at the location of the triplets upstream of the septum, must be less then the 8.1 cm for the extracted beam to clear the beam pipe at the location of the triplet. This constrain is based on the available apperture of the quadrupoles, the acceptance of the RCS ring and the beam parameters at the location of the triplet.

- The vertical displacement of the central orbit Y_{cod} at the entrance of the lambertson septum should be 9.1 cm.

The extraction process begins with the simultaneous excitation of all eight kicker modules which will be excited to the required field in ~ 330 nsec and will remain at a constant field for ~ 600 nsec. During this time each bunch entering the kickers will be kicked vertically into the aperture of the lambertson septum magnet, and subsequently will be deflected horizontally by 15.5 deg by the lambertson magnet in order to clear the quadrupole downstream of the lambertson and subsequently enter into the RTBT transport line. The bottom part of Fig. 2.11 shows the Y_{cod} (vertical displacement of the central orbit) after it is kicked vertically by the kickers.

In case that any of the kicker module does not fire due to malfunction, the beam bunch will not be deflected at its nominal vertical location. Fig. 2.11 shows the location in vertical phase space (y, y') of a fully, deflected bunch with all eight kicker modules fired, and the location of a partially deflected bunch when one of the kicker modules does not fire. We assuming a beam emittance of $260 \pi \text{mm} \cdot \text{mrad}$ and an acceptance of the RTBT line to be $600 \pi \text{mm} \cdot \text{mrad}$.

The requirements for the ring extraction system are summarized in Table 2.11

Table 21: Extraction parameters.

Extraction type	Single turn Two step
First step	Fast vertical full aperture kicker
Second Step	Magnetic septum Lambertson type
Maximum extraction rate	30 Hz
Fast kicker vertical deflection angle	18.0 mrad
Vertical displacement at septum entrance	9.1 cm
Kicker rise time	< 330 nsec 0 to 97%
Kicker constant field duration	~ 600 nsec
Lambertson deflection angle	15.5 degrees, horizontal
Beam extracts to target when one kicker module misfires	Yes

2.11.1 Kicker specifications

The fast kicker system consists of eight identical window-frame magnets with ferrite core. Each magnet will be excited by a single-turn copper conductor that will be centered-fed through the return leg of the ferrite core. The fast kicker pulsers will consist of eight pulse-forming networks (PFN) that will be discharged simultaneously into the single-turn copper coils of the magnets. The discharge will be by hydrogen thyratron tubes that are capable of high currents and fast rise times. In order to reduce the total inductance between the thyratron and the kicker, each of the eight PFN will be located in the ring next to closely coupled to each magnet section.

A summary of the specification of the kicker is given in Table 2.11.1.

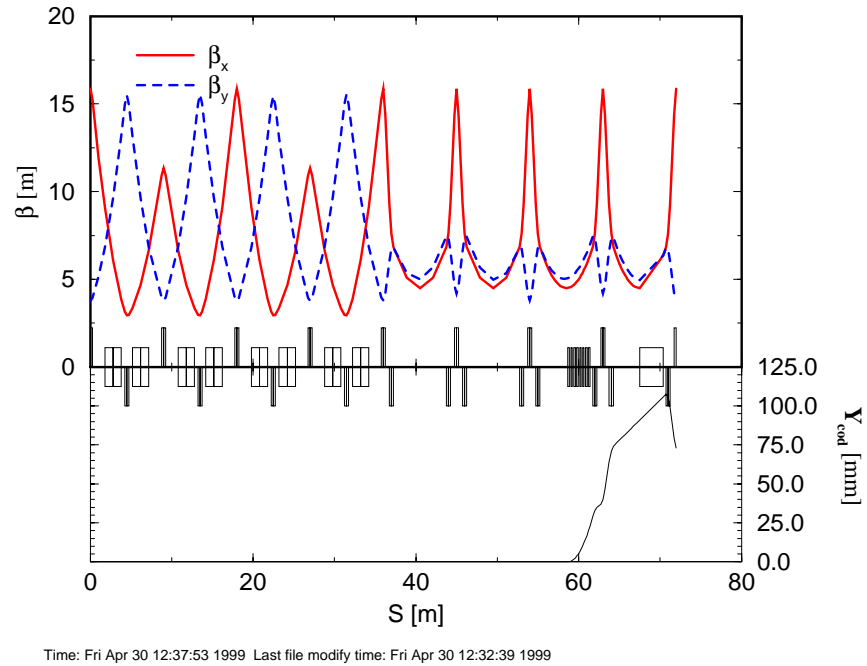


Figure 31: Extraction lattice.

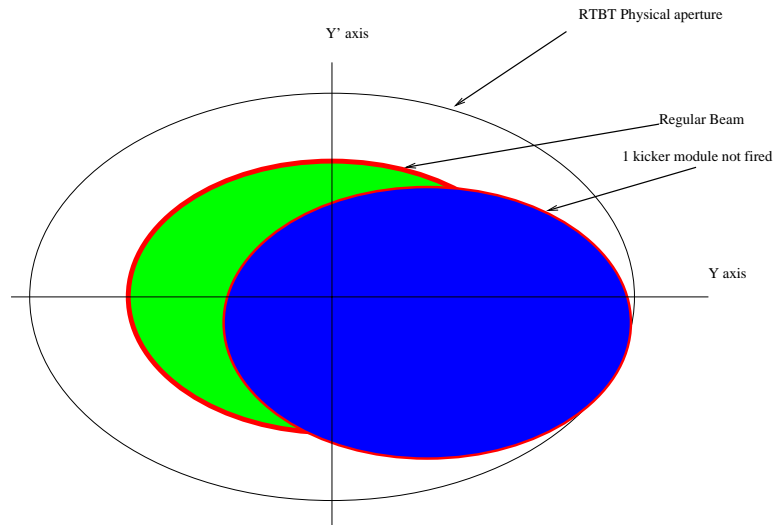


Figure 32: Extraction configuration.

Table 22: Fast extraction kicker parameters.

Mechanical Parameters:	
Type	Window-frame
Core material	Ferrite
No. of modules	8
Core length	44 cm
Core spacing	10 cm
Total length	380 cm
Gap (horizontal)	13.5 cm
Width (vertical)	13.5 cm
Electrical Parameters:	
Deflection angle per kicker module	2.25 mrad
Peak field	475 Gauss
Maximum current	5100 A
Pulse rate	30 Hz
Rise time	330 nsec
Pulse flat-top	600 nsec
Voltage per kicker	22 kV
No. of pulse-forming networks	8
No. of DC power supply	1
Voltage rating	40 kV

Both the maximum Voltage and Current requirements can be reduced by a factor of 0.88 or 0.84 by either, introducing an additional kicker or creating a slow bump at the entrance of the septum magnet.

2.11.2 Lambertson magnetic septum

A Lambertson type magnetic septum will be used to eject the fast kicked beam from the RCS ring. The septum will deflect the beam by 15.5 degrees with a field of ~ 0.82 Tesla. Computer simulations will optimize the magnetic field uniformity in the main field region and the minimization of the magnetic field in the circulating beam region. The magnet will be curved in the direction of the deflected beam and will have a Y-shaped vacuum chamber in order to accomodate the circulating and extracted beams. The magnet will operate in a DC mode and will be powered by an AC to DC converter type using multiphase ACR's (silicon controlled rectifier).

Table 23: Lambertson septum magnet parameters.

Bend angle	15.5 degree
Gap (field-free region)	5.2 cm radius
Gap (main-field region)	8 cm (V) \times 10 cm (H)
Septum thicness	1 cm
B (main-field)	8.2 kG
No. of turns	1350 A
Magnet resistance	0.009
Maximum DC voltage	15 V
Maximum power	20 kW

2.11.3 Timing and synchronization

In normal operating conditions the fast kicker must be triggered so that its field rises to its full value in the time intrval between the tail of one bunch and the head of the second bunch. Just after the extraction of the two bunches from the ring the charging of the fast kicker modules will begin and take ~ 12 msec ending ~ 1 msec before the start of the new magnet cycle. When the required charging level has been verified by the Beam Permit System, injection of the next two beam pulses from the LINAC will begin. Since no beam can be dumped continuously in the ring, the Beam Inhibit System will prevent any additional beam pulses from being admitted into the main ring after an abnormal condition is sensed in the SNS accelerator complex including the target area.

Table 24: RCS extraction parameters.

Quantity	Value	unit
Extraction energy, E_k	2	GeV
β	0.9477	
γ	3.1322	
$\beta\gamma$	2.968	
Momentum, p_0	2.784	GeV/c
Revolution frequency	0.950	MHz
Revolution period	1.053	μ s
Emittance	89	π mm mr
RF voltage, $h = 2$	225	kV
RF synchronous phase, ϕ_s	0	
RF frequency, $h = 2$	1.90	MHz
RF frequency, $h = 4$	3.80	MHz
RF bucket area	34.0	eVs
Bunch area	3.8	eVs
Synchrotron frequency	1.3	kHz
Synchrotron period	740	turn
Number of bunches	2	
Bunching factor	0.21	
Bunch center distance	527	ns
Bunch length	140	ns
Beam gap width	387	ns
Magnetic rigidity, $B\rho$	9.29	Tm
Dipole field	0.91	T
Quadrupole gradient, B'	4.6, 3.8, 5.9	T/m
Sextupole gradient, B''	83, 65	T/m ²

2.12 Impedance

The SNS RCS consists of two rings, with each ring carrying 1.04×10^{14} proton per cycle, injected at 400 MeV , and extracted at 2 GeV . With the repetition rate of 30 Hz , the extracted beam power per ring is 1 MW . The ring has a circumference of 299.2 meters , largely using the ceramic vacuum chamber with printed wires as the RF shield.

The ring impedance consists of the resistive wall, space charge, broadband, low frequency, and narrow band types. For each one of the impedance, the injection and extraction conditions are considered. The maximum value of the impedance is also provided, if needed.

Most part of this study follows the previous work on the SNS storage ring impedance [21].

2.12.1 Resistive Wall Impedance

For the ceramic vacuum chamber with the printed RF shielding wires, the longitudinal and transverse resistive wall impedances are,

$$Z_\ell(\omega) = (\text{sgn}(\omega) + j) \frac{\beta Z_0 \delta_s}{2b} \frac{\omega}{\omega_0} \quad (1)$$

and

$$Z_T(\omega) = (\text{sgn}(\omega) + j) \frac{R Z_0 \delta_s}{b^3} \quad (2)$$

where Z_0 is the impedance in free space, 377Ω , b is the radius of the vacuum chamber and R is the machine radius. The skin depth at the frequency ω is defined as,

$$\delta_s = \sqrt{\frac{2\rho}{\mu_0 |\omega|}} \quad (3)$$

where $\mu_0 = 4\pi \times 10^{-7} \text{ H/m}$ is the permeability of free space, and ρ is the resistivity of the vacuum chamber, for silver deposition it is $\rho = 0.03 \times 10^{-6} \Omega m$.

For the SNS RCS, $R = 47.6 \text{ m}$, and the average beam pipe radius is taken as $b = 10 \text{ cm}$. At the revolution frequency 0.714 MHz to 0.950 MHz , we get $\delta_s = 0.10 \text{ mm}$ to 0.09 mm . Taking the spacing factor of 2, the longitudinal and transverse resistive wall impedances at the revolution frequency are

$$Z_\ell(\omega_0) = 0.27(1 + j)\Omega \text{ to } 0.32(1 + j)\Omega \quad (4)$$

and

$$Z_T(\omega_0) = 3.6(1 + j)K\Omega/m \text{ to } 3.2(1 + j)K\Omega/m \quad (5)$$

respectively.

Since the fractional tune is 0.82, the most damaging resistive wall impedance is $Z_T(-0.18\omega_0) = (-1 + j) 8.6 K\Omega/m$ to $(-1 + j) 7.5 K\Omega/m$. Note that assuming the tune unchanged, we have $\delta_s = 0.24 \text{ mm}$ to 0.21 mm at this frequency. On the other hand, the printed wires have the thickness of 0.25 mm .

2.12.2 Space Charge Impedance

The longitudinal space charge impedance is defined as,

$$Z_\ell(\omega) = -j \frac{g Z_0}{2\beta\gamma^2} \frac{\omega}{\omega_0} \quad (6)$$

where

$$g = 1 + 2 \ln \frac{b}{a} \quad (7)$$

For Gaussian distribution, $a = \sqrt{2}\sigma$, where σ is the transverse rms beam size.

The transverse space charge impedance is,

$$Z_T(\omega) = -j \frac{R Z_0}{\beta^2 \gamma^2} \left(\frac{1}{a^2} - \frac{1}{b^2} \right) \quad (8)$$

We have $\beta = 0.713$ to 0.948 , $\gamma = 1.426$ to 3.132 , taking $a = \sqrt{2}\sigma = 2.49$ cm to 1.46 cm, then the longitudinal and transverse space charge impedances are

$$Z_\ell(\omega_0) = -j492 \Omega \text{ to } -j98.3 \Omega \quad (9)$$

and

$$Z_T(\omega) = -j26.3 \text{ M}\Omega/\text{m} \text{ to } -j9.3 \text{ M}\Omega/\text{m} \quad (10)$$

respectively.

The longitudinal impedance can be written as Z_ℓ/n , with $n = \omega/\omega_0$. Thus, we have $Z_\ell/n = Z_\ell(\omega_0)$.

Both Z_ℓ/n and Z_T are independent of the frequency and appear to be negative inductive.

2.12.3 Broad Band Impedance

The broad band impedance is caused by the bellows, steps, vacuum ports and valves. The impedance of the collimator can be seen as the combination of a resistive wall with smaller pipe radius, and the steps as well, but it is dominated by the steps. The models of these components will be presented, and the longitudinal impedance will be estimated. The transverse impedance will be obtained by using

$$Z_T \approx \frac{2R}{\beta b^2} \left(\frac{Z_\ell}{n} \right) \quad (11)$$

Since the real part of these impedance rises only above the pipe cut-off frequency, therefore, it is negligible. Only the imaginary part of the impedance will be presented.

Model The impedance of bellows and steps can be estimated using a model of pillbox. In all cases, we assume the worst case without tapering at the transitions.

The impedance for short pillbox ($w \leq h$) is calculated using,

$$Z_\ell = j\omega \frac{Z_0}{2\pi b c} \left(wh - \frac{w^2}{2\pi} \right) \quad (12)$$

which is inductive.

For a deep pillbox, $h \sim b$, the impedance is,

$$Z_\ell = j\omega \frac{Z_0}{2\pi bc} \left(wb \ln\left(1 + \frac{h}{b}\right) - \frac{w^2}{2\pi} \right) \quad (13)$$

If $w \gg h$, we have

$$Z_\ell = j\omega \frac{Z_0 h^2}{2\pi^2 bc} \left(2 \ln \frac{2\pi w}{h} + 1 \right) \quad (14)$$

where $w < b$ is still required.

Increase further the length w beyond b , the situation becomes two separate steps. The transition is at $w = b$. Simply substitute w by b , and divide by 2 in the equation (14), we have

$$Z_\ell = j\omega \frac{Z_0 h^2}{4\pi^2 bc} \left(2 \ln \frac{2\pi b}{h} + 1 \right) \quad (15)$$

The longitudinal impedance associated with a round vacuum pumping hole of radius b_{port} can be estimated as,

$$\frac{Z_\ell}{n} = j \frac{Z_0}{6\pi^2} \frac{b_{port}^3}{Rb^2} \quad (16)$$

Impedance of bellows For the SNS, there are 40 bellows at $b = 10$ cm, each has 20 corrugations with the period of 0.75 cm, i.e. $w = 3.75$ mm, and the depth $h = 1.5$ cm. Also, there are 32 bellows at $b = 15$ cm, each has 10 corrugations with the period of 1.5 cm, i.e. $w = 7.5$ mm, and the depth $h = 2$ cm. Using the equation (12), we have

$$\frac{Z_\ell}{n} = j0.79\Omega \text{ to } j1.05\Omega \quad (17)$$

and

$$Z_T = j10.5 \text{ K}\Omega/m \text{ to } j10.5 \text{ K}\Omega/m \quad (18)$$

Impedance of steps The impedance of steps can be estimated by using the equation (15). Note that the difference between a step-up and a step-down is disregarded.

The normal vacuum chamber radius is $b = 10$ cm. However, there are total 12 large quads with $b = 14$ cm, which result in 24 steps from 10 cm to 14 cm. For the 40 BPM's associated with normal quads, there are 80 steps from 10 cm to 12 cm, and for 8 BPM's with large quads, there are 16 steps from 14 cm to 16 cm. The present design shows that half of BPM tanks' steps are with taper.

The average vertical radius for all dipoles is taken as 9 cm. Therefore, for 32 dipoles, there are 64 steps from 9 cm to 10 cm.

Consider the horizontal steps. For 24 steps, with $b = 10$ cm, $h = 14$ cm, we have $Z_\ell/n = j2.7\Omega$. For 80 steps, with $b = 10$ cm, $h = 12$ cm, we get $Z_\ell/n = j7.1\Omega$, and for 16 steps, with $b = 15$ cm, $h = 17$ cm, we have $Z_\ell/n = j1.9\Omega$. In total, we have, $Z_\ell/n = j11.7\Omega$.

There are additional 64 vertical steps, with $b = 9$ cm, $h = 10$ cm, which result in $Z_\ell/n = j4.5\Omega$.

Let us take the shielding effect of the striplines at a BMP tank as a factor of 2 reduction in impedance. Also we assume that half of the transitions at dipoles are with taper, resulted in the impedance reduction by a factor of 2. The total vertical step impedance is,

$$\frac{Z_\ell}{n} = j8.1\Omega \text{ to } j10.7\Omega \quad (19)$$

and

$$Z_T = j108.1 \Omega/m \text{ to } j107.4 K\Omega/m \quad (20)$$

The horizontal impedance is a little smaller than the vertical one, but both are much larger than the impedance caused by the bellows.

Impedance of ports The storage ring has total 64 round vacuum pumping holes, with 6" diameter. We take $b_{port} = 7.5 \text{ cm}$. Let the beam pipe radius be $b = 10 \text{ cm}$, we get the total longitudinal impedance, using (16),

$$\frac{Z_\ell}{n} = j0.36 \Omega \text{ to } j0.36 \Omega \quad (21)$$

and the transverse impedance

$$Z_T = j4.8 K\Omega/m \text{ to } j3.6 K\Omega/m \quad (22)$$

Impedance of valves There are 8 vacuum valves at $b = 10 \text{ cm}$, and we may also have 8 valves at $b = 12.5 \text{ cm}$. Let a valve be roughly described by a pillbox with $w = 5 \text{ cm}$, and $h = 4 \text{ cm}$. Using the equation (13), we get the total longitudinal impedance

$$\frac{Z_\ell}{n} = j0.17 \Omega \text{ to } j0.23 \Omega \quad (23)$$

and the transverse impedance

$$Z_T = j2.3 K\Omega/m \text{ to } j2.3 K\Omega/m \quad (24)$$

Collimator A simplified model of collimator consists of a resistive wall with smaller pipe radius and the steps as well. There are 4 collimator units, each has an overall radius $b_{colli} = 7.5 \text{ cm}$, and a length of $\ell_{colli} = 2.43 \text{ m}$. Assume the collimators to be made by stainless steel, the same as the vacuum chamber. The collimator resistive wall impedance at ω_0 is,

$$Z_{\ell,wall}(\omega_0) = \frac{4\ell_{colli}}{2\pi R} \frac{b}{b_{colli}} Z_\ell(\omega_0) = 0.04(1+j) \Omega \quad (25)$$

and

$$Z_{T,wall}(\omega_0) = \frac{4\ell_{colli}}{2\pi R} \frac{b^3}{b_{colli}^3} Z_T(\omega_0) = 0.52(1+j) K\Omega/m \quad (26)$$

The longitudinal and transverse resistive wall impedances are 6% and 10% of the ring impedances, respectively.

For both horizontal and vertical transition impedances, we calculate 8 steps, with $b = 7.5$ cm, $h = 10$ cm, i.e.,

$$\frac{Z_\ell}{n} = j0.62 \, \Omega \text{ to } j0.83 \, \Omega \quad (27)$$

and

$$Z_T = j8.3 \, K\Omega/m \text{ to } j8.3 \, K\Omega/m \quad (28)$$

Note that these are much larger than the resistive wall part of impedance.

Summary The total longitudinal broad band impedance is estimated as

$$\frac{Z_\ell}{n} = j11 \, \Omega \text{ to } j14.7 \, \Omega \quad (29)$$

and

$$Z_T = j147 \, K\Omega/m \text{ to } j147 \, K\Omega/m \quad (30)$$

2.12.4 Low Frequency Impedance

Beam position monitor Dual plane stripline BPM's will be located adjacent to each quadrupole. One end of the stripline is shorted and another end is terminated for detection.

The longitudinal impedance of one strip plate, for such kind of BPM, is,

$$Z_\ell = Z_c \left(\frac{\phi_0}{2\pi} \right)^2 \left(\sin^2 \frac{\omega\ell}{c} + j \sin \frac{\omega\ell}{c} \cos \frac{\omega\ell}{c} \right) \quad (31)$$

where ℓ and ϕ_0 are the BPM length and subtends, and Z_c is the characteristic impedance of the stripline. One may notice that the lowest resonant frequency of the impedance is at $f_R = c/(4\ell)$. The reactive part, for frequency much smaller than f_R , can be estimated as,

$$\frac{Z_\ell}{n} = j \frac{Z_c}{n} \left(\frac{\phi_0}{2\pi} \right)^2 \sin \frac{\omega\ell}{c} \cos \frac{\omega\ell}{c} \approx j Z_c \left(\frac{\phi_0}{2\pi} \right)^2 \frac{\beta\ell}{R} \quad (32)$$

The transverse impedance can be obtained using the Nassibian-Sacherer derivation from the longitudinal impedance of the displaced beam. For a pair of striplines, it is in the perpendicular direction,

$$Z_T = \frac{R}{\beta b^2} \left(\frac{4}{\phi_0} \right)^2 \sin^2 \frac{\phi_0}{2} \left(\frac{Z_\ell}{n} \right) \quad (33)$$

where Z_ℓ is the longitudinal impedance for two striplines. In another direction, it is $Z_T = 0$.

Let ϕ_0 be small, the transverse impedance can be estimated as,

$$Z_T \approx \frac{4R}{\beta b^2} \left(\frac{Z_\ell}{n} \right) \quad (34)$$

In the SNS RCS, total 36 BPM's are associated with normal quads, where $b = 10$ cm. Total 12 BPM are associated with large quads, where $b = 14$ cm. All striplines have the

length $\ell = 12.5 \text{ cm}$, and the subtends $\phi_0 = 70 \text{ deg}$. The characteristic impedance of the stripline is $Z_c = 50 \Omega$.

At the low frequency, $\omega \ll c/\ell$, for 48 pairs of plates, we have,

$$\frac{Z_\ell}{n} \approx j0.68 \Omega \text{ to } j0.91 \Omega \quad (35)$$

and,

$$Z_T \approx j14.7 \text{ k}\Omega/m \text{ to } j14.7 \text{ k}\Omega/m \quad (36)$$

These are also the maximum imaginary part of the impedance. On the other hand, the maximum real parts of the impedance are at 450 MHz , with

$$\frac{Z_\ell}{n \text{ Re,max}} = 0.49 \Omega \text{ to } 0.65 \Omega \quad (37)$$

and

$$Z_{T,\text{Re,max}} = 10.2 \text{ K}\Omega/m \text{ to } 10.2 \text{ K}\Omega/m \quad (38)$$

Extraction kickers In a window frame magnet, the transverse impedance is dominated by the differential flux in the core induced by the beam position deviation. Differential flux generated by the beam is the same as two parallel wires, one represents the beam, and another returned at the position center, terminated at both ends. Neglecting the chamber effect, the conductor shielding effect, the ferrite boundary effects, etc. this yields the transverse impedance,

$$Z_T = \frac{c\omega\mu_0^2\ell^2}{4a^2Z_k} \Omega/m \quad (39)$$

where ℓ is the magnet length, $2a$ is the inner height, and $Z_k = j\omega L + Z_g$, with L the magnet inductance, and Z_g the termination impedance.

The SNS RCS extraction kicker has 8 window frame magnet units, the average length is $\ell = 40 \text{ cm}$, and the average inner width is $2b = 14 \text{ cm}$, all have the same height $2a = 11.5 \text{ cm}$. The magnet inductance of each unit is $L = \mu_0 b\ell/a = 0.61 \mu H$. The stray inductance is about $L_{\text{stray}} = 0.5 \mu H$.

With the charge resistance of 200Ω , and disregarding the stray parameters, we have the maximum real part of the impedance, which happens at 30 MHz ,

$$Z_{T,\text{Re,max}} = 20.7 \text{ K}\Omega/m \text{ to } 20.7 \text{ K}\Omega/m \quad (40)$$

and the imaginary part,

$$Z_{T,\text{Im,max}} = -j40 \text{ K}\Omega/m \text{ to } -j40 \text{ K}\Omega/m \quad (41)$$

These are not changed if the magnet is terminated by a 50Ω resistance, however, the peak real impedance will be at 7 MHz , rather than 30 MHz .

For longitudinal impedance, we consider the beam passes a ferrite ring with the outer and inner radii b_2 and b_1 . The inductance of the ferrite ring is

$$L = \frac{\mu_r\mu_0\ell}{2\pi} \ln \frac{b_2}{b_1} \quad (42)$$

where μ_r is the relative permeability. For CMD5005 used in the extraction kicker, $\mu_r \approx 1000$. Taking the equivalent $b_2 = 8.8 \text{ cm}$, and $b_1 = 6.3 \text{ cm}$ for the extraction kicker magnet, we get $L = 26.7 \text{ } \mu\text{H}$ for each module.

To reduce the massive ferrite loss, copper sheets are placed in the ferrite core as flux break.

Let the thickness of the copper sheet be δ_{copper} , then the corresponding leakage is estimated as,

$$L_{leak} = 2 \frac{\mu_0 \ell}{2\pi} \ln \frac{\pi a}{2\delta_{copper}} \quad (43)$$

Taking $\delta_{copper} = 1 \text{ mm}$, $2a = 11.5 \text{ cm}$, we get $L_{leak} = 0.72 \text{ } \mu\text{H}$ for $\ell = 40 \text{ cm}$, i.e. one magnet module. This is 2.7% of the flux generated without the copper sheet. If we take a 1% flux leakage around the copper sheet, the total inductance of 8 modules presented to the beam is $L_m = 2.14 \text{ } \mu\text{H}$. Using

$$\frac{Z_\ell}{n} = j\omega_0 L_m \quad (44)$$

we get the equivalent longitudinal impedance,

$$Z_\ell/n = j19.2\Omega \text{ to } j25.5\Omega$$

2.12.5 Narrow band impedance

For the fundamental mode of the RF cavities, the impedance can be expressed as

$$Z = \frac{R_{sh}}{1 + jQ(\omega/\omega_R - \omega_R/\omega)} \quad (45)$$

where R_{sh} and Q are the shunt resistance and quality factor of the loaded cavity, respectively, and ω_R is the resonant frequency.

There are 6 RF stations in the ring, each station consists of 2 gaps, at 25 KV per gap. The second harmonic consists of 2 station, with 2 gaps at 25 KV per gap. The same ferrite of the AGS Booster band III cavities, Phillips 4M2, will be used. The design of $h = 2$ and $h = 4$ cavities is the same.

The relative permeability is $\mu_r = 130$ for Phillips 4M2. Taking the ferrite length $\ell = 1.5 \text{ m}$, the inner radius $r_{in} = 17.5 \text{ cm}$, and the outer radius $r_{out} = 25 \text{ cm}$, the total inductance of a gap is

$$L = \frac{\mu_r \mu_0 \ell}{2\pi} \ln \frac{r_{out}}{r_{in}} = 14 \text{ } \mu\text{H} \quad (46)$$

The inherent capacitance is

$$C_{inh} = \frac{2\pi \epsilon_0 \ell}{\ln(r_{out}/r_{in})} \quad (47)$$

where $\epsilon_0 = 1/(\mu_0 c^2) = 8.8542 \times 10^{-12} \text{ F/m}$. We get $C_{inh} = 234 \text{ pF}$.

The capacitance needed to get $\omega_R = 2\pi \times 1.43 \text{ MHz}$ is $C_1 = 885 \text{ pF}$ for $h = 2$ cavities, and $C_2 = 221 \text{ pF}$ for $h = 4$ cavities. The inherent capacitance is small compared with the added ones.

The ferrite resistance is $R_{ferr} = 10 \text{ } K\Omega$ per gap, and the generator resistance is $R_{gen} = 1 \text{ } K\Omega$. Therefore, we have the shunt resistance of a gap,

$$R_{sh} \approx R_{gen} = 1 \text{ } K\Omega \quad (48)$$

The loaded cavity quality factor is

$$Q_1 = R_{sh} \sqrt{\frac{C_1}{L}} = 8.0 \quad (49)$$

For $h = 4$ cavity, it is $Q_2 = 4.0$.

The first estimate of high order modes is from the calculation of unloaded cavity study [22]. For the loaded cavity, the equivalent output impedance of the power amplifier of $R_{gen} = 1 \text{ } K\Omega$ is considered, which yields the follows, including the fundamental mode,

Frequency	R/Q
1.43	50
4.43	7.7
7.72	2.5
11.15	1
14.59	0.7
<i>MHz</i>	

The longitudinal high order modes and the transverse modes will be estimated using simulation codes. Once a prototype of cavities becomes available, measurement will be performed.

The possible narrow band impedance caused by large steps and cavities in the vacuum chamber will also be studied by the simulations.

2.12.6 Impedance budget

2.13 Collective instabilities

Because of the relatively large beam momentum spread, the longitudinal microwave instability will not be a problem. On the other hand, the transverse instability is usually of more concern. Firstly, the transverse instability directly causes beam loss, and secondly, there is large uncertainties in the transverse impedances, for instance, that from the extraction kickers. In general, the low energy synchrotrons operated below transition have not seen serious transverse instabilities. This is because of the large Landau damping effect come from the space charge incoherent tune spread. The SNSRCS is not exceptional. The resistive wall, head-tail, transverse Robinson type, and the transverse microwave instabilities will be studied. Finally, the condition of possible e-p instability will be compared with other machines.

2.13.1 Longitudinal microwave instability

Among the possible longitudinal beam instabilities, only the microwave instability needs to be addressed. The Keil-Schnell criterion is sufficient in this study, where the most important beam stabilizing factor, the beam momentum spread, is calculated using the beam peak current, i.e.,

$$\frac{dp}{p} > \sqrt{\frac{eI_p}{F\gamma E_0|\eta|} \left| \frac{Z_\ell}{n} \right|} \quad (50)$$

The form factor F is usually taken as 1. The longitudinal impedance is dominated by the space charge, which is $-j492 \Omega$ at the injection, and $-j98.3 \Omega$ at the extraction. The broad band impedance is inductive, so it offsets the space charge impedance. The total conventional longitudinal broad band impedance is estimated as $j14.7 \Omega$ at the extraction. The extraction kicker longitudinal impedance may contribute to this type of impedance, which is $j25.5 \Omega$ at the extraction, given 1% flux leakage through the copper sheets.

The beam peak current at the extraction is the highest, and the slippage can go much smaller, from -0.46 at the injection to -0.07 at the extraction. The peak current effect is cancelled somewhat by the increase of γ , but slippage effect makes the stability condition the worst at the extraction.

In Fig. 2.13.1, the RF voltage program, the beam peak current, the bunching factor, and the beam momentum spread are shown. The K-S criterion required beam momentum spread is calculated using the conventional broad band impedance.

In general, the longitudinal microwave instability is manageable.

2.13.2 Transverse instabilities

For the transverse instability, we need to go for a more detailed look. For instance, the transverse instability with the mode $m = 0$ is estimated by

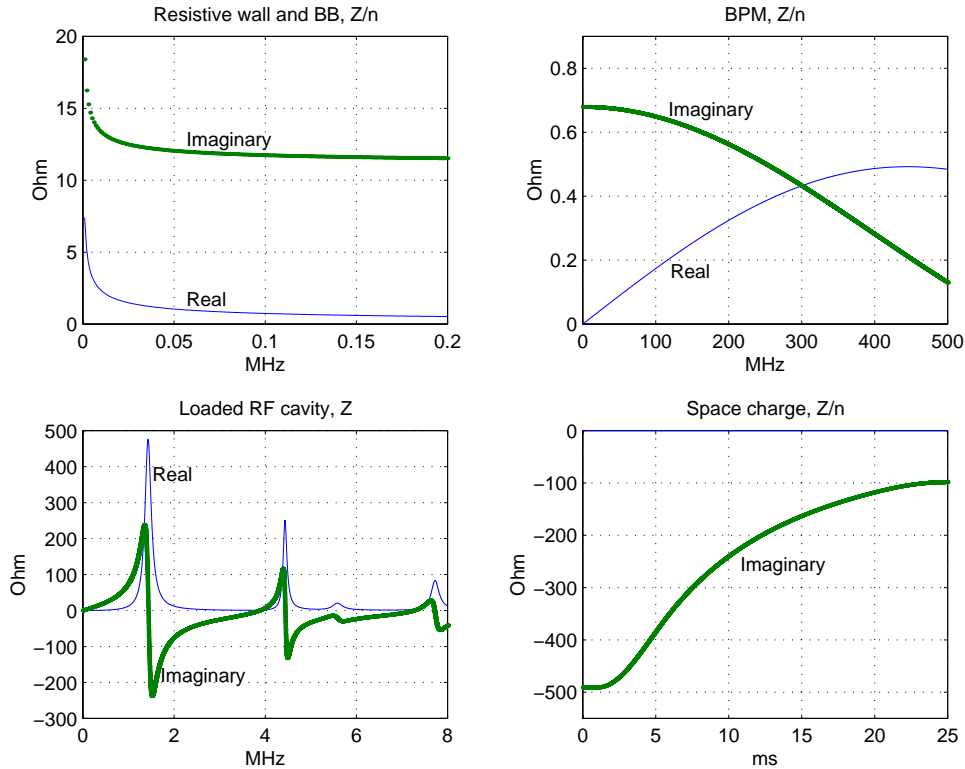
$$\Delta\omega = \omega - \omega_\beta = \frac{j\beta eI_0}{2Rm_0\gamma\omega_\beta} \sum_{n=-\infty}^{\infty} Z_T(n)\Lambda_0^2(n') \quad (51)$$

where $\Lambda_0^2(n')$ is the power spectrum of the beam signal with mode $m = 0$. n' represents the chromatic effect, and $Z_T(n)$ is the transverse impedance.

Table 25: Impedance budget for each synchrotron.

Impedance	Longitudinal	Transverse
	Z_L/n [Ω]	Z_T [$k\Omega/m$]
Space charge	$-j$ 196	$-j$ 6870
Broad band		
bellows	j 1	j 8
steps	j 15	j 120
ports	j 0.5	j 3.9
collimators	j 1	j 8
	$Z_L(\omega_0)$ [Ω]	$Z_T(\omega_0)$ [$k\Omega/m$]
Resistive wall	$0.7 (1 + j)$	$5 (1 + j)$
Low frequency		
BPM	$0.06 + 4.5j$	$0.4 + 29j$
	Z_L/n [Ω]	$\max(Z_T)$ [$k\Omega/m$]
Ext. kicker	j 30	$20 - j40$
RF cavity		

R

Figure 33: RCS longitudinal impedances z/n for resistive wall and broad band, BPM, and space charge. The loaded RF cavity impedance is for one station.

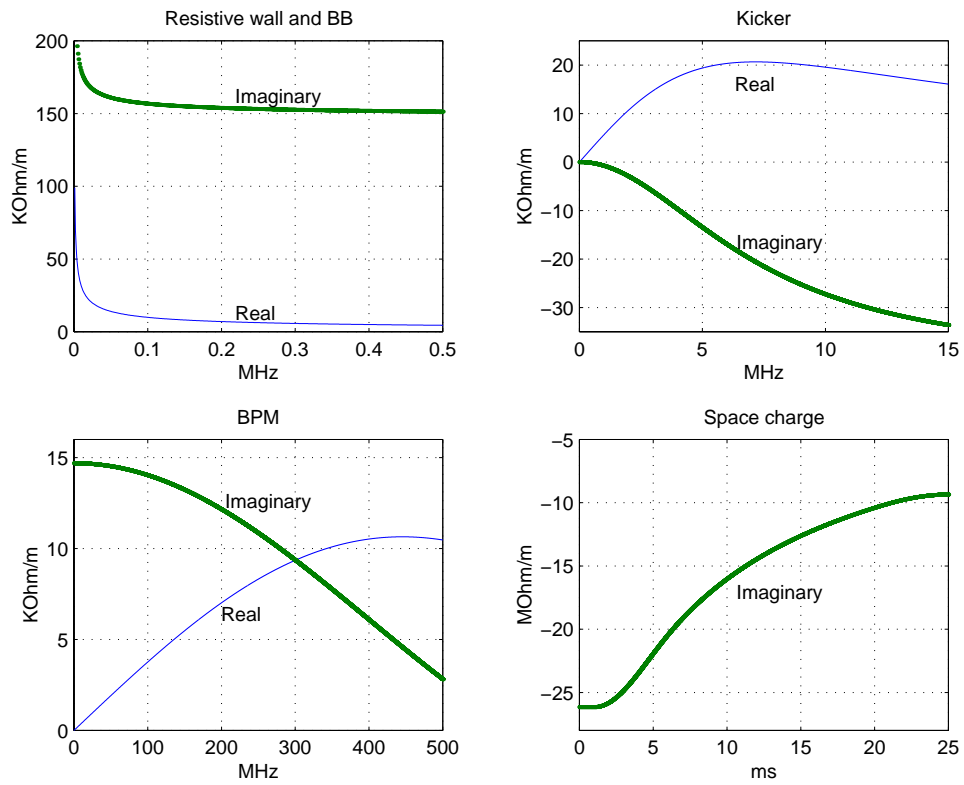


Figure 34: RCS transverse impedances for resistive wall and broad band, extraction kicker, BPM, and space charge.

Three factors are involved in the calculation.

1. The transverse impedance $Z_T(n)$, which is given in [1], and the beam spectrum, which will be discussed in next subsection.
2. The chromatic effect, which can be represented by the shifting of the beam spectrum in the frequency direction.
3. The sampling at the harmonic n .

Once the frequency shift $\Delta\omega$ is obtained, it is substituted into $e^{j\Delta\omega t}$. The imaginary $Z_T(n)$ gives rise to real $\Delta\omega$, which in turn gives rise to frequency shift. On the other hand, the real $Z_T(n)$ gives rise to imaginary $\Delta\omega$, which in turn gives rise to growth or damping rates.

Beam spectrum The beam spectrum of the mode $m = 0$ and $m = 1$ will be used in this study. Probably only the bandwidth of the spectrum of $m = 0$ mode needs to be mentioned. The full bandwidth of the power spectrum is

$$W_{bh} = \frac{2}{\tau} \quad (52)$$

where τ is the total bunch length, and W_{bh} in Hz . For SNS RCS, the bunch length is 420 ns at the injection and 140 ns at the extraction, with the single harmonic RF, therefore, we have $W_{bh} = 4.76 MHz$ to $14.3 MHz$. The relevant spectral lines are 3 and 10 at injection and extraction, respectively. With the double RF, the situation is a little complicated. In this study, the double RF parameters will be used. The complication of the non-regular bunch shapes, however, is disregarded.

Resistive wall instability The resistive wall instability is calculated assuming zero chromaticity. The horizontal tune at $\nu = 7.82$ can give rise to an instability. The vertical at the tune $\nu = 7.3$ should not cause problem. Note that for the RF harmonic $h = 2$, only the coupled bunch mode $n = 1$ is relevant in the resistive wall instability.

The wall impedance at the relevant frequency, $-18f_0 = 128.5 KHz$ is $8.6 K\Omega/m$ at the injection, and $7.5 K\Omega/m$ at the extraction. This is assuming that the thick silver wires with the spacing factor of 2 is used as the RF shield. Should the steel wires be used, this impedance would be increased dramatically.

Using only one sampling frequency at the tune of 7.82, we get the growth rates at the injection as 240/sec. and 125/sec. at the extraction. If the steel wires are used, then the growth rate at the injection will be 1150/sec. at the injection and 625/sec. at the extraction. This is shown in Fig. 2.13.2.

Considering the following factors, the transverse damper is probably not necessary.

- As soon as the ramping started, the tune can be reduced, therefore, only the injection period is of concern.
- According to the AGS experience, the growth rate calculated this way might be overestimated, say a factor of 5.

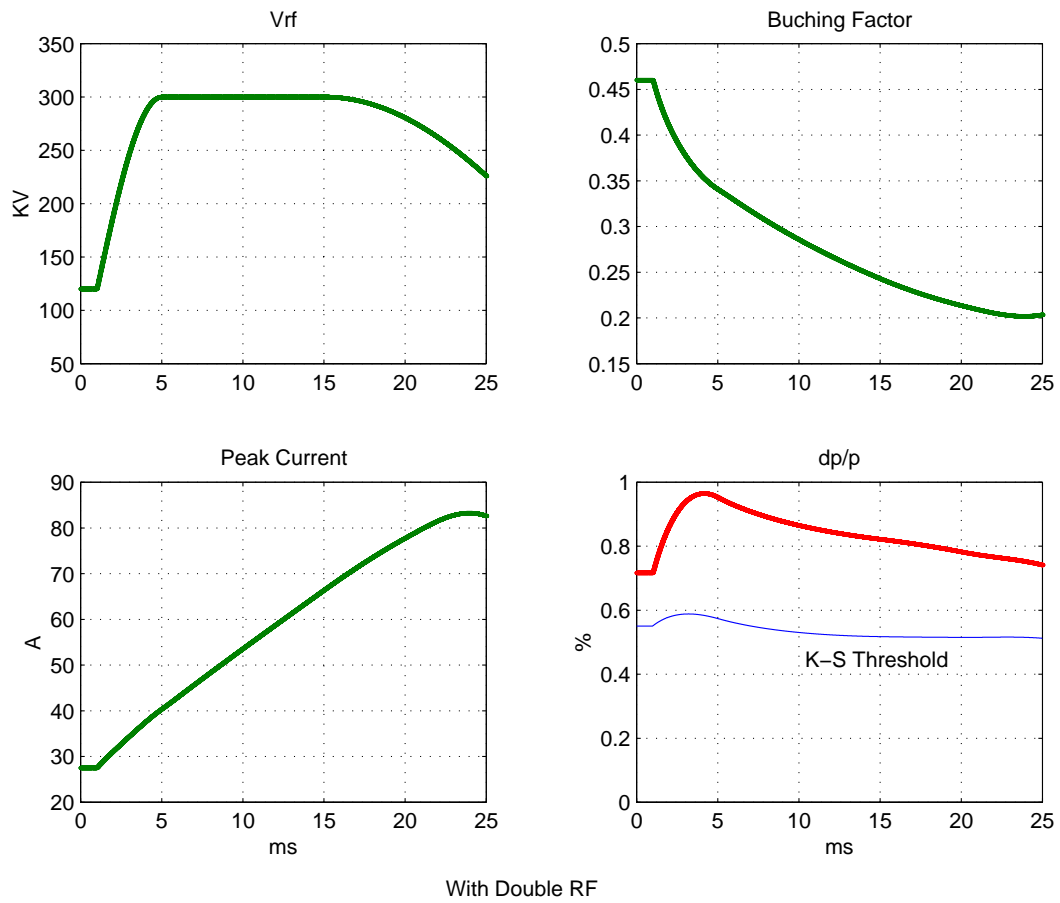


Figure 35: RCS RF voltage program, bunching factor, peak current, beam dp/p , and K-S criterion required dp/p . With double RF.

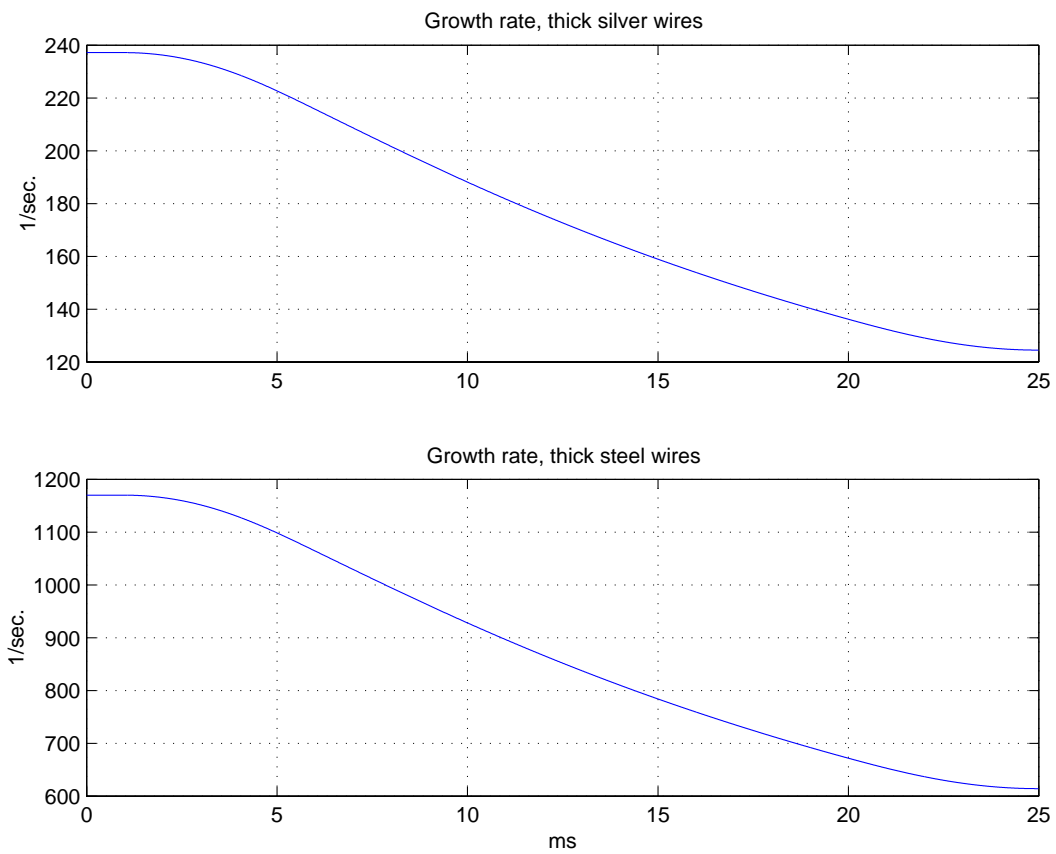


Figure 36: Resistive wall instability, with thick silver and steel walls, from injection to extraction.

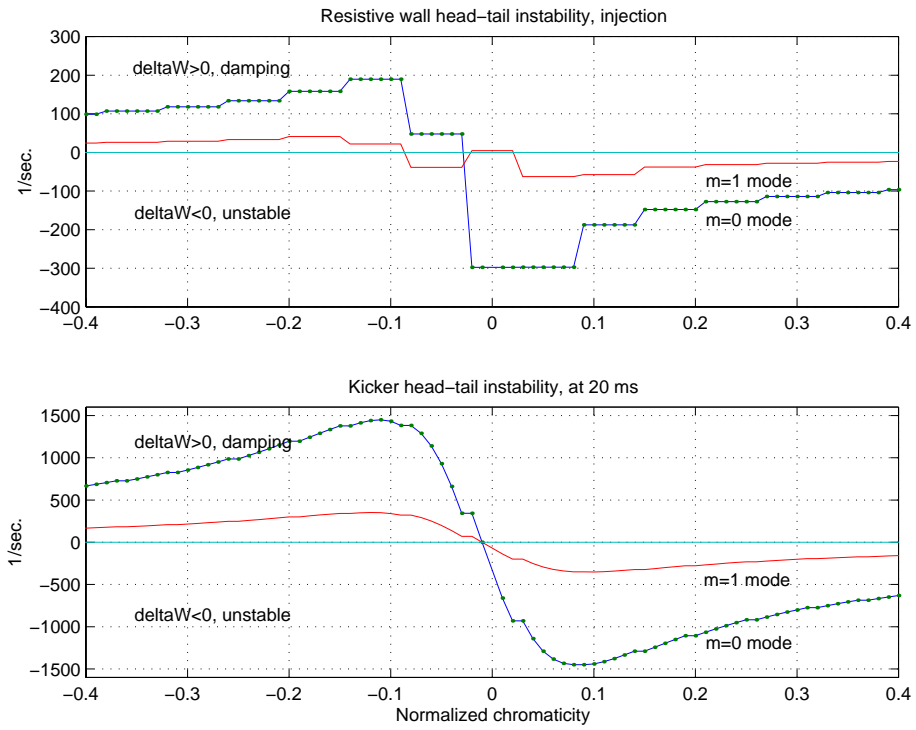


Figure 37: Head tail instability of resistive wall at the injection, and for kicker instability at 20 ms. With both modes of $m=0$ and $m=1$.

- The rapid ramping might contribute to a damping for the resistive wall instability, according to the Booster experience.

Head-tail instability The important factor in the head-tail instability is the chromatic frequency,

$$\omega_\xi = \frac{\xi}{\eta} \nu_0 \omega_0 \quad (53)$$

which is represented by the spectral line n' used in equation (2),

$$n' = n - \frac{\omega_\xi}{\omega_0} = n - \frac{\xi}{\eta} \nu_0 \quad (54)$$

Typical head-tail instability is observed with respect to the wall impedance. At the vicinity of zero frequency, the wall impedance changes rapidly. For a long bunch with narrow bandwidth, chromaticity is sensitive with respect to the head-tail instability. At the injection, $\eta = -0.463$, a change of the normalized chromaticity of 0.2 yield the beam spectrum frequency shift by 2.4 MHz, about half of the full beam bandwidth.

Taking the termination resistance of 50 Ω , the real part of the extraction kicker impedance is peaked at 7 MHz, about 20 K Ω/m . If we take, say, at 20 ms in the acceleration, the slippage becomes $\eta = -0.095$, then a change of the normalized chromaticity of 0.2 causes a beam spectrum frequency shift by 15.4 MHz. This shifted the beam power spectrum over the peak of the real impedance of the kickers.

In Fig. 3, these two situations are shown, for both modes $m = 0$ and $m = 1$. Since the bunch is long, the natural normalized chromaticity of around -1 should prevent this type of instability to happen. On the other hand, the chromatic tune spread requires the machine to work close to zero chromaticity, which makes it worthwhile to understand better for this instability.

In Table 2.13.2, the maximum possible head-tail growth rates are given for steel wire wall, silver wire wall, and kicker impedances, at the injection and extraction.

Table 26: Largest head-tail growth rates for steel and silver walls, and for extraction kickers terminated by 50 Ohm resistor. At injection and at 20 ms.

$\xi = 0$	Injection	at 20 ms
Steel wire wall	1467	935
Silver wire wall	297	189
Kicker	1426	1449
	1/sec.	1/sec.

Transverse Robinson instability Comparing with the longitudinal Robinson instability, we note the following differences in the transverse case,

- The mode $m = 0$ is dominant, rather than the mode $m = 1$ in the longitudinal case.

- The relevant impedance includes all the narrow band type, for instance, the one generated from the large steps.
- In the transverse case, the Robinson type instability is determined by the betatron tune, which is not a free parameter to adjust.

In the longitudinal case, the Robinson instability with respect to the fundamental mode is cured by the cavity detuning, and that caused by HOM's by de-Q ing. In the transverse case, to eliminate the possible Robinson type instability, the transverse narrow band impedance needs to be reduced. For instance, tapering the large steps, and shielding the chamber cavities, are all favorable in terms of this concern.

Transverse microwave instability Up to now, only the real part of the transverse impedance have been discussed. In general, the positive effective real impedance implies the stability. If the effective impedance is negative, then the frequency spread must be larger than the growth rate to suppress the instability.

On the other hand, the imaginary part of impedance causes the coherent frequency shift. The frequency spread must be larger than the coherent frequency shift. Otherwise, an infinitesimal perturbation may cause instability.

The frequency spread needed to stabilize the beam is represented in the microwave instability criterion,

$$\Delta\nu > \frac{\beta e I_p}{4\pi R m_0 \gamma \omega_\beta \omega_0} |Z_T(n_1)| \quad (55)$$

where $Z_T(n_1)$ is the transverse impedance at the sampling frequency n_1 , consisted by contributions of both real and imaginary parts of the impedance. For the worst case, the peak current is considered all the time.

The total tune spread for the effective frequency $(n + \nu_0)\omega_0$ is,

$$\Delta\nu = ((n + \nu_0)\eta - \xi\nu_0) \frac{\Delta p}{p} + \Delta\nu_{inc} + \Delta\nu_{oct} + \Delta\nu_S \quad (56)$$

where the chromatic and slippage tune spreads depend on the beam momentum spread, the octupolar tune spread is betatron oscillation amplitude dependent, and $\Delta\nu_S$ is the synchrotron oscillation tune spread.

For most low energy proton synchrotrons, without the damping effect of the space charge incoherent tune spread $\Delta\nu_{inc}$, the transverse microwave stability condition cannot be satisfied. The experience at the AGS and the Booster shows that this type of machines, below the transition, are in general stable in transverse. No special care needs to be taken.

2.13.3 e-p like (PSR) instability

For the e-p instability relevant to the similar synchrotrons, one of the most important factor is the potential at the beam center. A large potential helps electrons to stay, and also it is a possible source of the secondary electron production and acceleration at the bunch passage.

The potential for the radial position r within the beam, i.e., $r \leq a$, a is the beam size, is,

$$V = \frac{e\lambda}{2\pi\epsilon_o} \left(0.5 + \ln \left(\frac{b}{a} \right) - \frac{r^2}{2a^2} \right) \quad (57)$$

where λ is the beam line density, b is the chamber radius. Given the similar chamber size, the most important factors are the beam line density and the beam transverse size.

A comparison of the beam potential is shown in the Table 2.13.3. The potential of the SNS RCS at the injection is lower than that of PSR. At the extraction, the RCS potential is the highest. This needs some studies.

Table 27: Comparison of potentials at the bunch center for the AGS Booster, ISIS, PSR, and SNS RCS at injection/extraction. Average beam transverse size is used.

	N	B_f	R	λ	a	b	V
AGS B	40/23	0.4/0.15	32.1	0.5/0.57	2.0/1.1	4.5	1.9/4.2
ISIS	25/25	0.4/0.15	26.0	0.4/0.77	5.0/2.9	6	0.8/3.6
PSR	40	0.4	14.3	1.1	2.0	5	4.6
SNSRCS	104/104	0.46/0.22	47.6	0.76/1.58	4.3/2.5	10	3.4/8.6
	10^{12}		m	$10^{12}/m$	cm	cm	KV

Table 28: Comparison of machine parameters relevant to e-p like instability. The beam intensity corresponds to instability threshold for PSR, AGS Booster, KEK PS Booster and CERN PS, to the maximum value attempted for ISIS, and to the nominal value for SNS (2MW) and ESS.

Quantity	PSR	AGS Booster	KEK PS Booster	CERN PS	ISIS (inj.)	ISIS (ext.)	ESS (RCS)	ESS (RCS)	SNS (RCS)	SNS (RCS)
Circumference (C [m])	90.2	202	37.7	628	163	163	248	288	220	299
Energy (E_k [GeV])	0.799	0.2	0.04	1.0	0.07	0.8	1.334	3.0	1.0	2.0
Acceptance [$\pi\mu\text{m}$]	140	100	241/49	60/20	500	500	480	560	360	600
Emittance [$\pi\mu\text{m}$] (H/V , $\epsilon_{UN,rms}$)	7/13	8	3~8	7/3	50	17	30	14	36	27
UNBUNCHED:										
N_0 [10^{13}]	0.8	2~4	0.35		4	2.5				
1D density [m^{-1}]	0.9	1~2	0.93		2.5	1.6				
2D density [m^{-2}]	0.13	0.1~0.2	0.12~0.33		0.05	0.09				
3D density [m^{-3}]	0.017	0.02~0.04	0.05~0.13		0.009	0.016				
Unstable?	yes	yes	yes	yes	no	no				
BUNCHED:										
N_0 [10^{13}]	3.8			0.3			20	23.4	20.8	10
Bunching factor	0.37			0.048			0.5	0.5	0.35	0.21
1D density [m^{-1}]	11.4			1.0			18.2	18.9	20.6	15.9
2D density [m^{-2}]	1.63			0.34			0.56	0.63	1.5	0.59
3D density [m^{-3}]	0.21			0.02			0.09	0.085	0.16	0.09
Unstable?	yes	no	no	yes	no	no				
Growth time [μs]	25~80	~20	>210	500	—	—	—	—	—	—
Frequency [MHz] (unbunch/bunch)	~70/ ~175	80~100	10~200	20~40	—	—	—	—	—	—
Unstable direction	V	V	H/V	H						
Dependent factors	V_{rf} , ϕ_s $\Delta p/p$, ϵ_{rms} sextupole tunes impedance rf centering	σ_s tunes ...	σ_s vacuum ...	σ_s loss ...						

1D density (N_0/BC) in [$10^{11}/\text{m}$]; 2D density ($N_0/BC\epsilon_{rms}$) in [$10^{17}/\text{m}^2$]; 3D density ($N_0/BC\bar{\beta}\epsilon_{rms}$) in [$10^{17}/\text{m}^3$], with B the bunching factor, and N_0 the number of protons

PSR: R. Macek, private communications

AGS Booster (injection): M. Blaskiewicz, private communications

KEK Booster: Y. Irie, et al, KEK Proc. 97-17, (1997) pp. 247 – 255

CERN PS: R. Cappi, G. Metral, <http://www.cern.ch/PSdoc/ppc/md/md980716/epinstab.html>

ISIS, ESS, ESS (RCS, extraction): G. Rees, private communications

2.14 Beam Diagnostic Instrumentation

The beam diagnostics instrumentation for the RCS Ring is summarized in the table below.

Table 29: RCS RING Beam Instrumentation.

Measurement	Device	Quantity (per Ring)
Beam Loss	Ion chambers and Photo-multipliers	80 (IC) + 8 (PM)
Beam Current	Current transformers	1 (Fast) + 1 (slow)
Beam Position	Striplines	48 dual plane
Profile	Ionization Profile Monitor	2 planes
Tune/Damper	Stripline Kicker	2 planes
Bunch Acquisition System	Multichannel 1 GSa/s digitizer	16 channels
Beam in Gap Cleaner	Stripline kicker/fast switch	1

2.14.1 Beam Loss Monitors

The primary functions of the Beam Loss Monitor (BLM) system are to minimize losses by allowing tuning of the beam, and to prevent injection of subsequent beam following a high loss. Programmable threshold detection circuitry will provide an interlock signal tied to the Fast Protect System to prevent beam injection following high loss pulses. Ion chambers will be located regularly around the Ring at the quadrupoles and other points of expected transverse losses. Each BLM will be capable of inhibiting further injection if the losses exceed 1 W/m. Time resolution of the main system will be several microseconds. A limited number of Fast Beam Loss Monitors (FBLMs) capable of observing losses within a single turn will be located at the downstream end of each straight leg, and at injection and extraction areas where losses from longitudinal effects might be observed. Data from the FBLMs will be acquired through a separate Bunch Acquisition System, which will take data at a 100-1000 MSa/s rate.

Ion chambers will be used for the BLM system and scintillator-photo-multipliers will be used to as the FBLMs. The ion chamber detectors are sealed argon-filled glass units, which were developed for the Tevatron at FNAL [23], and are being used in modified form in RHIC. The sensitivity of these units is 70 nC/Rad. The modifications include non-PTFE connectors and isolated BNCs to break signal ground loops. Measurements made during the RHIC first sextant beam test showed a clean 4-decade range [24]. This was later extended another 2 decades upward by desensitizing the electronics. Response times are 1 – 2 μ s for electrons and about 1 msec for ions.

Since the 1 W/m figure represents the losses over 1 second, the processing electronics must provide the integral of the losses over each accelerator cycle. These will then be summed as a running total over 30 pulses. For tuning, however, it is often more desirable to see the losses during a pulse directly rather than their integral. For this reason the processing electronics will be designed to provide both outputs.

The FBLM detectors are “Paint Cans” containing liquid scintillator. They were used as the radiation monitors at FNAL for some years. The PSR also uses this type detector to track fast losses. Scintillator-Photo-multipliers offer a wide dynamic range of operation and

fast (nano-second) response, but show significant unit-to-unit variation and must be calibrated regularly. Radiation darkening of the scintillator and the glass of the photo-multiplier tube affect the calibration.

2.14.2 Beam Current Monitors

Beam Current Monitors (BCM) will provide information of the average current circulating in the ring and the charge density distribution within the bunch.

For the average intensity measurement in the RCS Ring the BCM resolution must be better than 0.1% of full intensity. This will require the use of different gain ranges for the early turns and for the remainder of the cycle. Compensation for the change in revolution time during the cycle will be provided so that the output will represent intensity rather than current. The rise time must be 100 nsec or less with a droop of less than 0.1% over the full cycle. While the HEBT transformer sees beam for only 600 μ sec, the Ring beam lasts for the injection period plus the acceleration duration, a total of 25 msec. This will require a magnetic feedback beam current transformer to achieve this low droop over such a long duration. With this design the signal observed on the secondary winding is amplified and applied to a tertiary winding which opposes the flux decay in the core. The increase in the droop time constant comes at the expense of output signal level, but this should not be a problem for the high intensity RCS ring.

The charge density distribution within the bunch will be measured with the fast current transformer (FBCM). The FBCM must have a risetime of 1 nsec or better to observe the 420 nsec bunch length, and a droop of at least 100 msec. Compensation for this droop will be provided. Acquisition will be through the 100 – 1000 MSa/s of the Bunch Data Acquisition System. While a Wall Current Monitor (WCM) could provide the same information, the bandwidth requirements for the RCS do not require the design complexity of a WCM, especially since a commercial current transformer is available which will meet the specifications.

2.14.3 Beam Profile Monitor

The profile must be measured non-destructively to prevent beam loss and activation of the ring. The measurement should cover a range of 90 mm with a bin size of 1.4 mm. The effect upon the beam, whether due to scattering or orbit distortion, must be minimal. Measurements made during the first 100 μ sec of injection will require integration over multiple turns and injection of gas. During acceleration profile data will be available throughout the cycle on each turn.

Interceptive profile measurement techniques using scrapers or thin carbon wires rapidly moved across the beam pipe (Flying Wires) will cause too much loss and soon be destroyed by the beam. An ionization profile monitor (IPM) makes use of the interaction of the beam with residual gas molecules in the vacuum chamber. [25] An IPM measures the spatial distribution of electrons freed by ionizing collisions of the beam with residual gas in the vacuum chamber. The electrons will be swept from the beam pipe by a transverse electric field, amplified by a microchannel plate (MCP), and collected by a circuit board with strip anodes oriented parallel to the beam axis. A magnetic field, parallel to the sweep electric field, counters the defocusing

effects of space charge and recoil momentum. For the 1 MW beam the maximum space-charge field will be about 5×10^4 V/m. In a magnetic field of 0.1 T, an electron subject to this field will travel parallel to the collector channels at 3×10^5 m/s with a gyration radius of 35 mm. Profile broadening by the space-charge field will be insignificant. An electric field of 150kV/m will remove electrons in under 10ns producing a maximum longitudinal drift of less than 4mm. The energy spectrum of recoil electrons extends to 3.0 MeV but over 95% will have energies < 500 eV. The 0.1 T field will confine a 500 eV electron to a Larmor radius of < 0.8 mm which is 2% of the beam radius. For a field of 0.1 T most of the electrons will be collected on the anodes over which they are formed. Three permanent magnet dipoles will be used to provide electron confinement without perturbing the beam orbit.

The MCP has a limited lifetime so both administrative constraints (don't run the IPM continuously) and provisions to gate the MCP bias voltage will be required to prevent plate depletion.

2.14.4 Beam Position Monitors

The Beam Position Monitor System will provide closed orbit measurements for the Ring. Stripline detectors will be located in each of the 48 quadrupoles. Because of the large number of detectors the beam position monitors (BPMs) must present low impedance to the beam to prevent instabilities. Detector length and transitions will be selected to give the lowest impedance consistent with required signal levels.

The dual plane stripline BPMs will be located adjacent to the quadrupole, but because they will be of stainless steel construction, cannot be in high field regions. The design will make use of techniques developed for the RHIC BPMs. The electrodes will be about 12 cm long and subtend an arc of 70 degrees, with the possibility reserved of longer lengths by extending the electrodes into the shielded pumping tee.

Calculations indicate that at 1×10^{10} circulating beam, circuit noise will provide a resolution of 1 mm RMS, improving to 50 :m at 2×10^{14} . Position measurements will be made on a turn-by-turn basis with data from multiple cycles stored locally for recall if a beam fault should occur. Data for computation of the closed orbits will be available from the front end processor on each cycle if desired. The analog electronics will consist of an impedance matching front end 0.1 - 5 MHz duplexing filter, followed an amplification stage. A low pass anti-aliasing filter precedes the 12-bit ADCs which sample the signal at 41 MSa/s. The over-sampled data is then stored in on-board shared VME memory. The data will be digitally processed at the front end to provide the position information. The local memory will be of sufficient size to store several cycles of position history data (useful following a beam inhibit/dump). Upon request averaged data, single revolution data, or the full memory may be obtained.

The wide dynamic range in signal will be covered with 2 gain states. An analog DPDT switch will direct the signal through the 0 dB or -40 dB paths, then into a 256 state programmable gain (40 dB) amplifier. Switching will require 1-2 turns so only a few gain changes per cycle will be used.

Triggering must be adjusted during the acceleration portion of the cycle since the fixed delays become phase shifts as the RF frequency changes. The same situation existed in the AGS booster in which the frequency swing was far more dramatic. It was easily handled with

modern digital techniques.

2.14.5 Damper/tune measurement

Transverse beam instabilities may develop which will lead to beam loss. While the need for a Damper was not clearly demonstrated for the LAR design, since the cycle time was so short, the 24 msec acceleration duration makes the need for a Damper likely for the RCS. The actual Damper parameters will require more detailed study of the instability growth rates expected. Measurement of the tune of the ring will be provided by using the Damper kicker to excite the beam oscillations.

A system similar to that in the AGS [26] will be installed to damp both horizontal and vertical transverse oscillations in the beam orbit. The AGS system takes signals from the beam position pickups and digitally processes them to obtain orbit data. The average orbit is subtracted to determine the excursion of the bunch and a correcting kick amplitude is obtained from a look-up-table (LUT). The kick is delayed using a FIFO and applied to the bunch on a later turn using a wideband 500 Watt RF amplifier to drive a stripline. The tune measurement will be made using the Damper to kick the beam. The digital acquisition and processing electronics for each beam position monitor has sufficient memory to store the position for the entire cycle. An FFT analysis of this data is normally used to find the fractional tune.

2.14.6 Beam-in-gap cleaner

Beam between the bunches will be lost during the acceleration phase or at extraction and contribute to the uncontrolled loss. This may come during the injection phase due to chopping residuals or foil scattering, or at any time due to beam instabilities. A 5-meter long gap cleaning stripline kicker will be installed in a straight section with a vertical betatron phase 90° from a collimator. MOSFET switch banks will provide 5 kV, 120 A pulses with 10 nsec rise and fall times during the gap which will build up the displacement over 20-25 turns. Dissipation in the switch banks may limit the number of times within the cycle that they can be fired but these bursts can be timed to occur at the end of injection and during high loss periods. A fast gated loss monitor viewing the collimator will provide a measure of the beam in the gap.

3 High Energy Beam Transfer Line

3.1 Introduction

The SNS RCS High Energy Beam Transport line (HEBT) connects the 400 MeV LINAC to two RCS rings. The HEBT not only matches the beam into the synchrotrons, but also defines the beam quality at injection. Table 3.1 gives the required Twiss parameters at the entrance (before the last LINAC quadrupole) and exit (injection stripping foil) of the HEBT. In addition, a major requirement of all parts of this accelerator is minimization of uncontrolled beam losses to allow hands-on maintenance. This is achieved by maintaining adequate tolerances on elements, appropriately located collimators, and sufficient beam diagnostics.

Table 30: Twiss parameters at the entrance and exit of the HEBT.

Twiss parameters	Entrance (end of LINAC)	Exit (stripping foil)	Units
α_x	-2.5255	0.00	
β_x	7.4897	5.00	mm/mr
ϵ_x	2.5	2.5	π mm·mr (5 RMS, unnorm.)
α_y	0.86898	0.00	
β_y	2.6233	6.000	mm/mr
ϵ_y	2.5	2.5	π mm·mr (5 RMS, unnorm.)
α_z	0.0005	0.14	
β_z	0.005	0.05	deg/keV
ϵ_z	1500	1500	π keV deg (5 RMS.)

The HEBT has following functions: (a) matching of the beam from the LINAC into the transport line, (b) momentum selection, (c) momentum compaction, (d) preparation of the beam for injection, (e) characterization of the beam out of the LINAC and before injection, and (f) halo cleanup. We have managed to decouple the first four of these functions, and can consider the HEBT as having three sections: LINAC-Achromat Matching Section (LAMS), Achromat, and Achromat-Ring Matching Section (ARMS). In addition to the 45° bend to the ring, there is a 0° beam line used for LINAC beam characterization, as shown in Fig 3.1.

The first two cells (8 m/cell) after the LINAC (LAMS) are used to characterize the LINAC beam, match beam into the Achromat, collimate beam halo. Following this section, the four cell long Achromat (8.5/cell) bends the beam 45° and provides momentum selection by cleaning up the beam energy halo at the point of maximum dispersion ($\eta_x=2.4$ m). The energy stabilizer and energy wobbler cavities are located in the first cell following the Achromat (in the ARMS), where the dispersion and its derivative are zero. The remaining four cells (9.35 m/cell) are used for matching the beam into the RCS ring, diagnostics. In ARMS, just after the 15 degrees horizontal bending magnet there is 30 Hz switching magnet which divert the beam vertically in two RCS rings. About 25 meters down the switching magnet there is small vertical dipole corrector.

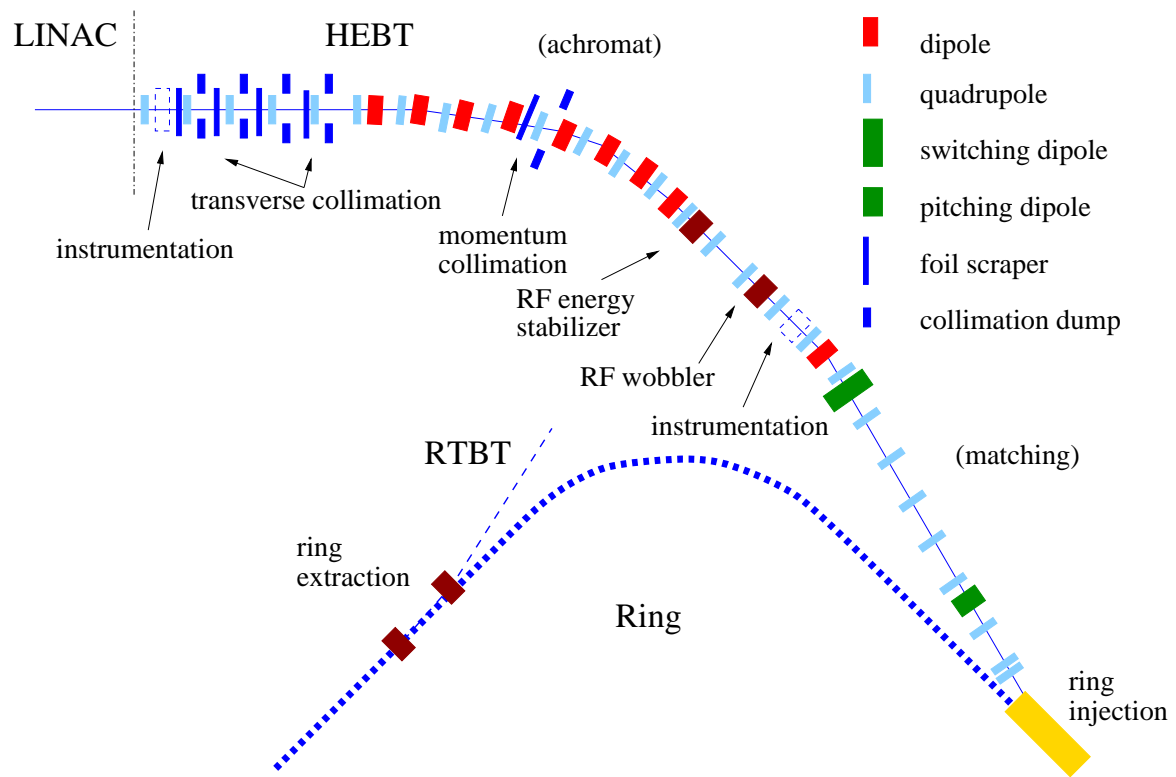


Figure 38: Schematic layout of the rapid-cycling synchrotron HEBT transfer line.

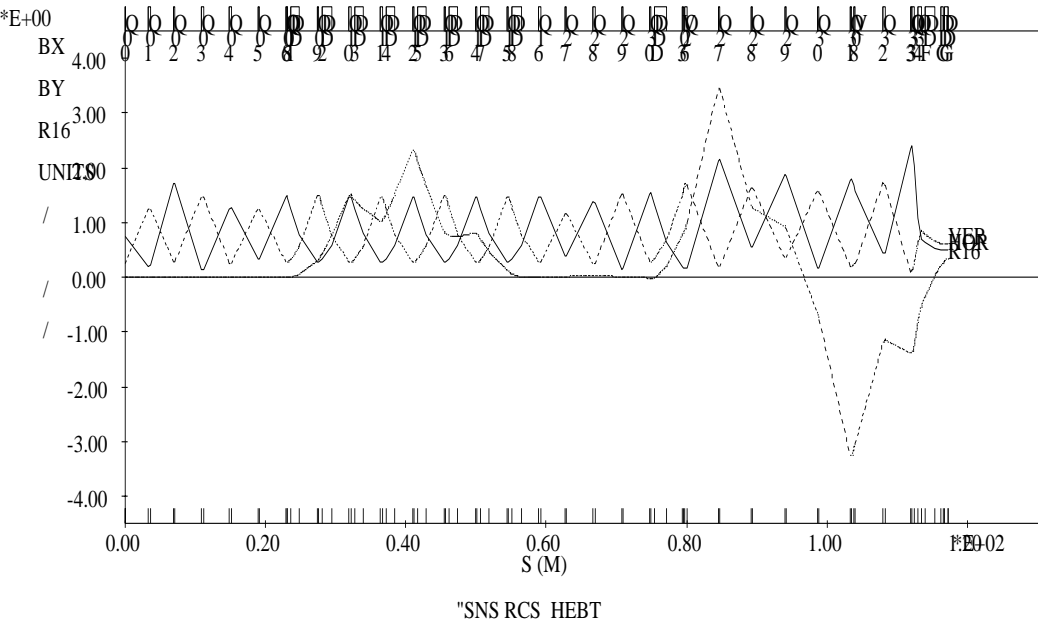


Figure 39: HEBT optics.

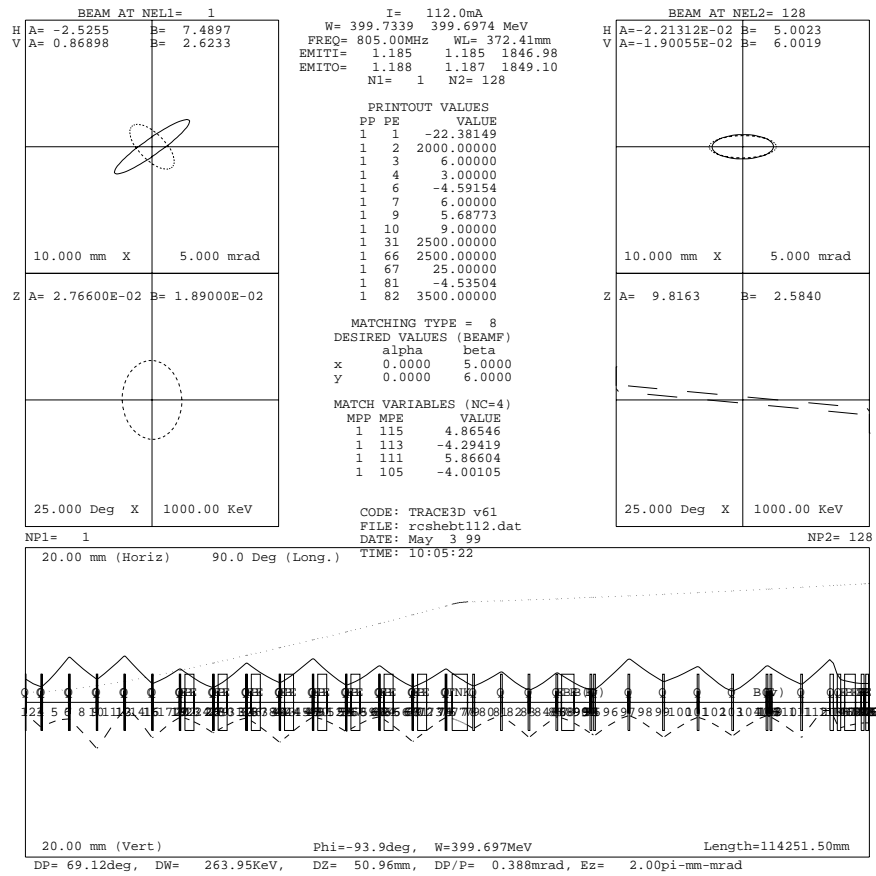


Figure 40: HEBT optics.

3.1.1 LINAC to Achromat matching section

The LINAC has a FODO lattice with a phase advance of about $60^\circ/\text{cell}$, and the Achromat has a FODO lattice with $90^\circ/\text{cell}$ phase advance. The first two cells (four quadrupoles) of the HEBT provide a smooth transition between the two. To remove any LINAC beam halo, there are four movable and four fixed collimators located in the 2nd to 5th half-cells in this section (details of the configuration are discussed in the section on halo scraping). The space between quadrupoles in the first cell of the HEBT is occupied by beam diagnostics, as discussed in a later section.

3.1.2 LINAC beam dump

In addition to the 450 bend to the synchrotrons, there is a 35 m long beam line straight out of the LINAC for LINAC beam characterization and beam dumping.

3.1.3 Momentum selection (Achromat)

A 45° achromatic bend starts at the 3th cell of the HEBT line, and finishes in four cells, containing eight 5.625° dipoles. The total phase advance in the Achromat is 360° . A beam energy-halo scraper is located at the middle cell of the Achromat, where the dispersion is maximum (2.4 meter). Figure 3.1.4 shows amplitude functions (β_x, β_y) and dispersion function (η) along the HEBT. The first dipole of the Achromat is a switching magnet to provide beam to the 0° LINAC dump.

3.1.4 Energy stabilizer & energy wobbler

Due to phase and amplitude errors in the LINAC RF system, expected random energy error is about ± 1.3 MeV. To correct this error there is about 1 meter long, 8 cell, 805 MHz RF cavity operating at gradient of 1.3 MV/m, about 50 meter from the LINAC in the first half cell after the LINAC. The difference in phase between on energy and off energy at the cavity is about 48 degrees/MeV. The momentum spread requirement for the RCS ring is $\Delta p/p = \pm 0.4\%$. This is accomplished with a 1 meter long, 8 cell, 805.1 MHz (about 100 kHz different from the Linac frequency) RF cavity, operating at a gradient 2 MV/m. These cavity are similar to the last cavity of linac. Both cavities is located in the first half-cell after the achromat (50 m from the linac), where the dispersion and its derivative both have zero values.

Table 31: Energy compressor specifications.

Type	Location	Freq	Field	Aperture	Length
8 cell	ARMS	805 MHz	1.3 MV/m	4.8 cm ϕ	1 m
8 cell	ARMS	805.1 MHz	2.0 MV/m	4.8 cm ϕ	2.6 m

3.1.5 Ring matching section

After the achromat, two cells are provided for the diagnostics. At the end of the achromat this line is horizontally parallel to the ring straight section, allowing one to have the required “dog leg” for injection into the ring. After the 15 degrees horizontal band magnet, a 30 Hz, 2.5 degrees switching magnet separate the beam vertically for two RCS rings. A 2.5 degrees vertical corrector magnet is located about 25 meter down stream to switching magnet. This provide ± 1 meter separation between two RCS rings. This section has enough “knobs” (quadrupoles) to match six variables (four amplitude functions and two dispersion functions). There is about 20 cm of vertical dispersion at the foil. The locations of the dipoles are determined by the injection scheme.

3.2 Magnets and Support

Table 3.2 shows the magnet requirements for the HEBT.

Table 32: Magnet requirements for the HEBT.

	Type	Location	No.	Field	Aperture	Length
Dipoles	5.625°	Achromat	8	0.3 T	8 cm gap	1.25 m
	(V) 2.5°	ARMS	2	0.33	8 cm gap	0.25 m
	Switching 2.5°	ARMS	1	0.33	8 cm gap	0.25 m
	15°	ARMS	1	0.55 T	8 cm gap	1.75 m
Quadrupoles	QH/QV	LAMS	6	6.5 T/m	8cm ϕ	0.25 m
	QH/QV	Achromat ARMS	25	5.0 T/m	15 cm ϕ	0.25m
	QH/QV	ARMS	4	4 T/m	25.6 cm ϕ	1.15 m

3.4 Instrumentation and Diagnostics

The instrumentation was selected to allow characterization of the beam coming from the linac, provide tools for tuning and loss protection of the transport line, and allow setup of the beam for injection into the RCS ring. The beam diagnostics instrumentation which will be required for the HEBT line is shown in the table below.

Table 33: HEBT instrumentation.

Measurement	Device	Quantity
Beam Loss	Ion chambers and Photo-multipliers	34 (IC) + 3 (PM)
Beam Current	Current transformers	2 (Fast) + 2 (slow)
Beam Position	Striplines	26 dual plane
Bunch Length	Witkover/Forschenko probe	1
Time of Flight	Capacitive Pick-up	1
Profile	Wire scanners	9
Profile (HARP)	HARP (at Dump)	2
Beam in Gap	Laser	1

Linac emittance will be measured using 4 profile monitors located close to the entrance to the line. These will be spaced at approximately 60° phase advance to reasonably cover the emittance. Stepping wires will be used to make the measurement. Simulations indicate that 8-micron diameter carbon filaments will withstand the beam even if maintained continually in the beam. The signal levels in the region beyond 2 sigma may be enhanced by leaving the wires stationary over a number of beam pulses, extending the dynamic range to allow halo measurements. A similar set of 4 scanners will be used to measure the emittance at the downstream end of the HEBT line. An additional wire scanner will be located at a point of maximum dispersion in the bend to allow on-line momentum spread monitoring. A multi-wire profile monitor (HARP) could not be used at this location because the beam losses would be intolerable.

Beam position will be measured using stripline detectors located at each quadrupole. A simple design with one end shorted (brazed) to the chamber will be used for stability and ease of construction. Since the detectors will be dual plane, test signals injected on the orthogonal plane strips will be used for calibration and testing.

A Witkover/Forschenko bunch density distribution monitor will be installed downstream of the energy stabilizer and RF wiggler to allow longitudinal tuning. A resolution of 1 – 2 degrees at 800 MHz has been achieved with these detectors.

Beam loss monitors will be located at each quadrupole (beta-max). These will be sealed ion chambers of the type used in the RCS ring, located close to the beam pipe to provide the sensitivity needed to monitor losses below 1 W/m. Several additional units will be located at critical components, or may be moved to local trouble spots. The ion chambers will be connected to the Beam Permit Link and used to stop the injected beam in the event of excessive loss. Several photomultipliers will be used to monitor fast (within bunch) losses. These will be located at the end of the linac, in the region of maximum dispersion in the arc, and at injection to the ring.

Signals from pairs of annular capacitive pick-ups will be used to measure the passage of the beam and provide an on-line energy monitor using the Time-of-Flight.

Beam current will be monitored at each end of the line by two transformers: One will measure the details of the chopped beam current with 1 nsec response (same as the fast beam current monitor in the RCS ring) while the other will measure the average current within the chopped bunches with 50 – 100 nsec rise time and $< 0.1\%/ms$ droop. This unit will be a passive current transformer since the injected pulse duration is under 1 msec.

Since the losses must be kept to the level of 0.01%, the beam in the gap between ring bunches must be kept to this level. A device to monitor the beam-in-gap coming from the linac will be installed in HEBT. Using a mode-switched laser, it is estimated that sufficient H-minus beam can be stripped to allow a measurement. The laser must be located just upstream of the bend so the resulting neutral beam could be again stripped and detected in the zero-degree line.

3.5 Vacuum System

Vacuum of mid 10^{-8} Torr level is required in HEBT to minimize gas stripping of the transported H⁻ beam and will be achieved by using UHV material, good vacuum practice and sufficient pumping. Vacuum level of 10^{-7} Torr is sufficient for the RTBT line.

4 Ring to Target Beam Transfer Line

4.1 Introduction

The Ring to Target Beam Transport line (RTBT) connects the accumulator ring, at the beginning of the extraction Lamberson magnet, to the target. It is 160 m long. The beam requirements at the target are given in Table 4.1. Table 4.1 gives the Twiss parameters of the beam at the beginning of the extraction Lamberson magnet and at the target.

Table 34: Beam requirements at the target.

Beam width	200 mm
Beam height	70 mm
Time-average beam current density, over beam footprint	≤ 0.091 A/m ²
Beam power within target and outside nominal spot	$< 5\%$
Peak time-average beam current density, over 1 cm ²	≤ 0.182 A/m ²
Peak 1-pulse density, over 1 m ²	1.89×10^{16} protons/m ²

Table 35: Twiss parameters at the ring Lamberson magnet and at the target.

Twiss parameters	Output of Ring	Target	Units
α_x	0.0	0.0	
β_x	4.499	112.4	mm/mrad
ϵ_x	89	89	p mm mrad (5RMS, unnorm.)
α_y	0.0	0.054	
β_y	4.967	13.8	mm/mrad
ϵ_y	89	89	p mm mrad (5 RMS, unnorm.)

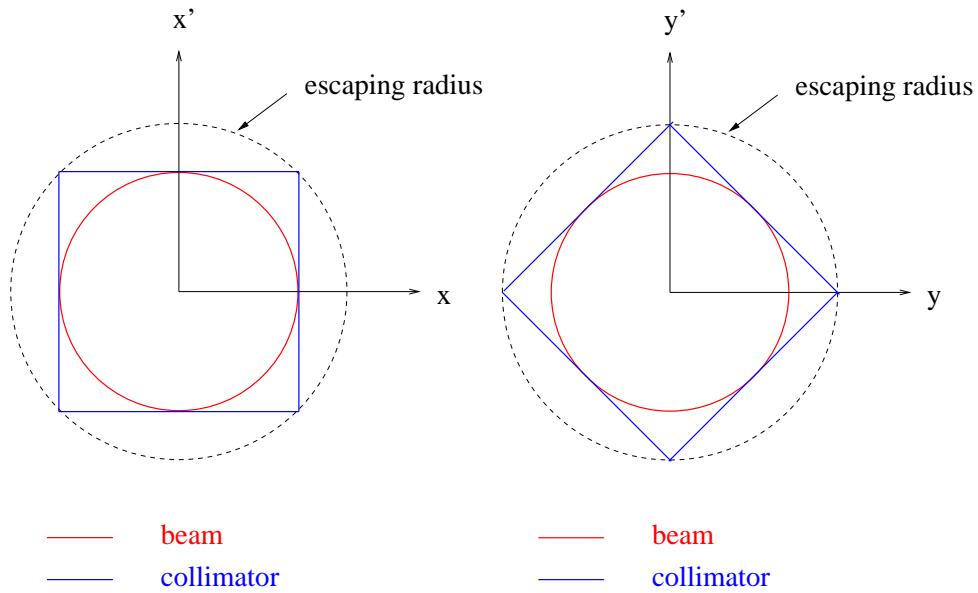


Figure 42: Schematic layout of the HEBT collimation system consisting of movable foil scrapers and dumps.

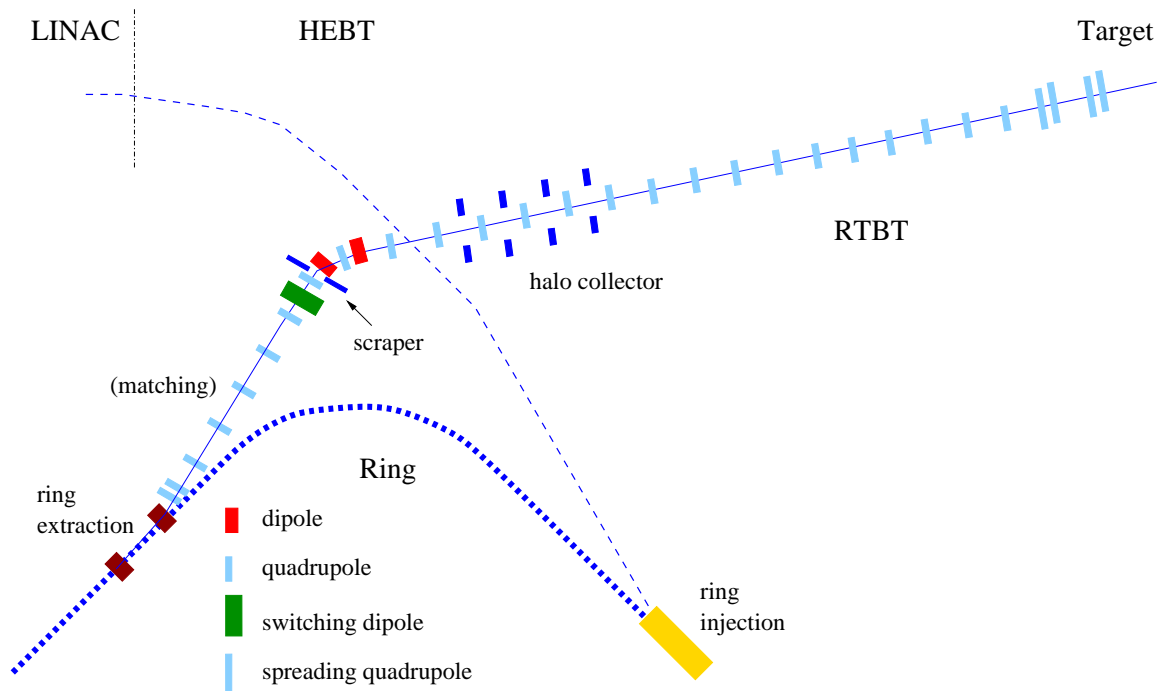


Figure 43: Schematic layout of the RCS RTBT line.

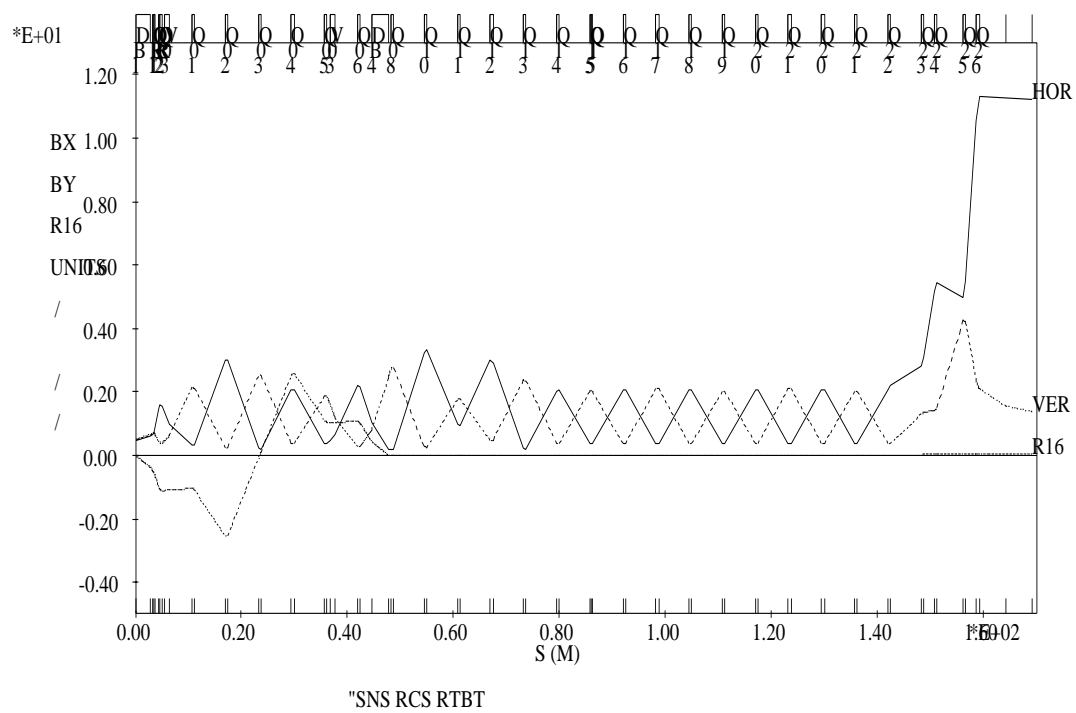


Figure 44: RTBT optics.

4.2 Design Description and Functions of the RTBT Line

The RTBT uses a FODO lattice up to the beam spreading section. The 90° /cell phase advance and length of 12.5 m/cell. The line has following elements: (a) extraction, (b) beam dump, (c) halo collimation, (d) beam spreader, and (e) diagnostics. The first four functions have essentially been decoupled in the RTBT. The extraction system starts in the ring with a Lamberson magnet and continues through four cells in the RTBT. Following the extraction system, the beam can be dumped straight through a 15.5° dipole magnet. After this 15.5° bend, two cells are used for the halo collimation. Following another 6 cells of transport, the last five quadrupoles in the line are used for final beam spreading to produce the beam size required at the target. To reduce the probability of uncontrolled beam losses and define the beam size precisely on the target, RTBT is equipped with four transverse beam halo scrapers and several types of diagnostic devices. Fig. 4.1 shows the layout of the RTBT. Fig. 4.1 shows the amplitude functions (β_x, β_y) and the dispersion function (η) along the RTBT.

4.2.1 Extraction section

The extraction system starts in the ring with a Lamberson magnet and continues through four cells in the RTBT. In this section beam is match from doublet to FODO in four cell with total phase advance of 360 degrees and 15.4° degrees bend which bend in the opposite to the Labmertson magnet. In the second cell there is 2.5° degrees bend magnet and about 20 meter downstream a switching 30 Hz magnet which combine both ring to one transferline to target. This section achromatic in the horizontal direction.

4.2.2 Extraction dump

Following the extraction section, the beam dump is in a line straight through the 15.5° dipole magnet. This dump can handle up to 200 kW beam power and will be used for accumulator tuning purposes. This line is 28 m long. This line has only two quadrupoles.

4.2.3 Beam spreader

The beam spreader consists of two doublets and a singlet near the end of the RTBT. These five 36 cm diameter aperture quadrupoles provide the desired beam size at the target, as given in Table 4.1. Due to thermal considerations of the target, the beam current density on target must remain below the limits shown in the table. There will be one harp located near the ring extraction and a pair of harps ~ 1.5 m in front of the target. Since the harp in front of the target is important for guaranteeing beam flatness, there will be two units, one always in the beam and the second retracted as a spare

4.3 Magnet System

Table 4.3 shows the magnet requirements for the RTBT.

Table 36: Magnet requirements for the RTBT.

	Type	Number	Field	Aperture	Length
Dipoles	15.5 degree	1	0.81 T	19.8 cm \times 45 cm	3.1 m
	Switching (V)	1	0.41 T	45 cm \times 19.8cm	1.0 m
	Corrector(V)	2	0.41 T	45 cm \times 19.8 cm	1.0 m
Quadrupoles	QH/QV*	32	4.6 T/m	25.6 cm ϕ	0.6 m
	Special	5	3 T/m	36 cm ϕ	0.8 m

* Same as the RCS ring quadrupoles.

4.4 Halo scraping (collimation)

To define the beam size at the target, there are four beta collimators in the RTBT line. These collimators are located just after the last 15.5° bend in the line in two cells with 90 degrees/cell phase advance, and each is designed to handle up to 1 kW of beam power. There is a three meters long collimator just before the target window to prevent beam from hitting outside of the target area.

4.5 Beam Diagnostic Instrumentation

The beam diagnostics instrumentation for the RCS Ring-to-Beam-Target (RTBT) line is summarized in the table below.

Table 37: RTBT instrumentation.

Measurement	Device	Quantity
Beam Loss	Ion chambers and Photo-multipliers	34 (IC) + 3 (PM)
Beam Current	Current transformers	2
Beam Position	Striplines	26 dual plane
Profile	Wire scanners	5
Profile (HARP)	HARP (at Dump)	2

The beam in the RTBT line consists of a single turn extraction of the beam in the RCS ring. With the 2nd harmonic RF design, this beam will consist of two bunches, each with a duration of a few hundred nanoseconds. Signals from some detectors, such as the ion chambers, the HARPs and the Wire Scanner profile monitors, will be an integrated over the full beam. The fast signals, such as the photo-multiplier loss monitors and the current transformers, will have information about the bunch structure which would be of interest. These fast detectors will

have their signals available for the 100-1000 MSa/s digitizers. The current transformer will also have an integrated output available for total charge transferred.

The detectors have all been described earlier and are not unique to the RTBT with the exception of the HARPs. The target harp will be specially designed for high radiation since it will be located very close to the neutron conversion target. In addition it must be designed to be easily removable and replaceable using remote handling .

As in the HEBT line, there will be a BPM and a BLM at each quad, and 4 wire scanners to measure the emittance of the extracted beam. The HARPs will be used to assure an acceptable distribution for the target.

4.6 Vacuum System

Vacuum level of 10^{-7} Torr is sufficient for the RTBT line.

5 Challenges

- Cleaning of ramping and RF capture beam loss
- Development of programmable magnet power supply
- Construction of large-bore magnets with laminated coils
- Construction of large-aperture vacuum chambers with RF shielding
- Control of magnetic field errors due to ramping eddy current and saturation
- Need for separate quadrupole magnets for eddy current mismatch compensation
- Instabilities (head-tail, e-p like (PSR), etc.)
- Achievement of desired beam distributio at the target (may require beam manipulation in RTBT using octupoles)

6 Appendix

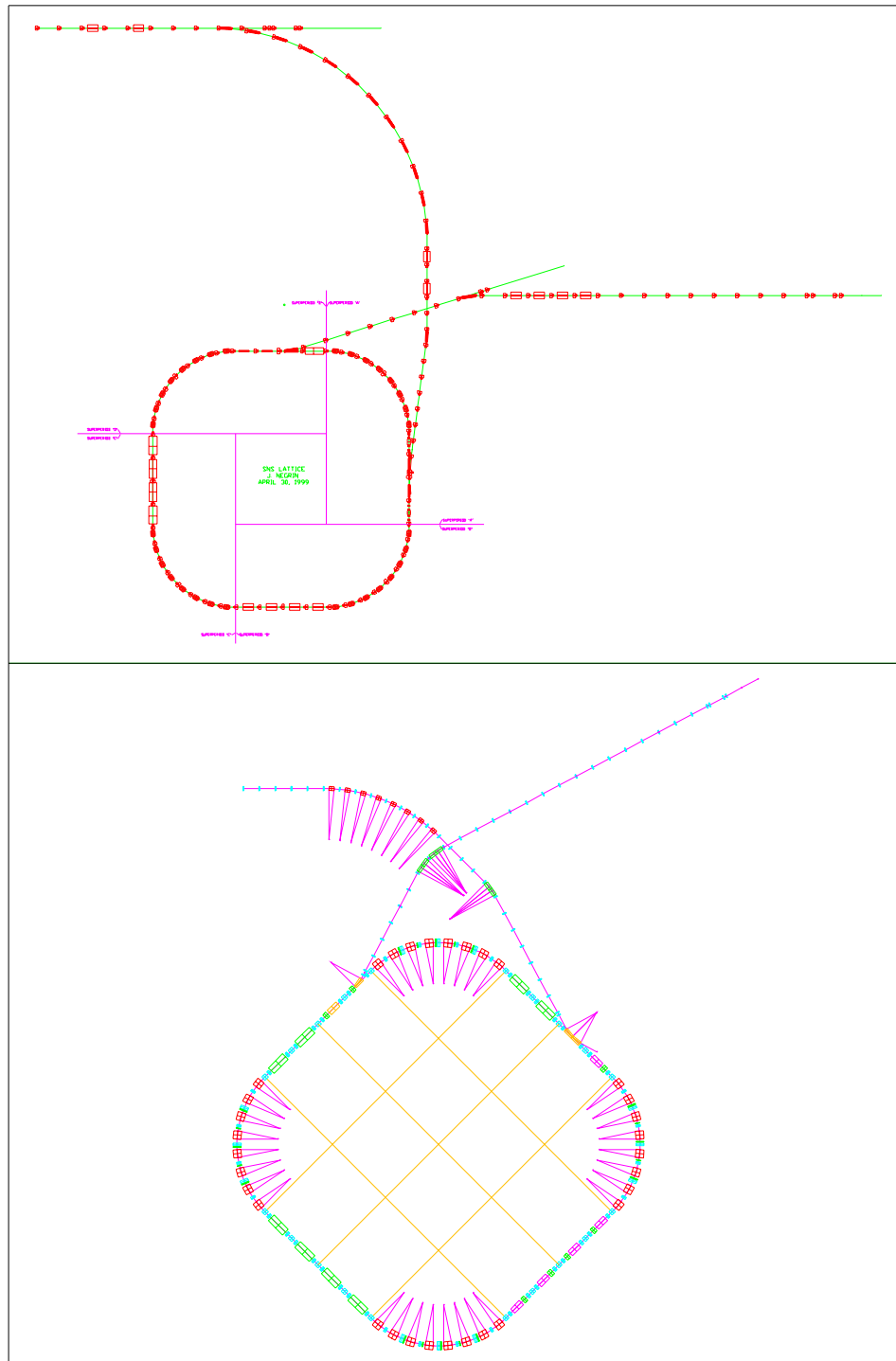


Figure 45: SNS rapid-cycling synchrotron (RCS) layout in comparison with the LINAC-accumulator ring (LAR) layout.

Table 38: Comparison of RCS machine parameters.

Quantity	ESS	JHF	ANL	SNS
Ring	2	1	1	2
Beam power per ring [MW]	2.5	1	1	1
Superperiod	4	3	4	4
Rep. rate [Hz]	25	25	30	30
Injection E_k [GeV]	0.8	0.4	0.4	0.4
Extraction E_k [GeV]	3	3	2	2
Circumference [m]	288.4	320	190.4	299.2
Number of proton [10^{14}]	2.08	0.83	1.04	1.04
RF voltage [kV]	240+120	420	180	300+100
RF freq. [MHz]	1.75/2.02		1.12/1.49	1.43/1.90
RF harmonic h	2		1	2
Lattice	doublet	FODO/doublet	FODO	FODO/doublet

References

- [1] *Spallation Neutron Source Design Manual*, June 1998.
- [2] T. Wangler, *RF Linear Accelerators*, Wiley & Sons, p. 285.
- [3] T. Roser, private communications, 1999.
- [4] *European Spallation Neutron Source Design Manual*, June 1998.
- [5] *JHF Accelerator Design Report*, JHF Project Office, KEK Report 97-16 and JHF-97-10, March 1998.
- [6] *IPNS Upgrade Design Manual*, .
- [7] *5 MW Pulsed Spallation Neutron Source Preconceptual Design Study*, Brookhaven National Laboratory Report No. 60678, June 1994.
- [8] C. Gardner, Y. Y. Lee, N. Tsoupas, J. Wei, “An Alternative Lattice for the Spallation Neutron Source Accumulator Ring”, Proceedings of the 1999 PAC, New York, N. Y., USA, 29 March–2 April, 1999.
- [9] F. Pederson, IEEE, TNS, Vol. NS-22, No. 3, p.1906, (1975).
- [10] A. Gamp, CERN 92-03, p.408.
- [11] R.E. Prael and H. Lichtenstein, *User Guide to LCS: The LAHET Code System*, Los Alamos National Laboratory, Los Alamos, NM, LA-UR-89-3014 (1989).
- [12] MCNP-A General Monte Carlo N-Particle Transport Code Version 4A, J.F. Breisemeister, ed., Los Alamos National Laboratory, Los Alamos, NM, LA-12625-M (1993).
- [13] A.G. Croff, *ORIGEN2 - A Revised and Updated Version of the Oak Ridge Isotope Generation and Depletion Code*, Oak Ridge National Laboratory, Oak Ridge, TN, ORNL-5621 (1980).
- [14] E.J. Sternglass, Phys. Rev. 108, 1,1 (1957)
- [15] M. Plum, PSR-95-001, LANL, (1995)
- [16] S.Y. Zhang, *Secondary Electron Emission at the SNS Storage Ring Collimator*, SNS Tech Note 50 (1998) References
- [17] In Reference [7], pp4.3-69
- [18] J.R.J. Bennett and R.J. Elsey, IEEE NS-28, Vol. 3, 3336(1981).
- [19] T. Hodges et.al., IEEE 91CH3038-7, 2272(1991).
- [20] S.Y. Zhang and J.G. Wang, SNS RCS Ring Impedances, in preparation.

- [21] S.Y. Zhang, SNS Storage Ring Impedances, SNS Tech. Note, No.61, March, 1999.
- [22] M. Blaskiewicz, private communication.
- [23] Shafer, R. E. et al, 1983, *The Tevatron Beam Position and Beam Loss Monitoring Systems*, Twelfth Intl. Conf. on H. E. Accel., p 609.
- [24] Witkover, R., et al, *RHIC Beam Loss Monitor System Design*, Proc. 1997 Part. Accel. Conf, 97CH36167, p.2218.
- [25] Connolly, R., et al, *An Ionization Profile Monitor for SNS*, 3/1/99.
- [26] Smith, G. A., Castillo, V., Roser, T., Van Asselt, W., Witkover, R., Wong, V., *Digital Transverse Damper for the Brookhaven AGS*, Proc. 1995 PAC p.2678.